INFORMATION TO USERS

This manuscript has been reproduced from the microfilm master. UMI films the text directly from the original or copy submitted. Thus, some thesis and dissertation copies are in typewriter face, while others may be from any type of computer printer.

The quality of this reproduction is dependent upon the quality of the copy submitted. Broken or indistinct print, colored or poor quality illustrations and photographs, print bleedthrough, substandard margins, and improper alignment can adversely affect reproduction.

In the unlikely event that the author did not send UMI a complete manuscript and there are missing pages, these will be noted. Also, if unauthorized copyright material had to be removed, a note will indicate the deletion.

Oversize materials (e.g., maps, drawings, charts) are reproduced by sectioning the original, beginning at the upper left-hand corner and continuing from left to right in equal sections with small overlaps. Each original is also photographed in one exposure and is included in reduced form at the back of the book.

Photographs included in the original manuscript have been reproduced xerographically in this copy. Higher quality 6" x 9" black and white photographic prints are available for any photographs or illustrations appearing in this copy for an additional charge. Contact UMI directly to order.

UMI

A Bell & Howell Information Company
300 North Zeeb Road, Ann Arbor MI 48106-1346 USA
313/761-4700 800/521-0600

MECHANISMS OF LIQUID CRYSTAL AND BIOPOLYMER ALIGNMENT ON HIGHLY-ORIENTED POLYMER THIN FILMS

by

John Raymond Dennis

A dissertation submitted in partial fulfillment of the
requirements for the degree of

Doctor of Philosophy

University of Washington

1998

Approved by
Chairperson of Supervisory Committee

Program Authorized
to Offer Degree Physics

Date June 3 1998

UMI Number: 9836162

UMI
300 North Zeeb Road
Ann Arbor, MI 48103

In presenting this dissertation in partial fulfillment of the requirements for the Doctoral degree at the University of Washington, I agree that the Library shall make its copies freely available for inspection. I further agree that extensive copying of this dissertation is allowable only for scholarly purposes, consistent with "fair use" as prescribed in the U.S. Copyright Law. Requests for copying or reproduction of this dissertation may be referred to University Microfilms, 1490 Eisenhower Place, P.O. Box 975, Ann Arbor, MI 48106, to whom the author has granted "the right to reproduce and sell (a) copies of the manuscript in microform and/or (b) printed copies of the manuscript made from microform."

Signature John R. Dennis

Date June 5, 1998

University of Washington

Abstract

MECHANISMS OF LIQUID CRYSTAL AND BIOPOLYMER ALIGNMENT ON HIGHLY-ORIENTED POLYMER THIN FILMS

by John Raymond Dennis

Chairperson of the Supervisory Committee:
Associate Professor Viola Vogel
Department of Bioengineering

Molecular order can strongly enhance material properties or produce materials which perform advanced functions. Many materials, from small crystals to large macromolecules, may be aligned on highly-oriented poly(tetrafluoroethylene) (PTFE) or high-density polyethylene (HDPE) thin films, prepared by a simple shear deposition process. Here, mechanisms by which these films produce order are examined, first in a well-characterized liquid crystal, then in two more complex polymer liquid crystals, and finally in an adsorbed motor protein system.

Optical second harmonic generation (SHG) was used to study surface molecular order in the liquid crystal 4'-*n*-octyl-4-cyano-biphenyl (8CB) on PTFE and HDPE films. In nematic 8CB cells with bulk alignment along the polymer orientation axis, the surface monolayers of 8CB were also aligned, and showed C_{2v} symmetry. In the isotropic phase, the surface monolayer alignment was lost. Monolayers of 8CB evaporated onto either polymer showed little or no alignment. The bulk 8CB alignment appears to be primarily caused by surface ridges through an elastic, bulk-mediated mechanism, unlike the epitaxy-like alignment found on some cloth-rubbed polymer surfaces.

For the polymer liquid crystal poly-γ-benzyl-glutamate (PBG), uniform homogeneous surface alignment was observed on PTFE films; this is the first report of PBG surface alignment. However, liquid crystalline samples of microtubules were not aligned. PTFE films show promise for aligning some other polymer liquid crystals via elastic interactions.

The motor protein kinesin, adsorbed to PTFE films, transported fluorescently labeled microtubules predominantly in straight lines along the films' orientation axis, not in random directions as observed on glass surfaces. As the kinesin surface density was increased, the degree of alignment peaked and then declined. The results indicate that directed motion occurs because active kinesin preferentially adsorbs to surface sites along linear tracks on the film. This suggests that kinesin may be harnessed for nanoscale surface transport along predetermined tracks.

Improvements in SHG methods are also reported. Fresnel factors for buried interfaces are corrected and extended to uniaxial materials. For isotropic interfaces, a simple method is presented to measure the complete second-order susceptibility, up to an overall phase factor, without using a reference phase. This method is illustrated using 8CB monolayers.

TABLE OF CONTENTS

LIST OF FIGURES

LIST OF TABLES

ACKNOWLEDGMENTS

I would like to thank my adviser, Prof. Viola Vogel, for her constant encouragement and positive outlook, for making so much of her time available to me, and for many helpful discussions, ideas and manuscript revisions. I wish to thank the other members of the Vogel group, and also members of Prof. Pat Stayton's group, for scientific help, especially in preparing and revising talks, for help with new computer programs and other general lab tasks, and for keeping the lab environment friendly and not too serious. I am particularly grateful to Beth Smiley for getting me started on SHG experiments and for being such an entertaining office mate. Prof. Joe Howard and members of his lab, especially Dave Coy, have been generous with time and equipment in teaching me how to work with microtubules and kinesin. I also would like to thank Prof. Howard and Prof. Marjorie Olmstead for reading this manuscript and providing helpful comments, and the other members of my supervisory committee, Professors Larry Sorensen, Michael Schick and Charles Campbell, for useful discussions. Financial support was provided by NIH National Research Service Award 5 T32 GMO8268 from the National Institute of General Medical Sciences, by the NSF Engineering Resource Center UWEB, and by the Whitaker Foundation.

For all their support and encouragement in getting to this point, and past it, I am very grateful to my parents and family. Many friends have also made this long haul more enjoyable, especially Paul Vahey, Pat VanDuser, and the members of our Monday night book discussion group. Finally, for always being willing to listen or talk about work, for help through the hardest times in this project, for celebrating my successes, and for companionship, understanding and faith in me, many thanks to my wife Shelli.

1. INTRODUCTION

1.1 GENERAL OVERVIEW

Control of molecular orientation and conformation is an important factor in determining properties and functions of materials. The strength of a polymer, the optical properties of a thin film, or the performance of a liquid crystal display can depend strongly on the orientations of its constituent atoms or molecules. Molecular alignment in such systems is often induced through interactions with patterned or oriented substrates, although the mechanism of this alignment in many cases is not well understood, particularly for complex molecules.

Control of molecular orientation is critical in many biological systems, where the cooperation of many biomolecules in a precise arrangement is necessary to the systems' function. The contraction of muscle, for example, requires the interaction of a great many actin and myosin filaments in a well-ordered array, while collagen consists of a regular, staggered arrangement of polypeptide chains assembled into a strong, flexible fiber. Surfaces can also play important roles in molecular ordering within biological systems. Control of crystal morphology and orientation in biomineralization (formation of bones, shells etc.) can be determined by proteins which bind to specific crystal faces (1, 2). Other proteins such as fibronectin adopt different conformations and supramolecular structures upon binding to different types of surfaces (3). The interaction of fibronectin and other extracellular matrix proteins with surfaces plays a substantial role in determining physiological responses to biomaterials and other foreign substances. Cells cultured on surfaces with structured micron-scale topologies will align with the surface features, a phenomenon known as contact guidance (4, 5). In these and similar biological systems, precise regulation of macromolecular alignment has been refined through a long evolutionary process. Thus, studying the causes of order in such systems is a promising way to search for general physical principles which govern the alignment of complex molecules.

Consideration of such alignment processes motivates the following general questions. What molecular-scale properties of substrates are responsible for inducing molecular order in other materials? How can properties of surfaces be designed to produce alignment of biopolymers and other macromolecules; or, how can the response of such molecules to surfaces be predicted? As a step toward addressing these questions, molecular alignment on highly-oriented polymer films has been studied in this work. Films of poly(tetrafluoroethylene) (PTFE) or high-density polyethylene (HDPE) with oriented, nanometer-scale surface features are produced by a simple and inexpensive shear deposition process, making excellent test systems for alignment studies. Only more recently have other relatively simple techniques for producing controlled nanoscale surface features begun to emerge (6).

Shear-deposited PTFE films have the ability to induce orientation in a wide variety of other materials. They have previously been used to orient liquid crystals, to grow oriented crystals of a number of different materials of varying lattice types and sizes (7), and to orient proteins (8) (see also below). Within the PTFE films, the polymer chains are stretched and aligned along a single direction in a crystalline array (7). The PTFE films also have a surface topography of long straight nanometer-scale ridges and grooves, running in the same direction as the polymer chains (7). Both this nanoscale topography and the polymer chain orientation have been found to contribute to the alignment of different materials (9). Films of HDPE have similar surface structure and some aligning properties (10), but have been less well studied.

The first material aligned on these films in this work was a liquid crystal, the alignment of which was then characterized in detail using optical second harmonic generation (SHG). After this, a transition to the study of larger and more complex molecules was made using polymer liquid crystals, which share many properties with low molecular weight liquid crystals, but have been found to be more difficult to align on surfaces (11). Finally, alignment of an adsorbed protein on polymer films was studied. The polymers and proteins used were not suited to examination by SHG, and were instead studied using optical microscopy. The birefringence of the liquid crystalline materials was observed using polarized light microscopy. With differential interference contrast (DIC) microscopy or fluorescence microscopy, it was possible to observe large macromolecular polymers individually; DIC also was used to examine topographies of the polymer films.

SHG is well suited for the study of molecular order and alignment mechanisms at interfaces (see for example (12)). Because of its symmetry properties it is forbidden (at least to first order) in media with inversion symmetry, so it is interface-selective: the signal from molecules ordered at an interface can be studied in the presence of far greater numbers of the same molecules in the adjacent bulk media (13). It is sensitive enough to detect a fraction of a monolayer at an interface (14), and can serve as a non-invasive, in situ surface probe, with high temporal and spectral resolution. SHG can give information about molecular surface densities and orientations at interfaces (15, 16), progress of reactions or surface assembly processes (17), and surface potentials (18). SHG has been used to probe systems of biological interest (19), including aromatic amino acids (20, 21) and the biological chromophore retinal (22).

The chapters of this dissertation proceed from the study of small molecules to large biological polymers. In Chapter II, the alignment of a previously well-studied liquid crystal on shear-deposited PTFE and HDPE thin films was examined by SHG. The results provide a picture of the molecular orientations at the surface as well as insights about the mechanism by which the PTFE films orient liquid crystals. Chapter III is a collection of other important theoretical and experimental SHG results: corrected calculations of the nonlinear optical response from buried interfaces; an improved method for the analysis of SHG signals from isotropic interfaces; and new data on the nonlinear optical properties of the amino acid tryptophan.

The use of PTFE surfaces for aligning polymer liquid crystals, a class which includes a number of biopolymers (23), is explored in Chapter IV. Two examples are studied: a simple synthetic polypeptide, poly-γ-benzyl-glutamate (PBG), and microtubules, which are rigid tubes polymerized from the protein tubulin. It was found that the PTFE films are able to align samples of PBG, a result not previously obtained without the use of magnetic fields (24, 25). However, they failed to align samples of microtubules, and experiments planned to test the competition between surface and magnetic influences on microtubule alignment failed due to a lower-than-expected magnetic moment of microtubules. A different type of microtubule alignment experiment on PTFE films, involving the motor protein kinesin, was successful, as described in Chapter V. Kinesin motors bound to a glass surface are known to transport microtubules along the surface, with the direction of transport being random. When the kinesin was bound to PTFE films, a strong preference for microtubule motion parallel to the PTFE orientation axis was found, and the nature and causes of this alignment have been explored.

1.2 SHEAR-DEPOSITED FILM PROPERTIES AND PREPARATION

The thin oriented PTFE films used in this study were originally discovered during investigations of the friction properties of polymers (26, 27). It was found that PTFE block sliding along a smooth substrate leaves a thin film of PTFE, after an initial high-friction region which left polymer on the surface in thicker clumps. The PTFE films were estimated to be less than 10 nm thick by electron microscopy, and electron diffraction showed a high degree of polymer chain orientation along the sliding direction. HDPE produced similar (although less complete) films, but other polymers tested did not, apparently due to their less-smooth molecular profiles.

The use of the PTFE films as orienting substrates was developed by Wittmann and Smith (7), who found that the films induce alignment in crystals of a variety of small organic molecules, polymers, and inorganic materials grown on the films by various methods, as well as in liquid crystals. Additional studies have found many other materials which are oriented by these films, including alkanes (28), various aromatic and fluorescent materials (29, 30), and a number of polymers (7, 31, 32). Liquid crystal cells made from these films show good-quality homogeneous alignment, with a lower threshold voltage than rubbed polyimide cells, and are good candidates for alignment of ferroelectrics (33, 34). Proteins have also been aligned on these substrates, including silk, which crystallizes with a high content of beta sheets oriented along the films' shear direction (8), fibrinogen, (35), and myosin (36).

The PTFE films have been characterized by a variety of techniques. In the earlier studies, electron microscopy of shadowed films showed a thin PTFE layer with fine, straight ridges running in the shear direction, and electron diffraction revealed that the polymer chains were highly oriented along this direction, in a crystalline arrangement (7, 27). Several atomic force microscopy (AFM) studies have imaged the ridges and valleys of the PTFE film surfaces, revealing very long straight ridges with random height distributions typically ranging from 1 to 40 nm, and average thicknesses on the order of 10 nm (9, 37-

40). Higher-resolution AFM images show the individual PTFE chains, in the helical configuration expected in their crystalline state, oriented along the shear direction (37, 39-41). The film quality and coverage were found to depend upon the deposition temperature, with more even and complete films obtained at higher temperatures, while the speed and pressure of deposition had less effect (37, 38, 41). The polymer chain orientation within the PTFE films has also been observed by a number of other techniques, including infrared absorption spectroscopy (42), X-ray photoelectron spectroscopy (40), and high-resolution electron energy loss spectroscopy (43).

Although the PTFE films have been extensively characterized, little is known about the origins of their ability to orient other materials. One study has indicated that different mechanisms may operate to orient different materials: epitaxial lattice-matching with the oriented PTFE chains for polyethylene crystallized on PTFE films; and a graphoepitaxial alignment, due to the films' surface ridges, for crystals of 1,4-bis-2-(5-phenyloxazolyl)benzene (9).

Shear-deposited films of HDPE have been studied less than PTFE, but they have similar properties in many respects. HDPE films have been shown to induce alignment in several types of organic crystals, polymers and liquid crystals, although to a lesser extent than PTFE films (10). HDPE films also have highly-oriented, crystalline polymer chains and surface ridges similar to those found on PTFE (44-46), and good surface coverage is obtained with deposition at elevated temperatures (10).

The procedure used in this project for producing thin, highly-oriented polymer films is shown in Figure 1.1, together with a machine constructed for the film preparation in this project. Sliding a solid block of PTFE or HDPE across a substrate deposits a thin layer of polymer onto the substrate, with the polymer oriented along the sliding direction. The shear deposition machine was used to give a straight shear direction under reproducible conditions.

The polymer deposition was carried out as follows. Polymer blocks were cut to a size of approximately 1 cm by 1 cm by 3-4 cm, with a flat-milled transfer end, and sanded smooth with fine (No. 600) sandpaper. Polymers and glass or fused silica substrates were cleaned by soaking in Nochromix crystals (Godax Laboratories) dissolved in sulfuric acid for approx. 1 hour, rinsing 3 times with ultrafiltered water (18 MΩ cm resistivity), immersing in 0.05 M NaOH, rinsing 3 more times with water, and drying in an oven for 1 hour. The primary cause of film deposition problems appeared to be dust, and so the deposition machine was partly disassembled and wiped carefully with ethanol before use. In addition, the metal parts which move against other metal surfaces were wrapped with PTFE tape, to prevent formation small metal particles which were otherwise found in the system (especially where the spring compression screw contacted the compression block).

Next, the substrate was placed on a preheated hot plate, the polymer block was placed on top of it, and the housing of the shear deposition machine was lowered over the polymer, to within about 1 mm of the substrate. The spring was compressed until the lower end of the compression block reached the bottom of the window in it's slider (see Figure 1.1(b)), giving a force of about 14 N, or a nominal pressure of about 1.4×10^5 Pa. The machine was then translated across the surface one time, always in the same direction, at approximately 1 mm/s. The pressure was released, the substrate and polymer were removed, the machine was reset to its original position, and additional substrates were prepared by the same process. After the first coating, the polymer block would have a shiny spot of about 5 mm diameter in its center, seen by reflection at glancing incidence, which indicated the substrate contact area. This reduced contact area would give a better estimate of the applied pressure, roughly 7×10^5 Pa. Our experience and the AFM studies cited above indicate that the applied pressure and speed are not critical parameters, within the general range used. The temperature was more important to good film formation; temperatures of approximately 100 °C to 270 °C were used for PTFE films, and 80 °C for HDPE films.

After several uses, the shiny spot on the polymer would begin to show small lines in the shear direction, apparently from dust or particles being dragged across its surface. Up to 10 or more substrates (or as few as 1 or 2 under dirty conditions) could be coated with a polymer block before it needed renewal, by repeated sanding. For PTFE, the first polymer film would often have a thick or uneven region, as seen previously, before the block end was "conditioned". Changing the shear direction by turning the block 90° would often renew this behavior.

On glass substrates, the ridges of the PTFE films were visible by optical microscopy, either between crossed polarizers or in a differential interference contrast (DIC) configuration. It may appear surprising that they would be visible under polarized light, but this is not implausible: their retardation of the ridges, measured with a compensator, was typically only 1-2 nm, which for a ridge 50 nm high would require a birefringence of only 0.02 to 0.04. The films could also be verified by their high contact angle with water. The HDPE films were harder to examine: they were not visible under microscopy, having an index of refraction much closer to that of glass (and apparently, little birefringence), and they were less hydrophobic. Both types of films could be tested by constructing liquid crystal cells, or with an AFM. High resolution AFM images of the type published previously (37, 39-41) were not obtained here due to distortion of the soft polymer ridges by the AFM tip, but the film topography was imaged at lower magnification, as shown in Figure 1.2.

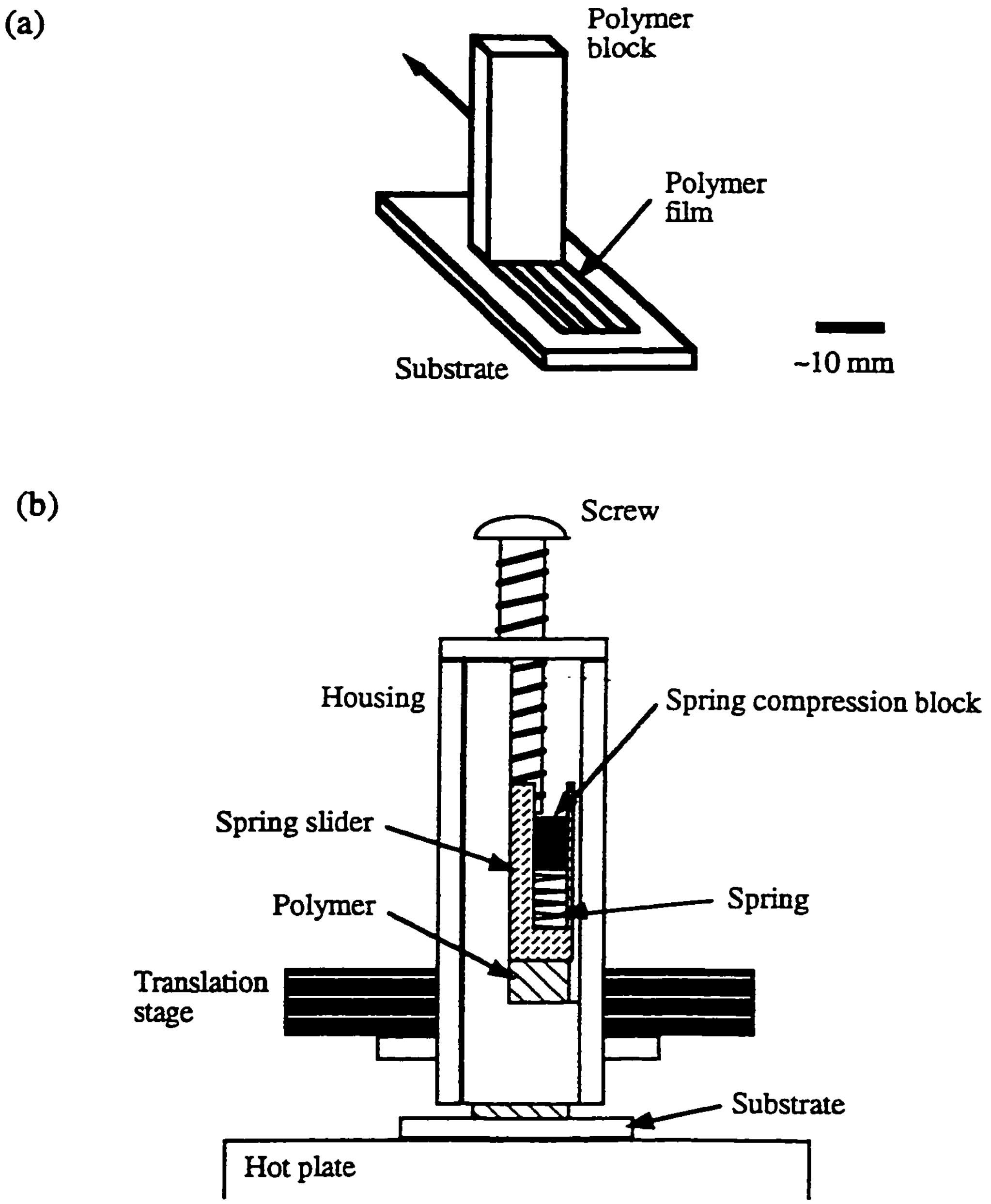

Figure 1.1: Shear-deposition process for preparing polymer films.
(a) Schematic of the film transfer process. (b) Film deposition machine. The substrate sits on a hot plate, and a motorized translation stage moves the housing containing the polymer across the substrate (into the page). A screw and moving block are used to compress the spring inside the spring slider, which presses the polymer against the substrate.

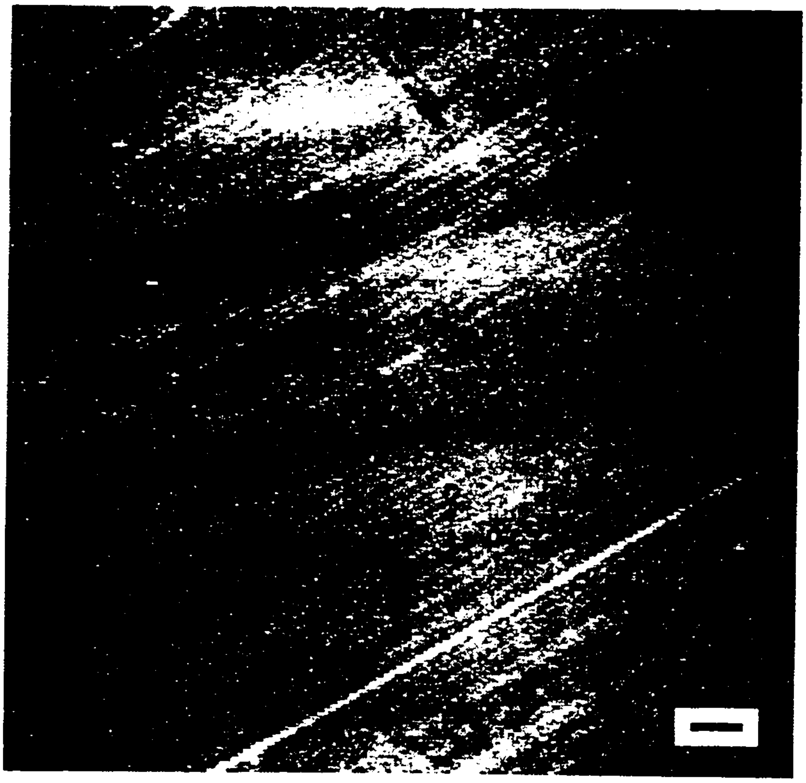

Figure 1.2: AFM image of shear-deposited PTFE film.
Polymer ridges with heights on the order of 10 nm are seen running diagonally across the image. The shade represents surface height, with a range of 20 nm from black (low) to white (high) The scale bar is 1 μm.

2. LIQUID CRYSTAL ALIGNMENT ON PTFE AND HDPE THIN FILMS STUDIED BY OPTICAL SECOND HARMONIC GENERATION

2.1 INTRODUCTION

Controlling molecular alignment via engineered surfaces is of considerable interest for tailoring material properties. Shear-deposited polytetrafluoroethylene (PTFE) thin films have an unusual ability to induce alignment in many other systems. Oriented crystal growth on these films has been demonstrated for a number of small organic molecules and polymers, grown from melts, solutions, or vapors (7). PTFE films also provide an alternative to cloth-rubbed polymer surfaces for inducing uniform liquid-crystal (LC) alignment (7), and they have been shown to induce orientation in a motor protein system, consisting of the muscle proteins actin and myosin (36). Thus the aligning ability of these films extends to a wide variety of materials and size scales. The polymer chains within the PTFE films show strong, crystalline orientation along one axis (7), and the induced order in each case is along the same axis. The films have a surface topology consisting of nanoscale ridges and grooves, which also follow this axis (39, 45).

The mechanisms behind the aligning ability of these films are not understood, and information has not been published about the surface interactions on a molecular scale. Here, we report on optical second harmonic generation (SHG) studies of the interactions of these films with a liquid crystal. The liquid crystal, 4'-*n*-octyl-4-cyano-biphenyl (8CB, Figure 2.1), provides a simple test molecule which is aligned by the films and which has a well-characterized SHG signal, allowing the orientation of the chromophores at the surface to be deduced. This information may serve as one step toward a more general understanding of alignment processes on shear-deposited polymer films.

The results of this study may also be of interest in efforts to understand the nature of liquid-crystal surface alignment. Alignment of liquid crystals has been observed using a variety of surface preparations (47), and has found widespread application in liquid crystal displays, yet the alignment processes are only partially understood. Two mechanisms, illustrated in Figure 2.2, have been proposed to explain alignment of LCs on various types of surfaces. In the first mechanism (48), alignment occurs through minimization of the bulk LC's elastic energy, for the particular topography and anchoring conditions of the surface. A typical example is a grooved glass surface with homogeneous anchoring (or anchoring at a fixed tilt angle), for which bulk distortion is minimized by alignment along the grooves. The second mechanism operates on a molecular scale, and does not depend on the bulk LC. Instead, the surface induces order in adjacent LC molecules, and this order is propagated out into the bulk. Geary *et al.* (49) showed that cloth-rubbed crystalline polymers align LCs by this mechanism, while rubbed noncrystalline polymers did not cause alignment; thus, the mechanism was compared to epitaxy, though no precise lattice matching is involved.

Shear-deposited PTFE films are prepared by a simple technique: as a solid PTFE block slides across a smooth surface, a thin, uniform layer is sheared off of the block and adheres to the surface. The polymer chains are stretched out and oriented in a crystalline arrangement along the sliding direction (7, 27, 44), and straight ridges, typically 1 to ~30 nm high and randomly spaced, also follow this direction (36, 39, 45). These films were originally studied in the context of investigating the friction and wear properties of polymers. PTFE and one other polymer, high-density polyethylene (HDPE), are distinguished by their ability to deposit even films with oriented chains; this has been attributed to their smooth molecular profile and lack of chain branching (27). Shear-deposited HDPE films, like PTFE films, have been used to grow oriented crystals of various materials and to align liquid crystals (10). Both the PTFE and HDPE films have surface features compatible with either of the alignment mechanisms described above: oriented crystalline chains and parallel surface ridges. It is possible that both mechanisms contribute to alignment.

Different LC alignment mechanisms may be distinguished with SHG by defining the role of the surface layer in bulk alignment. To a first-order (electric dipole) approximation SHG is forbidden in bulk media with inversion symmetry, so it is surface and interface selective, with a high sensitivity. At a polymer–LC interface, the signal from a polar-ordered surface layer of LC molecules can dominate the higher-order bulk LC signal and give information about surface molecular orientation (13). SHG has been used previously to demonstrate epitaxylike alignment on some cloth-rubbed crystalline polymers (50, 51).

LC monolayers adsorbed onto these polymers showed strong orientation along the rubbing direction, indicating that surface interactions produced alignment independent of the presence of the bulk LC. The surface layers of LC cells sandwiched between these substrates were also aligned and anchored strongly, even when the bulk LC was in the isotropic phase. In contrast to the rubbed polymers, surfactant-coated surfaces were found to align by the elastic mechanism (50); they produced no LC surface-layer anisotropy in either adsorbed monolayers or isotropic-phase cells, though they did align bulk LC in nematic cells.

Here we present SHG studies of the alignment of 8CB in cells sandwiched between shear-deposited PTFE or HDPE films, and in monolayers evaporated onto these films. Section 2.2 summarizes the theory behind the SHG measurements, and the data and analysis are presented in Section 2.4. Section 2.5 discusses the molecular picture which emerges for 8CB aligned on the shear-deposited polymer films, including the mechanism of alignment. It is intended that this discussion may be read with minimal reference to the technical details of the earlier sections.

2.2 THEORY

Our analysis of SHG data closely follows that of Feller *et al.* (50), with some changes to their local field factors. For SHG in reflection from a surface, the second-harmonic (SH) energy per laser pulse is:

$$S = \frac{32\pi^3\omega^2 \sec^2\theta_1(2\omega)}{c^3[\varepsilon_1(2\omega)]^{1/2}\varepsilon_1(\omega)}\left|\chi^{(2)}_{\text{eff}}\right|^2 I^2_\omega TA \qquad (2.1)$$

where ω is the fundamental frequency, $\theta_1(2\omega)$ is the SH reflection angle, $\varepsilon_1(\omega)$ and $\varepsilon_1(2\omega)$ are dielectric constants of the incident medium at ω and 2ω, and I_ω, T and A are the intensity, duration, and (effective) area of the incident laser pulse. $\chi^{(2)}_{\text{eff}}$ is the effective second-order nonlinear susceptibility, given by:

$$\chi^{(2)}_{\text{eff}} = [\hat{\mathbf{e}}(2\omega)\cdot\mathbf{L}(2\omega)]\chi^{(2)}:[\mathbf{L}(\omega)\cdot\hat{\mathbf{e}}(\omega)][\mathbf{L}(\omega)\cdot\hat{\mathbf{e}}(\omega)] \qquad (2.2)$$

where $\chi^{(2)}$ is the actual second-order susceptibility, $\hat{\mathbf{e}}(\omega)$ and $\hat{\mathbf{e}}(2\omega)$are input and output polarization vectors, and $\mathbf{L}(\omega)$ and $\mathbf{L}(2\omega)$ are local field factors. The local field factors relate the input and output fields outside the sample to the fields at the SH source position, taking into account reflection and refraction at interfaces. We have made corrections to previously published factors for this work, and have derived new expressions for use with the uniaxial nematic cells; these changes are presented in the Appendix.

We consider the case when the surface nonlinear susceptibility $\chi^{(2)}$ is dominated by a polar-ordered surface monolayer of 8CB molecules. $\chi^{(2)}$ is written as an orientational average of the molecular nonlinear polarizabilities, $\alpha^{(2)}$, which in the case of 8CB have a single dominant component (52):

$$\chi_{ijk}^{(2)} = N_s \left\langle \left(\hat{\mathbf{i}} \cdot \hat{\xi}\right)\left(\hat{\mathbf{j}} \cdot \hat{\xi}\right)\left(\hat{\mathbf{k}} \cdot \hat{\xi}\right)\right\rangle \alpha_{\xi\xi\xi}^{(2)} \tag{2.3}$$

Here, N_s is the surface density of adsorbed molecules, and $\hat{\mathbf{i}}$, $\hat{\mathbf{j}}$, and $\hat{\mathbf{k}}$ stand for $\hat{\mathbf{x}}$, $\hat{\mathbf{y}}$, or $\hat{\mathbf{z}}$, the substrate coordinates; $\hat{\mathbf{z}}$ is the surface normal, and $\hat{\mathbf{x}}$ the alignment direction for aligned monolayers (Figure 2.3(a)).

A LC monolayer aligned in one direction on a surface will in general have C_{1v} or higher symmetry, which allows six unequal nonvanishing components of $\chi^{(2)}$. The monolayers used in this work were found to have C_{2v} or higher symmetry, allowing only three unequal components. They are shown here in terms of θ, the polar angle between $\hat{\mathbf{z}}$ and the molecular axis $\hat{\xi}$, and ϕ, the azimuthal angle measured from $\hat{\mathbf{x}}$:

$$\begin{aligned}
&\chi_{zzz}^{(2)} = N_s \left\langle \cos^3\theta \right\rangle \alpha_{\xi\xi\xi}^{(2)} \\
&\chi_{zyy}^{(2)} = \chi_{yzy}^{(2)} = \chi_{yyz}^{(2)} = N_s \left\langle \sin^2\theta \cos\theta \right\rangle \left\langle \sin^2\phi \right\rangle \alpha_{\xi\xi\xi}^{(2)} \\
&\chi_{zxx}^{(2)} = \chi_{xzx}^{(2)} = \chi_{xxz}^{(2)} = N_s \left\langle \sin^2\theta \cos\theta \right\rangle \left\langle \cos^2\phi \right\rangle \alpha_{\xi\xi\xi}^{(2)}
\end{aligned} \tag{2.4}$$

The angle brackets denote angular averages, and independent distributions for θ and ϕ have been assumed. An azimuthally isotropic monolayer also has $\chi^{(2)}_{zxx} = \chi^{(2)}_{zyy}$, leaving only two independent $\chi^{(2)}$ components.

The laboratory coordinates $(\hat{\mathbf{X}}, \hat{\mathbf{Y}}, \hat{\mathbf{Z}})$ are defined as shown in Figure 2.3(a), with $\hat{\mathbf{Z}}$ the surface normal (parallel to $\hat{\mathbf{z}}$) and the laser incident in the $\hat{\mathbf{X}} - \hat{\mathbf{Z}}$ plane. Beam polarizations parallel or normal to this plane (denoted *p* or *s*, respectively) are defined by

$$\begin{aligned}\hat{\mathbf{e}}_p(\omega) &= [-\cos\theta_1(\omega), 0, \sin\theta_1(\omega)] \\ \hat{\mathbf{e}}_p(2\omega) &= [\cos\theta_1(2\omega), 0, \sin\theta_1(2\omega)] \\ \hat{\mathbf{e}}_s(\omega) &= \hat{\mathbf{e}}_s(2\omega) = [0,1,0]\end{aligned} \tag{2.5}$$

Note that the polarization vectors, local field factors, and $\chi^{(2)}_{\mathrm{eff}}$ in Eq. (2.2) have been expressed in the laboratory coordinates, while $\chi^{(2)}$ has been written in the sample coordinates; thus, $\chi^{(2)}_{\mathrm{eff}}$ depends on the sample rotation angle Φ. For SHG measurements, *p* or *s* polarizations are selected for the input and output beams, and the SH signal is recorded as Φ varies. Equations for $\chi^{(2)}_{\mathrm{eff}}$ as a function of Φ for the four polarization combinations (*p* or *s* input with *p* or *s* output) have previously been published (50). When data for each polarization combination are fit to these equations, all nonvanishing components of $\chi^{(2)}$ may be found. The distributions of the molecular orientation angles θ and ϕ may then be deduced. A Gaussian distribution is used for θ:

$$f(\theta) = F\exp\left[-\frac{(\theta-\theta_0)^2}{2\sigma^2}\right] \tag{2.6}$$

and a truncated cosine series for ϕ:

$$g(\phi) = \frac{1}{2\pi}\sum_{n=0}^{3} d_n \cos(n\phi) \tag{2.7}$$

where F and d_0 are normalization constants ($d_0 = 1$), θ_0 is the average value of θ, and σ is the variation. Positive d_2 indicates preference for azimuthal angles near the $\hat{\mathbf{x}}$ axis rather than the $\hat{\mathbf{y}}$ axis, and d_1 and d_3 show preference for the $+\hat{\mathbf{x}}$ direction over $-\hat{\mathbf{x}}$.

When bulk 8CB is present in addition to the polar-ordered surface monolayer, there is an additional bulk nonlinearity which alters $\chi^{(2)}_{zzz}$, $\chi^{(2)}_{zxx}$, and $\chi^{(2)}_{zyy}$. The fit is carried out as before, and then the calculated bulk contribution is subtracted out in the manner described by Feller *et al.* (50) before finding the angular distributions $f(\theta)$ and $g(\phi)$.

2.3 EXPERIMENTAL ARRANGEMENT

Shear-deposited PTFE and HDPE films were prepared by sliding flat polymer blocks across fused silica slides in a motorized machine. Temperatures of approximately 100 °C for PTFE and 80 °C for HDPE were used, as they gave more complete and reproducible surface coverage than lower temperatures. The applied pressure and speed were also controlled, and were on the order of 10^5 Pa and 0.5 mm/s, respectively. Before use, slides and polymer blocks were cleaned in Nochromix glass cleaner, rinsed three times in 18 MΩ-cm water, soaked in 0.05 M NaOH, rinsed three times in water again, and dried in an oven. The topography of selected PTFE and HDPE films was examined with an atomic force microscope (AFM) (45). Each type of surface showed long straight ridges running uniformly in the polymer shear direction, similar to those seen previously on PTFE (39).

8CB (British Drug House K-24, Figure 2.1) generates a strong SHG signal and has been used in numerous SHG studies (53). It is a smectic A liquid crystal at room temperature, and becomes nematic above 33.5 °C and isotropic above 40.5 °C. To form cells, pairs of slides with PTFE or HDPE films were placed together with their shear directions opposite. Spacers of No. 00 cover glass (FGR Steinmetz Inc., Surrey, BC, Canada) at the cell corners gave a gap of approximately 75 μm between the slides. The gap was filled by capillary action with 8CB in the isotropic phase. Bulk alignment in cells was monitored with a polarized light microscope in a reflection geometry. When cooled to the nematic or smectic phase, the 8CB cells prepared with polymer-coated slides showed uniform alignment along the polymer orientation direction (Figure 2.4). Evaporated 8CB monolayers were prepared by heating an 8CB drop to approximately 75 °C in close proximity to a surface, while monitoring the SHG signal (15).

In the SHG measurements, a Q-switched frequency-doubled Nd:YAG laser, with a repetition rate of 10 Hz, was used as the fundamental beam (Figure 2.3). The beam energies used were 2.5–5 mJ per pulse. 8CB has an absorption peak near the second-harmonic wavelength (266 nm), giving resonant enhancement of the signal. The beam was incident on the sample at an angle of 60° to the surface normal, after passing through a half-wave plate, a polarizer, a converging lens, and a 475 nm cutoff long-pass filter. The lens reduced the beam spot area on the surface to about 2 mm^2. The reflected beam passed through a filter (Corning CS 7-54), which removed the fundamental radiation, a second lens, an analyzer, a focusing lens, a monochromator, and a second CS 7-54 filter before being detected by a photomultiplier tube with a gated integrator. Data points are 30 or 60 s averages of the SH signal. The microscope was positioned to monitor bulk alignment at the location probed by SHG.

For 8CB cells, a laser mirror which reflects at 367 nm (TLM1-367-0 from CVI Laser) was inserted into the reflected beam after the first CS 7-54 filter. This mirror transmitted the SH signal at 266 nm, and reflected a large peak, which was centered near 370 nm. Without the mirror, the small fraction of this peak which reached the detector was large enough to distort the SHG data. The peak was about 40 nm wide, unpolarized, and uncollimated, and was absent for 8CB monolayers. It appears to be excimer fluorescence generated by the bulk 8CB, similar to an 8CB excimer reported previously (54).

The relative phases of signals from 8CB monolayers on different surfaces were also measured (55). For these measurements, a z-cut quartz plate is inserted in the beam path after the sample and before the fundamental-beam filter (Figure 2.3(c)), and generates a second SH signal in transmission. Due to the (small) dispersion of air, the phase difference between the quartz signal and the sample signal depends on the sample-to-quartz distance. The quartz is translated along the beam path to produce an interference pattern, described by

$$S = A + B\cos\left(2\pi\frac{l}{T} + \psi\right), \tag{2.8}$$

$$T = \lambda_0/(2n_1(2\omega) - 2n_1(\omega)) \tag{2.9}$$

where S is the SH intensity, A and B are constants, l is the quartz position, T is the distance between peaks, ω and λ_0 are the frequency and vacuum wavelength of the fundamental, and $n_1(\Omega)$ is the refractive index of air at frequency Ω. For air (56), $n_1(2\omega) - n_1(\omega)$ is 1.98×10^{-5}. The difference in phase angles, ψ, for different samples gives the relative phases of their SH signals.

2.4 RESULTS

In this section we present SHG data for 8CB cells and evaporated monolayers, and describe how the surface orientation distributions of 8CB are extracted from the data. First, the SHG data are fit to find the second-order susceptibility $\chi^{(2)}$. The phases of the monolayer signals are measured to determine whether the heads of the 8CB molecules point toward or away from the surface. The susceptibilities for the 8CB cells are then divided into surface and bulk terms. Finally, the surface susceptibilities are used to find the orientation parameters of Eqs. (2.6) and (2.7). The main parameters of interest are θ_0, which is the average tilt angle from the surface normal, and d_2, which describes the degree of in-plane alignment along the polymer orientation axis.

SHG data and fits for PTFE and HDPE cells containing 8CB are shown in Figure 2.5, for both the isotropic and nematic phases of the bulk 8CB. The polymer shear direction is 0° in each plot. The s-in s-out polarization gave only a small background signal, and is not shown or used in the fits; the same is true for the p-in s-out signal in the isotropic phase. For the fits, the square root of the signal is written as a (linear) function of the independent components of $\chi^{(2)}$. Thus, a system of many equations is generated, one for each choice of Φ and the polarization combination. Each such system of equations was fit by simultaneous variation of the allowed $\chi^{(2)}$ components. The nematic fits were calculated for C_{2v} symmetry, under which the 0° and 180° directions are equivalent, and also for the more general C_{1v} symmetry. The C_{1v} fit matched the C_{2v} fit closely, indicating that the samples have C_{2v} symmetry; the C_{2v} fits are the ones shown.

For the nematic phase, the local field factors of Eq. (2.2) are non-diagonal (see the Appendix), but the off-diagonal terms were found to be small, and our fits were carried out using the diagonal terms only. To test this approximation, the $\chi^{(2)}$ resulting from the fit was used to generate fit curves with both the diagonal matrices and the full matrices. The two sets of fit curves agreed quite well, with largest errors of 4% for p-in s-out at $\Phi = 45°$ and 1% for the other polarization combinations. The full matrices predict a small s-in s-out signal even for a sample with C_{2v} symmetry, while for the diagonal matrices this is not allowed.

SHG data and fits for 8CB monolayers evaporated onto PTFE and HDPE films are shown in Figure 2.6. As in the isotropic-phase cell, the p-in s-out polarization combination gave only a small background signal. The fits for the monolayers, as well as for the isotropic cells, show little difference between $\chi^{(2)}_{zxx}$ and $\chi^{(2)}_{zyy}$, indicating azimuthal isotropy in the SH signal. For the nematic cells, $\chi^{(2)}_{zxx} > \chi^{(2)}_{zyy}$, showing 8CB alignment along the polymer orientation direction.

On silica surfaces, monolayers of 8CB adsorb with the cyano head groups pointing toward the surface (55). On some surfactant-coated glass surfaces, partial monolayers of polar-ordered 8CB molecules have been found, with the remainder of the surface covered by 8CB molecules in an antiparallel arrangement, which does not contribute significantly to the SHG signal (15). For evaporated 8CB on PTFE and HDPE films, fits to the data give surface coverages (N_s) which are roughly half to three quarters of the fused silica coverage, varying from sample to sample.

Phase measurements were used to show that the polar-ordered 8CB molecules on PTFE and HDPE had their heads facing the surface, as on fused silica. The opposite orientation should produce a phase shift of π in the signal, relative to the 8CB-silica signal. Results for each type of surface are shown in Figure 2.7. The changes in peak heights are caused by the widening profile of the fundamental beam along which the reference quartz is translated. Fits to Eq. (2.8), with a linear term added, are also shown in Figure 2.7. The peak separation T in the fits is fixed at 13.9 mm, in agreement with the value calculated from Eq. (2.9). The phases for PTFE and HDPE differ from the silica phase by less than $\pi/8$. The presence of the PTFE and HDPE films has some effect on the phase relative to fused silica, by adding an extra phase term to the local field factors of Eq. (2.2). However, the calculated change in phase due to this effect was small, approximately $\pi/30$ for PTFE and $\pi/120$ for HDPE.

For the 8CB cells, the susceptibilities obtained from the fits may contain both surface and bulk contributions. We wish to isolate the surface contribution. We first present qualitative evidence that there is a significant surface contribution. When exposed to laser intensities of roughly twice the normal measurement intensity for several tens of minutes, 8CB cells showed substantial signal decreases (up to 50% for the *s*-in, *p*-out polarization). The decreases were irreversible and were localized at the exposed spots, indicating that the lost signal had come from surface-bound molecules. In contrast, no signal loss was seen with much longer exposure times for a monolayer of 8CB spread at the air-water interface, or for a free surface of isotropic-phase bulk 8CB; the molecules in these systems are free to move rapidly.

The surface susceptibility is found by subtracting out the bulk contribution, which has previously been published (13, 50). This requires that the absolute magnitude of the signal be calibrated, and that the relative phases of the surface and bulk terms be known. For 8CB cells in which the 8CB heads point toward the surface, it has previously been found that the surface and bulk terms are approximately opposite in phase (13, 50). The phase measurements described above indicate that this should hold for the PTFE and HDPE cells used here. Our signal magnitudes were calibrated using 8CB monolayers on water (52, 57). The magnitudes for our cells in the nematic and isotropic phases were smaller than for the monolayer on water, but substantially larger than published values for the bulk, and also larger than our measured signal for the free surface of isotropic 8CB. After subtracting out the bulk signal, we find for the PTFE and HDPE cells that the surface coverage N_s is roughly half to three-quarters of a monolayer, similar to the coverage for the evaporated 8CB layers on PTFE and HDPE. This coverage represents the fraction of the surface which is covered by polar-ordered 8CB.

The orientation parameters describing surface molecular alignment are found from the surface susceptibilities, for cells, and from the total susceptibilities for evaporated monolayers, since these have no bulk contribution. The C_{2v} symmetry of the fits means that d_1 and d_3 of Eq. (2.7) are zero, and that θ and σ cannot be determined independently. We set $\sigma = 0$ to calculate θ_0; $\sigma = 5°$ would give slightly larger values. The value of d_2 is independent of the value chosen for σ, since d_2 can be determined from the ratio $\chi^{(2)}_{zxx}/\chi^{(2)}_{zyy}$, which is independent of the θ distribution. The values of d_2 and θ_0 for PTFE and HDPE are listed in Table 2.1.. The values of d_2 obtained here for surface monolayers in nematic cells are comparable to those obtained by Feller *et al.* (50) for polyimide surfaces and indicate strong alignment. The d_2 values for isotropic cells and evaporated monolayers indicate no alignment or slight alignment at the surface.

2.5 DISCUSSION

The SHG data for evaporated 8CB layers on PTFE and HDPE films show that a fraction of the 8CB molecules assume a polar arrangement, with their heads toward the surface. This polar arrangement covers roughly half to three-quarters of the surface, despite the hydrophobic nature of the polymers. Previously, glass surfaces coated with hydrophobic layers of octadecyltrichlorosilane (OTS) have been found to adsorb approximately one-tenth to one-sixth of a polar-ordered 8CB layer, with the remainder of the surface covered by 8CB molecules in an antiparallel arrangement (15, 58). For glass coated with *n,n*-dimethyl-n-octadecyl-3-aminopropyltrimethoxysilylchloride (DMOAP), the polar 8CB coverage was about two thirds of a monolayer (15). In each case, the heads of the polar-ordered 8CB faced toward the hydrophobic substrate. With the OTS coating, 8CB is exposed to a close-packed array of hydrocarbon chains that are oriented normal to the surface. The hydrocarbon chains are more loosely packed in the case of DMOAP, with the headgroups occupying approximately twice the cross-sectional area of the chains, leading to enhanced polar ordering of 8CB. It is, hence, not surprising that a fraction of the 8CB orients with the polar headgroups toward the shear-deposited PTFE and HDPE films, but the reason for the relatively large extent of polar order on these films is not clear. It appears that the 8CB is not strongly anchored, since it can easily be reoriented (as described below). It is likely that the polar order is related to properties of these thin, sheared polymer films which differ from the properties of the bulk polymers. The films have a very structured surface topology, which in the case of PTFE provides sites for oriented nucleation of a wide variety of crystals, and which may also allow anchoring of 8CB molecules. Also, the films are very thin, with the substrate possibly exposed between some of the polymer ridges (although AFM images indicate that the exposed areas would be very small).

In addition, the configuration of neighboring 8CB dipoles at the surface may contribute to the amount of polar ordering. On all of the surfaces used in this study, the 8CB molecules are tilted away from the surface normal by similar, large angles (θ_0 in Table 2.1). Previous studies have found the same large tilt angles on a wide variety of different surface types, and have attributed this to the fact that this tilt angle greatly reduces interactions between neighboring dipoles (13, 50, 52).

In the plots of Figure 2.5 and Figure 2.6, it is clear that the SHG data for the isotropic-phase 8CB cells and the 8CB monolayers are similar to each other, but very different from the data for the nematic cells. The isotropic cell and monolayer signals indicate little or no alignment along the polymer orientation direction, while the nematic cell signals indicate strong alignment. After the bulk contributions to the cell signals are subtracted, the azimuthal orientation parameters d_2 (Table 2.1) confirm that the same trends are found in the surface signals: the 8CB surface layers in the isotropic-phase cells show lack of orientation similar to the evaporated monolayers, while the surface layers in nematic cells are well aligned. The isotropic cell data were taken after the cells had been aligned in the nematic phase for several hours, starting within fifteen minutes after they were re-heated to the isotropic phase. The surface monolayer appears to be rearranged as the bulk nematic-isotropic transition is crossed.

We see then that the PTFE and HDPE films do not align 8CB molecules in contact with them when the bulk 8CB is isotropic, or when no bulk phase is present. In addition, the surface molecules are not strongly bound in one orientation, but are able to reorient easily. This indicates that the epitaxy-like aligning effect described by Geary *et al.* (49) does not act strongly in these systems, if at all. The excellent bulk alignment observed must be due to the surface ridges and grooves acting on the bulk LC through an elastic mechanism. Orientation within the surface layer of 8CB would then follow the bulk orientation.

These results are quite different than those found for cloth-rubbed surfaces of polyimide (PI) (50, 51) For cells made from those surfaces, the isotropic and nematic plots are quite similar to each other, and also fairly similar to plots for monolayers; in each case, the signal comes primarily from an 8CB surface layer, which is aligned along the rubbing direction. For the cells, surface monolayer alignment persisted at temperatures well above the isotropic transition temperature, indicating strong surface anchoring. This alignment is through the epitaxylike mechanism. The 8CB surface layers in these samples show C_{1v} symmetry: the numbers of molecules tilted parallel and antiparallel to the rubbing direction are not equal. This symmetry would be inconsistent with elastic alignment by simple ridges, on which either direction is equivalent, but the C_{2v} symmetry of the PTFE and HDPE nematic cells is consistent with elastic alignment.

On the PTFE films, the surface features which induce aligned crystal growth are different than those which produce LC alignment. LC alignment by the elastic mechanism involves surface features which are much larger than the molecular scale, while the oriented growth of crystals should involve interactions of molecules or small clusters with molecular-scale surface features. The random nature of the ridge heights and spacings gives a continuous distribution of different ridge sizes. The PTFE films also induce a mix of polar and nonpolar configurations in 8CB molecules at the surface, suggesting that different topographical features on the films may interact differently with adsorbates, perhaps creating linear patterns of nucleation. The polar-ordered molecules are not azimuthally anchored, but are able to easily reorient. The combination of weak surface interactions and linear patterning on many different size scales together may play a large part in the orienting capabilities of these PTFE films.

Table 2.1: Fit parameters from SHG data for 8CB at polymer film surfaces and interfaces.

θ_0 is the average molecular tilt with respect to the surface normal (Eq. (2.6)), and d_2 describes the degree of in-plane alignment along the polymer orientation axis (Eq. (2.7)). For an unaligned monolayer d_2 is zero, while values near 0.5 indicate strong alignment. Uncertainties were estimated by finding the variations needed to increase the sum of squared deviations of the fits by 50%.

Polymer and configuration	d_2	θ_0 (degrees)
PTFE nematic cell	0.49 ± 0.07	73 ± 1
PTFE isotropic cell	0.06 ± 0.04	72 ± 1
PTFE monolayer	0.09 ± 0.04	73 ± 1
HDPE nematic cell	0.50 ± 0.08	73 ± 1
HDPE isotropic cell	0.04 ± 0.04	70.8 ± 0.6
HDPE monolayer	-0.03 ± 0.04	69.0 ± 0.6

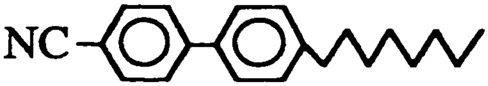

Figure 2.1: Chemical structure of 4'-*n*-octyl-4-cyano-biphenyl (8CB).

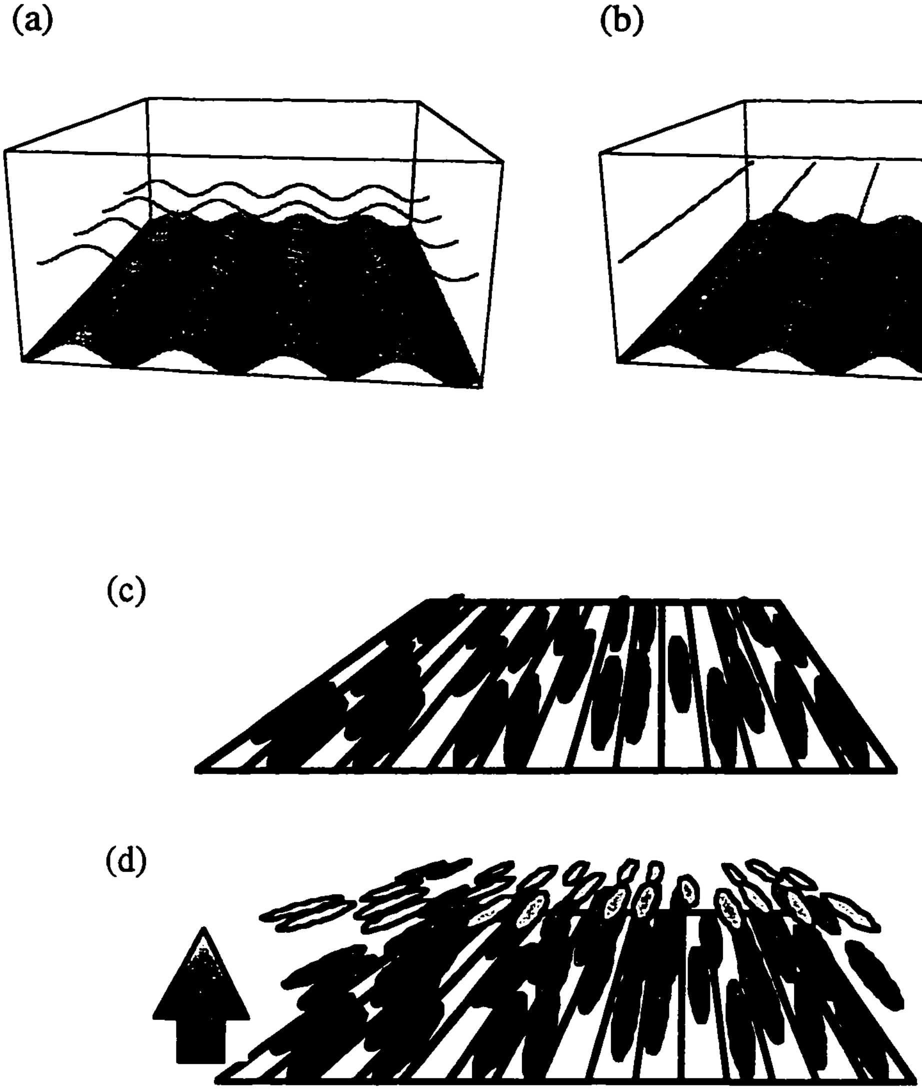

Figure 2.2: Elastic and epitaxy-like mechanisms of liquid crystal alignment. (a) In the elastic mechanism, macroscopic surface ridges deform the bulk director (solid lines) of a liquid crystal with homogeneous boundary conditions oriented across the ridges. (b) The undeformed alignment parallel to the ridges is a lower-energy state. (c) In the epitaxy-like mechanism involves,g LC molecules are anchored at the surface with a preferred orientation, and (d) this preferred orientation is propagted into the bulk

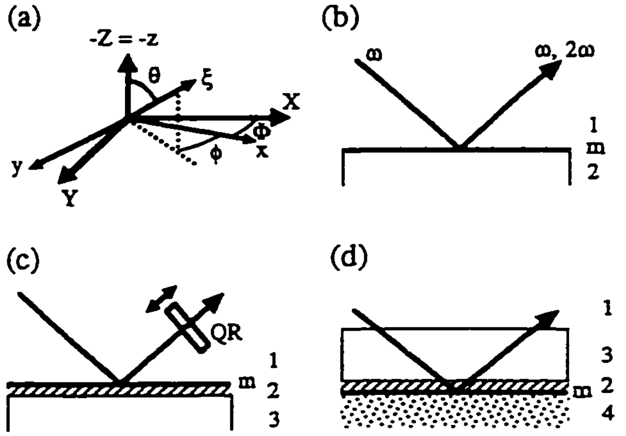

Figure 2.3: Sample geometries for SHG.

(a) Relations between coordinate systems, where ξ is a representative molecular axis, related by angles θ and ϕ to the sample coordinates, which are in lower case letters. Φ is the rotation angle between the sample and laboratory coordinates (capital letters). The laser plane of incidence is the XZ plane. (b) Schematic of SHG from a monolayer "m" at an interface. (c) and (d) SHG configurations for LC monolayers and cells, respectively, where medium 1 is air, 2 is polymer, 3 is silica, and 4 is bulk LC. The heavy lines "m" show the interfaces which generate SH signals. The translatable quartz "QR" shown in (c) is present only during phase measurements.

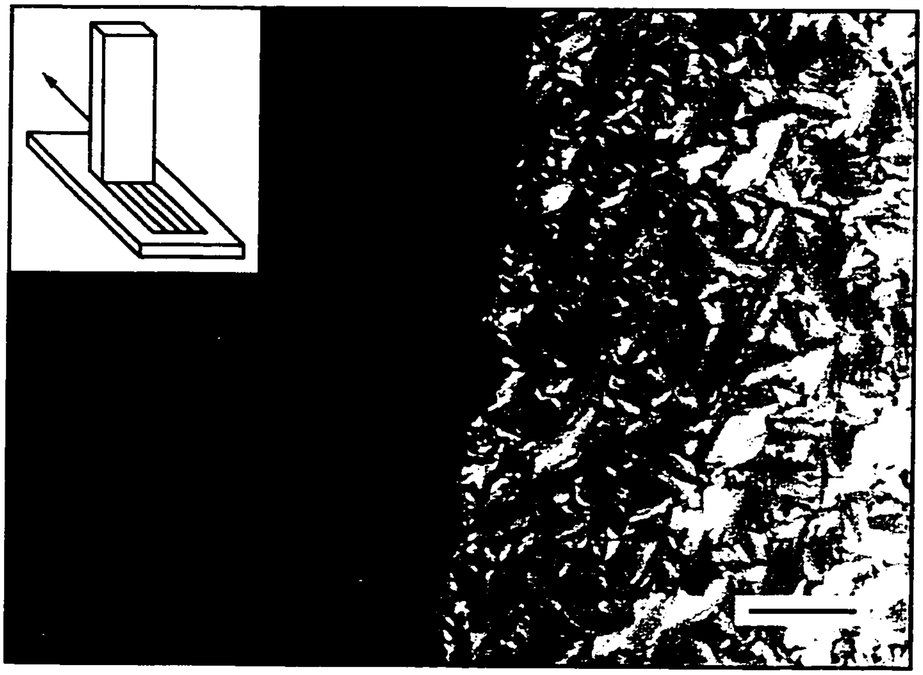

Figure 2.4: Alignment of 8CB in the smectic A phase by a PTFE film. The cell is viewed by optical microscopy between crossed polarizers. The edge of the PTFE-aligned region is shown, with the right side displaying unaligned 8CB on the untreated area of the slide. The aligned 8CB on the left is oriented at 10° from its extinction angle, so that some texture is seen. The inset depicts the polymer film deposition procedure. The scale bar is 30 μm.

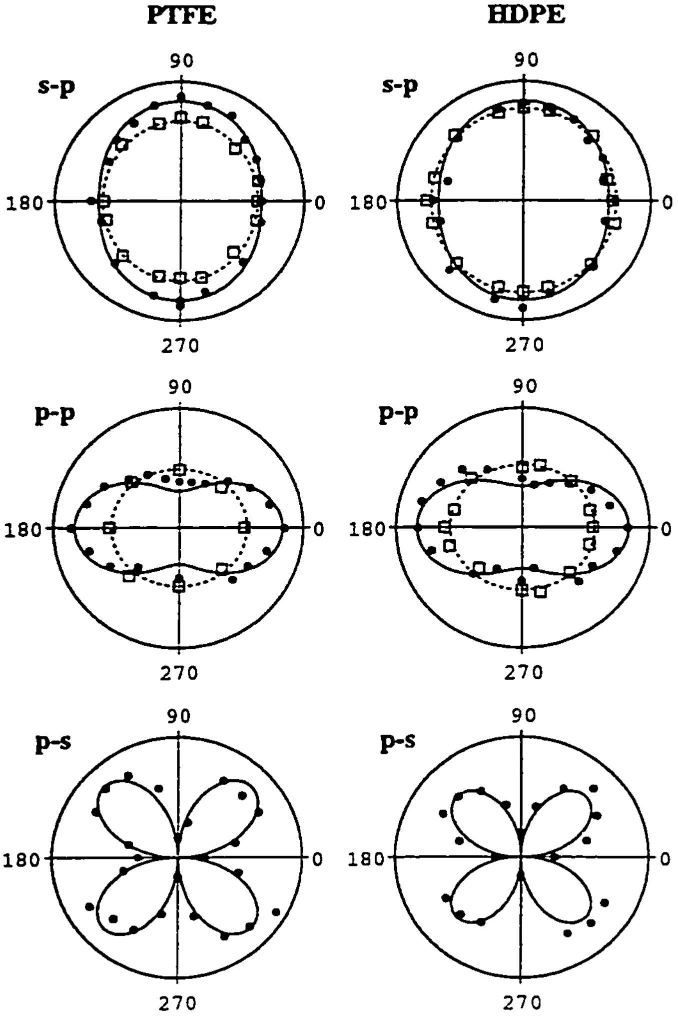

Figure 2.5: Square root of second-harmonic intensity (arbitrary units) vs. sample rotation angle Φ for 8CB cells with films of PTFE and HDPE. Φ=0° defines the polymer shear direction. The filled circles and solid lines are data and fits for the nematic phase of the bulk 8CB, and the open squares and dashed lines are for the isotropic phase. The plot labels give the polarization combinations: *s-p* is *s*-in, *p*-out. The plots are scaled differently, with the *p-p* and *p-s* scales being approximately 77% and 33%, respectively, of the *s-p* scale.

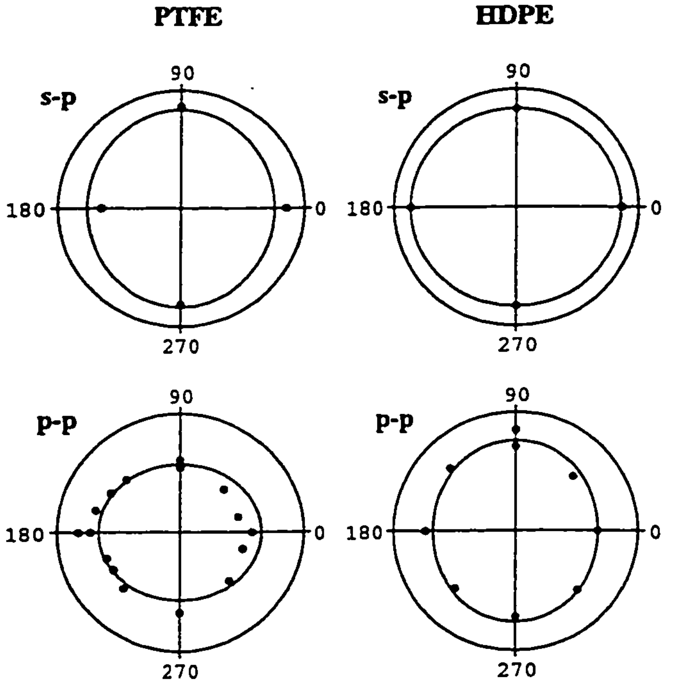

Figure 2.6: Square root of second-harmonic intensity (arbitrary units) vs. sample rotation angle Φ for 8CB monolayers evaporated onto PTFE and HDPE films.
The lines are fits to the data, and the plot labels give input and output polarizations.

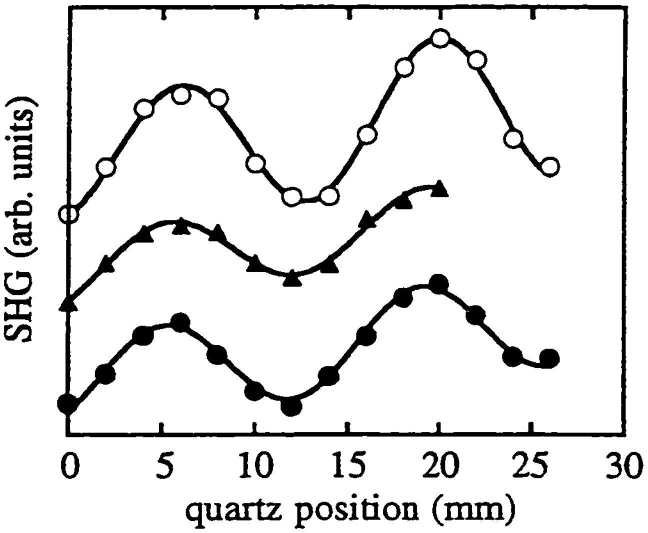

Figure 2.7: Interference between SHG signals from evaporated 8CB monolayers and a quartz reference, giving the relative phases of the monolayer signals.

SH intensity (arbitrary units) is plotted vs. position *l* of the quartz reference for monolayers on a PTFE film (filled circles), an HDPE film (triangles), and a bare fused silica slide (open circles). Data for different surfaces are offset vertically, and the origin of *l* is arbitrary. Solid lines are fits to Eq. (2.8), with a linear term added.

3. SECOND HARMONIC GENERATION: TECHNIQUE IMPROVEMENTS AND APPLICATIONS TO ISOTROPIC SURFACES

3.1 INTRODUCTION

Optical second harmonic generation (SHG) is a powerful tool for studying molecular order and other properties of interfaces, and has been applied to a variety of different types of surfaces (12). This chapter combines technique extensions and improvements with data used to illustrate the measurement technique and to test and calibrate the experimental system. The data also provide some new insights into the properties of some previously-studied surfaces.

The equation describing the second-harmonic signal generated at an interface (Eqs. 2.1, 2.2) contains local-field factors, which contain the Fresnel factors and may also include microscopic local-field effects, such as induced-dipole interactions (59). For SHG studies at simple surfaces such as the air-water interface, the Fresnel factor contributions have been discussed in the literature (60-62). Section 3.2 addresses the adaptation of these factors for studies of buried interfaces, such as presented in Chapter 2. A correction is made to a result published previously for buried interfaces. The results are also extended to the case in which one of the material layers is uniaxial, with the extraordinary axis oriented at an arbitrary angle within the sample plane. A comparison with local field factors derived by a slightly different method is presented in Appendix A.

For isotropic interfaces, Section 3.3 presents a method of analyzing both the magnitude and phase information which is contained in the SH signal, without the use of a variable phase reference signal. The method involves using a quarter wave plate and polarizer to null the signal, for several input-beam polarizations. This allows determination of the magnitudes and phases of all components of the second-order nonlinear susceptibility, up to an overall phase factor. The results are similar to the results of a rotating-wave-plate method presented recently (63-65), and the nulling method has a simpler data analysis.

The nulling method is also especially well-suited to tests of different models of local field factors.

The nulling method of Section 3.3 is applied in Section 3.4 to monolayers of 8CB at the air-water interface, and in Section 3.5 to the free surface of isotropic-phase 8CB. The 8CB monolayer is a reproducible reference system, well-studied previously (52, 57, 66). It is found to fit a simple interface model to a good approximation, and is used as a calibration of absolute signal magnitudes. The nulling method of analyzing the data also reveals some small deviations of the 8CB monolayer signal from the simple interface model used. These deviations may be explained by adjustments to the local field factors, for example by including a complex dielectric constant for the 8CB at the SH frequency. For the free surface of 8CB, the SHG data contains both surface and bulk contributions, with different phases. The phases and magnitudes of all nonlinear susceptibility components are found, with only the overall phase undetermined.

Section 3.6 addresses the SHG signal from the amino acid tryptophan, which has potential applications as a probe of peptide orientation at interfaces. Previous measurements for tryptophan at the air-water interface (67), which yielded the absolute magnitude of the surface susceptibility, have been taken with the same SHG experimental setup used in this work. The previous data had also indicated that the dominant contribution to the signal came from a single component of the molecular nonlinear polarizability, $\alpha^{(2)}$. However, in the course of this work it was found that the setup needed a modification, which affects the single-component conclusion for $\alpha^{(2)}$. New data are presented which show that $\alpha^{(2)}$ does not have a single dominant component. The previous measurement of the absolute signal magnitude is unaffected by this change, and should still be correct.

3.2 LOCAL FIELD FACTORS FOR LIQUID CRYSTAL CELLS

The local field factors in Eq. (2.2) relate the incident laser field and the detected SHG to the fields at the interface where the signal is generated. In general they may include both Fresnel factors and microscopic local field effects, but the ones discussed here include only Fresnel factors. Local field factors for a monolayer at an interface (12) (modeled as shown in Figure 2.3(b)) have previously been extended to cover LC monolayers and cells with polymer aligning layers (50) (Figure 2.3(c) and (d)). We have used a corrected form of the factors for cells, presented here with justification for the corrections; we also present equations for the case of a uniaxial LC, which we have used for cells in the nematic phase.

Input and output local field factors are taken to be diagonal matrices, except in the case of a uniaxial LC. The input factors $\mathbf{L}(\omega)$ are defined simply as $L_{ij}(\omega) = E_{i,\mathrm{source}}/\mathrm{E}_{j,\mathrm{incident}}$, while the outputs $\mathbf{L}(2\omega)$ are defined by (50)

$$E(2\omega) = \frac{4\pi i \omega \sec\theta_1(2\omega)}{c\sqrt{\varepsilon_1(2\omega)}}\left[\hat{\mathrm{e}}(2\omega)\cdot\mathbf{L}(2\omega)\cdot\mathbf{P}^s(2\omega)\right] \tag{3.1}$$

where $E(2\omega)$ is the SH field at the detector and $\mathbf{P}^s(2\omega)$ is an induced polarization sheet (i.e., the SH source induced by the fundamental beam). With these definitions, the local field factors reduce to 1 if the dielectric constants of all layers in the system are equal. The induced polarization sheet is infinitesimally thin (too thin to affect ordinary refraction at the interface), but has an index of refraction distinct from the adjacent media.

The local field factors for a second harmonic source at an interface between two bulk media, as in Figure 2.3(b), have been presented previously (12, 60). The input factors, shown here for reference, are:

$$\begin{aligned}
L_{xx}(\omega) &= \frac{2n_1(\omega)\cos\theta_2(\omega)}{n_2(\omega)\cos\theta_1(\omega) + n_1(\omega)\cos\theta_2(\omega)} \\
L_{yy}(\omega) &= \frac{2n_1(\omega)\cos\theta_1(\omega)}{n_1(\omega)\cos\theta_1(\omega) + n_2(\omega)\cos\theta_2(\omega)} \\
L_{zz}(\omega) &= \frac{2n_1^2(\omega)n_2(\omega)\cos\theta_1(\omega)}{n_m^2(\omega)[n_2(\omega)\cos\theta_1(\omega) + n_1(\omega)\cos\theta_2(\omega)]}
\end{aligned} \tag{3.2}$$

where n_1, n_2 and n_m are the indices of refraction of the bulk media and monolayer. The output local field factors have exactly the same form, with the indices and angles at ω

replaced by values for 2ω. For monolayers on top of thin polymer films, as in Figure 2.3(c), we have used the previously published local field factors.

Next, the derivations of the local field factors for the LC cell of Figure 2.3(d) are shown, because we have made corrections to the versions which were published previously (50). Only the p polarization will be shown, since no corrections were made for the s polarization. As in Chapter 2, for an LC cell the layers represent (top to bottom): air (1), silica (3), polymer (2), LC (4). For the input factors, we begin by relating the input field in medium 1, $E_{1p}(\omega)$, to the field in medium 4, $E_{4p}(\omega)$:

$$E_{4p}(\omega) = t_p t_{13p} E_{1p}(\omega) \tag{3.3}$$

where t_{13p} is the Fresnel transmission coefficient from medium 1 to medium 3 with p polarization. The transmission from medium 3 to medium 4, including multiple reflections within medium 2, is described by $t_p = t_{32p} t_{24p} e^{i\beta} / \left(1 + r_{32p} r_{24p} e^{2i\beta}\right)$, where r_{abp} are Fresnel reflection coefficients from medium a to medium b, $\beta = \left(2\pi/\lambda_o\right) n_2 h_2 \cos\theta_2(\omega)$, λ_o is the laser wavelength in vacuum, and h_2 is the polymer layer thickness. The previously published (incorrect) local field factors would be obtained by simply taking x and z components of the fields in Eq. (3.3):

$$E_{4x}(\omega) = t_p t_{13p} E_{1x}(\omega) \qquad E_{4z}(\omega) = t_p t_{13p} E_{1z}(\omega) \tag{3.4}$$

This is incorrect because E_{1p} and E_{4p} are magnitudes of vectors which are not parallel. Instead the following equations are used to substitute for the fields in Eq. (3.3):

$$\begin{aligned} E_{1x}(\omega) &= -E_{1p}(\omega)\cos\theta_1(\omega) \qquad & E_{4x}(\omega) &= -E_{4p}(\omega)\cos\theta_4(\omega) \\ E_{1z}(\omega) &= E_{1p}(\omega)\sin\theta_1(\omega) \qquad & E_{4z}(\omega) &= E_{4p}(\omega)\sin\theta_4(\omega) \end{aligned} \tag{3.5}$$

This gives the correct relations between x and z components:

$$E_{4x}(\omega) = t_p t_{13p} E_{1x}(\omega) \frac{\cos\theta_4(\omega)}{\cos\theta_1(\omega)} \qquad E_{4z}(\omega) = t_p t_{13p} E_{1z}(\omega) \frac{\sin\theta_4(\omega)}{\sin\theta_1(\omega)} \tag{3.6}$$

Then, the fields inside the monolayer are substituted for the fields in medium 4, using the continuity of tangential E components and normal D components across the interface. The final input local field factors (with y included for reference) are then:

$$
\begin{aligned}
L^c_{xx}(\omega) &= t_p t_{13p}\frac{\cos\theta_4(\omega)}{\cos\theta_1(\omega)} \\
L^c_{yy}(\omega) &= t_s t_{13s} \\
L^c_{zz}(\omega) &= t_p t_{13p}\left[\frac{n_4}{n_m}\right]^2 \frac{\sin\theta_4(\omega)}{\sin\theta_1(\omega)} = t_p t_{13p}\frac{n_4 n_1}{n_m^2}
\end{aligned}
\qquad (3.7)
$$

If h=0 then $t_k = t_{34k}$, and if in addition $n_3 = n_1$, then Eq. (3.7) reduces to Eq.

(3.2), as expected. The uncorrected version of Eq. (3.7) did not take the proper form in this limit, demonstrating the need for a correction. For isotropic 8CB cells, the correction changes the magnitudes of $L^c_{zz}(\omega)$ and $L^c_{xx}(\omega)$ by factors of 0.64 and 1.66, respectively, while $L^c_{yy}(\omega)$ is unchanged.

The output local field factors for the same case are now derived, again for p polarization only, to show that the same corrections result. The field radiated into medium 2 by a polarization sheet at the interface (which is not the total field in medium 2, since multiple reflections aren't included) is found using Eq. (3.1):

$$E'_{2p} = \frac{4\pi i\omega\sec\theta_2}{c\sqrt{\varepsilon_2}}\left[\cos\theta_2 L^R_{xx}P^s_x + \sin\theta_2 L^R_{zz}P^s_z\right] \qquad (3.8)$$

where $L_{xx}{}^R$ and $L_{zz}{}^R$ have the forms given in Eq.

(3.2), and all terms are understood to be evaluated at 2ω (omitted for brevity). The transmission coefficient for this field into medium 3, including all multiple reflections within medium 2, is given by: $t'_p = t_{23p}/\left(1 + r_{32p}r_{24p}e^{2i\beta}\right)$. Then, the SH field at the detector is:

$$E_p = E'_{2p} t'_p t_{31p} = \frac{4\pi i\omega \sec\theta_1}{c\sqrt{\varepsilon_1}}\left[\cos\theta_1 L^c_{xx} P^s_x + \sin\theta_1 L^c_{zz} P^s_z\right] \tag{3.9}$$

where the last equality comes again from Eq. (3.1) and defines the output local field factors $L_{xx}{}^c$ and $L_{zz}{}^c$. We may solve for these factors by substituting Eq. (3.8) into Eq. (3.9) and equating the coefficients of $P_x{}^s$ and $P_z{}^s$, to find that:

$$\begin{aligned} L^c_{xx} &= t'_p t_{31p} \sqrt{\frac{\varepsilon_1}{\varepsilon_2}} L^R_{xx} \\ L^c_{zz} &= t'_p t_{31p} \sqrt{\frac{\varepsilon_1}{\varepsilon_2}} \frac{\tan\theta_2}{\tan\theta_1} L^R_{zz} \end{aligned} \tag{3.10}$$

After some simplification, these expressions take exactly the same form as the input factors of Eq. (3.7), with indices and angles at ω replaced with 2ω values. Thus the output local field factors for the cell have the same correction as the input factors. The previously published output factors did not have this correction, but were claimed to be the same as the uncorrected input factors. It is not clear at what point our derivation may have differed from the earlier one, which was not explicitly shown.

For nematic LC cells, the LC (medium 4) is uniaxial. Pure *s* and *p* waves can then propagate through the LC only for special values of the sample rotation angle Φ. In general, the LC instead has extraordinary and ordinary (e and o) modes whose polarization vectors vary with Φ. We write the input local field factors in terms of the transmission coefficients published by Lekner (68) for an isotropic layer on a uniaxial substrate. In applying these equations, Lekner's medium 1 becomes our medium 3, the isotropic layer becomes medium 2, and (α, β, γ) become $(\cos\Phi, \sin\Phi, 0)$. The input factors are:

$$
\begin{aligned}
L^u_{xx}(\omega) &= (t_{pe}X_e + t_{po}X_o)\frac{t_{13p}}{\cos\theta_1} \\
L^u_{yy}(\omega) &= (t_{se}Y_e + t_{so}Y_o)t_{13s} \\
L^u_{zz}(\omega) &= -(t_{pe}Z_e + t_{po}Z_o)\frac{t_{13p}}{\sin\theta_1}\frac{n_o^2}{n_m^2} \\
L^u_{xy}(\omega) &= (t_{se}X_e + t_{so}X_o)t_{13s} \\
L^u_{yx}(\omega) &= (t_{pe}Y_e + t_{po}Y_o)\frac{t_{13p}}{\cos\theta_1} \\
L^u_{zy}(\omega) &= (t_{se}Z_e + t_{so}Z_o)t_{13s}\frac{n_o^2}{n_m^2}
\end{aligned}
\qquad (3.11)
$$

where (X_o,Y_o,Z_o) and (X_e,Y_e,Z_e) are the o and e polarization unit vectors (Lekner Eq. (7) and (8)), and $t_{po},t_{pe},t_{so},t_{se}$ are transmission coefficients from medium 3 to medium 4, given by Lekner in Eq. (68) and (70). n_o is the ordinary refractive index of the LC. The local field matrix has only six independent elements, because the X and Z components of the incident field are related; the three matrix elements which are not shown were set to zero.

To find the output local field factors for this case, we calculated the *s* and *p* fields radiated into medium 1 by a polarization sheet at the SH source layer, using the boundary conditions of Lekner Eq. (11) and (13) together with Shen (12) Eq. (3). The local field factors were then calculated from Eq. (3.1). The three elements set to zero in the output matrix were the same as the zero elements of the input matrix transposed. Numerically it was shown that the output matrix equals the transpose of the input matrix, with the sign of $L^u_{zy}(\omega)$ changed, for a variety of arbitrary choices of angles, layer thicknesses and refractive indices (including complex values). But this relationship was not demonstrated algebraically due to the complexity of the equations involved.

The non-diagonal input and output local field factors mean that *s* and *p* fields can mix: a *p*-polarized incident field can give a partially *s*-polarized source field, for example, or a SH polarization in the *s* direction can generate a *p*-polarized output field. The effect of the off-diagonal terms on the fits of Chapter 2 was found to be small.

3.3 SHG NULLING TECHNIQUE FOR ISOTROPIC INTERFACES

A goal of many SHG studies is to measure the second-order nonlinear susceptibility $\chi^{(2)}$ of interfaces which are isotropic about the surface normal (having $C_{\infty v}$ symmetry). Such an interface has three independent, complex components of the susceptibility tensor: $\chi^{(2)}_{zzz}, \chi^{(2)}_{zii}$, and $\chi^{(2)}_{izi}$, where $i = x$ or y. These components may be deduced from measurements of the SH signal for various input and output polarizations. Here is presented a method of extracting the susceptibility from SH nulling measurements, which allows calculation of the full susceptibility up to an overall phase factor, without the use a reference signal for phase calibration. This method allows simple testing of various assumptions which have been previously been used in similar calculations.

The nonlinear susceptibilites of interfaces have often been calculated using only a portion of the measurable signal, together with assumptions which simplify the calculation. A common example is the following. Consider a monolayer of achiral, polar-ordered molecules at an interface, isotropically distributed about the surface normal, such as a Langmuir monolayer of 8CB on water. The SHG signal is assumed to come entirely from these molecules, which have a molecular nonlinear polarizability $\alpha^{(2)}$ with a single nonzero component, $\alpha^{(2)}{}_{\xi\xi\xi}$ (see Eq. (2.3)). Then , the surface susceptibility becomes real and the number of independent real unknowns drops from six to two (compare Eq. (2.4)):

$$\chi^{(2)}_{zzz} = N_s\langle\cos^3\theta\rangle\alpha^{(2)}_{\xi\xi\xi} \tag{3.12}$$

$$\chi^{(2)}_{zii} = \chi^{(2)}_{izi} = N_s\langle\sin^2\theta\cos\theta\rangle\alpha^{(2)}_{\xi\xi\xi}$$

The measured signal magnitudes for polarizations of p-in, p-out and s-in, p-out are then used to calculate these two components and give the average tilt angle θ.

It is possible to make a more complete measurement of the interface SH response, and use that data to reduce the number of assumptions in finding $\chi^{(2)}$. For instance, some studies have made magnitude measurements for more different polarizations (66). A very complete characterization of the susceptibility may be made by directly measuring the signal phases in addition to the magnitudes, using a phase reference (69) (Chapter 2 illustrates such phase measurements). However, direct phase measurements require substantial additional equipment and time. Recently the magnitudes and relative phases of all susceptibility components have been calculated from signal magnitude measurements only, by varying the input polarization with a rotating quarter-wave plate (63-65). The signal magnitude vs. quarter-wave plate rotation angle was recorded for several linear output polarizations, and these plots were Fourier analyzed to find the susceptibility.

The nulling method described here also allows calculation of $\chi^{(2)}$ (up to an overall phase factor) from signal magnitude measurements. The data analysis is simpler than in the rotating wave plate method described above. The susceptibility is overdetermined from the data, allowing consistency checks for accuracy. This method is especially well-suited for testing different models of local-field or Fresnel factors (59) (see also Appendix A), since these factors are only introduced in the final step of the analysis. The essence of the method is simple: rather than measuring only the magnitude of the SH signal, its full elliptical polarization state is measured, for several linear input polarizations.

The elliptical polarization state of the SH beam, for a given linear input polarization γ_1, is measured by nulling the signal with a quarter-wave plate and polarizer, as illustrated in Sections 3.4 and 3.5. Two angles are measured which characterize the ellipse. First is ψ, the angle between the plane of incidence and the ellipse minor axis. The second is ζ, which is related to the eccentricity (eccentricity = $|\tan \psi - \zeta|$), and which gives the handedness of the ellipse: $\psi - \zeta$ is positive for a right-handed elliptical polarization and negative for left-handed. These two angles are used to calculate the magnitude ratio and phase difference of the p and s components of the field: $|E_p(2\omega)|/|E_s(2\omega)|$ and $\varphi_p - \varphi_s$ (as described for example in (70)).

Next, equations are needed which relate the fields to the susceptibility $\chi^{(2)}$. For arbitrary input polarization γ_1 (0° for p, 90° for s), the input polarization vector is:

$$\hat{\mathbf{e}}_{\gamma 1}(\omega) = \left[-\cos\theta_1(\omega)\cos\gamma_1, \sin\gamma_1, \sin\theta_1(\omega)\cos\gamma_1\right] \tag{3.13}$$

and the *p* and *s* polarized SH fields are written:

$$\begin{aligned} E_p(2\omega) = K\Big[&c_1\chi^{(2)}_{zzz}\cos^2\gamma_1 + \chi^{(2)}_{zii}\left(c_2\cos^2\gamma_1 + c_4\sin^2\gamma_1\right) \\ &+c_3\chi^{(2)}_{izi}\cos^2\gamma_1\Big] \\ E_s(2\omega) = K&c_5\chi^{(2)}_{izi}\sin\gamma_1\cos\gamma_1 \end{aligned} \tag{3.14}$$

where *K* is the ratio in Eq. (3.1), and the c_i are complex constants containing the local field factors (they may be found from Eq. (2.2)). Using these equations, the susceptibility components may be simply expressed in terms of the fields at special polarizations:

$$\begin{aligned} E_{45s}(2\omega) &= Kc_5\chi^{(2)}_{izi}/2 \\ E_{sp}(2\omega) &= Kc_4\chi^{(2)}_{zii} \\ E_{pp}(2\omega) &= K\left[c_1\chi^{(2)}_{zzz} + c_2\chi^{(2)}_{zii} + c_3\chi^{(2)}_{izi}\right] \end{aligned} \tag{3.15}$$

where E_{jk} is the field for *j*-in *k*-out polarization. The fields for arbitrary polarization are related to these special values by:

$$\begin{aligned} E_p(2\omega) &= E_{pp}(2\omega)\cos^2\gamma_1 + E_{sp}(2\omega)\sin^2\gamma_1 \\ E_s(2\omega) &= 2E_{45s}(2\omega)\sin\gamma_1\cos\gamma_1 \end{aligned} \tag{3.16}$$

The data processing then proceeds as follows. First , $E_{45s}(2\omega)$ is set to 1. Then, $E_s(2\omega)$ is real and is known for all γ_1 from Eq. (3.16). The *n* measurements of $|E_p(2\omega)|/|E_s(2\omega)|$ and $\varphi_p - \varphi_s$ are then used to calculate $E_p(2\omega)$. Note that the input polarizations used should not be *s* or *p*, since these give no *s*-polarized SH signal. For *n* calculated values of $E_p(2\omega)$, 2*n* real equations are then generated from Eq. (3.16):

$$\mathrm{Re}\left[E_p(2\omega)\right] = \mathrm{Re}\left[E_{pp}(2\omega)\right]\cos^2\gamma_1 + \mathrm{Re}\left[E_{sp}(2\omega)\right]\sin^2\gamma_1 \tag{3.17}$$
$$\mathrm{Im}\left[E_p(2\omega)\right] = \mathrm{Im}\left[E_{pp}(2\omega)\right]\cos^2\gamma_1 + \mathrm{Im}\left[E_{sp}(2\omega)\right]\sin^2\gamma_1$$

The n real equations and n imaginary equations may then be used independently to find the real and imaginary parts of $E_{pp}(2\omega)$ and $E_{sp}(2\omega)$. If n is two then these solutions may be directly calculated, while if n is larger than two then the solutions are overspecified and may be fit. Finally, the nonlinear susceptibility $\chi^{(2)}$ may be calculated directly from Eq.

(3.15). The overall magnitude of the solution may be calibrated by directly measuring $E_{pp}(2\omega)$, $E_{sp}(2\omega)$, or $E_{45s}(2\omega)$; measuring all three gives an independent consistency check. Only the overall phase of the susceptibility is not known.

This method of finding $\chi^{(2)}$ is very simple computationally, requiring only fits to linear equations with two unknowns (Eq. (3.17)). It also requires relatively few experimental measurements, and the nulling measurements are less sensitive than other measurements to errors such as laser power fluctuations. With more than two measurements, the solution is overspecified, allowing consistency checks. An important benefit of this method is that the local field factors are not used until after the fits, in the final calculation of the susceptibility with Eq.

(3.15). Thus it is easy to test different models of the local field factors; they could even be used as fitting parameters in this final step.

3.4 8CB MONOLAYER ON WATER STUDIED BY SHG NULLING TECHNIQUE

Measurements of the nonlinear susceptibility $\chi^{(2)}$ of a monolayer of 8CB at the air-water interface were used to calibrate other signal magnitudes and to demonstrate the measurement technique described in Section 3.3. 8CB monolayers have been well-studied previously (52, 57, 66), and make good test systems for several reasons: the SH response of 8CB is much larger than the water signal; 8CB may be well modeled as a sum of isotropically-distributed dipoles at the surface; 8CB forms insoluble monolayers on water, with a known and uniform surface density; and the pressure-area isotherm of 8CB on water is very reproducible and stable.

A custom-built PTFE Langmuir trough, with motorized PTFE barriers, was used in these experiments (Figure 3.1(a)). The surface pressure was measured by a Wilhelmy plate. The barriers were controlled, and surface pressure was monitored, by a Macintosh IIci computer using LabView II software (National Instruments, Austin, TX). A 1 mg/ml solution of 8CB in hexane was spread at the air-water interface and allowed to equilibrate for 10 minutes, and isotherms of surface pressure vs area per molecule were recorded while compressing or expanding the 8CB between the barriers.

The SHG setup was as described in Chapter 2, except that a quarter wave plate (for the SH wavelength, 266 nm) was added before the output polarizer. The procedure for nulling the SHG signal, giving the angles ψ and ζ described in Section 3.3, was as follows. Let γ_2 and γ_3 be the angles of the output polarizer and the quarter wave plate slow axis, respectively, related to the laboratory coordinates by (compare Eq. (3.13)):

$$\hat{\gamma}_i = \left[\cos\theta_1(\omega)\cos\gamma_i, \sin\gamma_i, \sin\theta_1(\omega)\cos\gamma_i\right] \tag{3.18}$$

where $i = 2$ or 3. First, γ_2 was varied to locate a minimum, with the quarter wave plate either removed or constrained to $\gamma_3 = \gamma_2$. The value of γ_2 which gives a minimum is the polarization ellipse minor axis ψ. Next, with $\gamma_3 = \psi$, giving linear polarization, the signal was again minimized by varying γ_2. The minimum angle is ζ. Any signal remaining at this minimum is from either background noise or an incoherent source.

Figure 3.1(b) shows the isotherm of 8CB on water. Slow leakage of 8CB around the barriers caused successive isotherms to be shifted to smaller areas, but isotherms were otherwise very reproducible, and are similar to those in the literature (57, 66). The plateau is a monolayer to trilayer transition (57). SHG data was taken on the close-packed monolayer at a surface pressure of 4 mN/m, below this plateau. Small barrier adjustments were needed periodically to maintain this pressure against leakage of 8CB.

The SHG signal from 8CB monolayers was nulled for input polarizations γ_1 of 0°, 15°, 30°, 45°, 65° and 90°. The signal nulling was complete, with any remaining background signal too small to measure reliably (<1% of peak signal). For 0° and 90°, which are s and p in, the SH signal was linearly polarized along p, as expected. For the other input polarizations, the SH polarization was near linear, but was slightly elliptical. An example of the nulling data for $\gamma_1 = 45°$ is shown in Figure 3.2(a). From this data the magnitudes and phases of the p-polarized signals for all γ_1 were calculated and fit as described in Section 3.3. The data and fit are shown in Figure 3.2(b). Uncertainties in real and imaginary parts of $E_p(2\omega)$ were found using estimated uncertainties of 0.5° in ψ and 1° in χ. The quality-of-fit parameter chi-squared per degree of freedom was 0.2 for the real fit and 0.6 for the imaginary fit, indicating that the data were self-consistent. The electric field fit parameters, calibrated as described below, are shown in Table 3.1.

The magnitudes of $E_{pp}(2\omega)$, $E_{sp}(2\omega)$ and $E_{45s}(2\omega)$ were measured experimentally, to test for consistency with the fits and for later use in calibration. The measured ratios of $E_{pp}(2\omega)$ and $E_{sp}(2\omega)$ to $E_{45s}(2\omega)$ were 0.39 ± 0.01 and 0.93 ± 0.01, respectively. From the fits, the values predicted for these ratios are 0.35 ± 0.01 and 0.92 ± 0.01, fairly consistent with the measured ratios.

From the fit results for the SH field, the second-order nonlinear susceptibility $\chi^{(2)}$ of the 8CB monolayer was calculated, assuming a monolayer dielectric constant of 1 (with the local field factors of Eq. (3.2)). The results are shown in Table 3.1. These results may be compared to the predictions of the simple electric dipole model of 8CB, under which the molecular nonlinear polarizability has a single component, $\alpha^{(2)}_{\xi\xi\xi}$. This model predicts that all components of $\chi^{(2)}$ have the same phase, and that $\chi^{(2)}_{zii} = \chi^{(2)}_{izi}$. The data are consistent with this model, to at least a first approximation. Using this model and assuming that all of the 8CB molecules have the same tilt angle θ at the interface, a value of 69° is found for θ, consistent with previous measurements (52, 57). The nonlinear susceptibility and the fields of Table 3.1 were calibrated using the published magnitude of $\alpha^{(2)}{}_{\xi\xi\xi}$ (52).

The nonlinear susceptibility differs from the predictions of the dipole model described above by a small but significant amount. One possible explanation is a local field effect due to dipole-dipole interactions; however, the usual equations for such an effect(59) do not predict a phase change, which is observed. Another possibility is that the dielectric constants of the monolayer are not equal to 1. In particular, it may be supposed that the dielectric constant at the SH frequency, $\varepsilon_m(2\omega)$, is complex, since 8CB is near resonance at this frequency. To test this possibility, the imaginary part of $\varepsilon_m(2\omega)$ was varied to minimize the phase differences between the elements of $\chi^{(2)}$. For a value of $\varepsilon_m(2\omega) = 1 - 0.2\,i$, the largest phase difference fell to 3°. The magnitudes of $\chi^{(2)}$ were unchanged by this variation, except that $\chi^{(2)}{}_{zii}$ increased by 2%, bringing it slightly closer to $\chi^{(2)}{}_{izi}$. This value of $\varepsilon_m(2\omega)$ gives a reasonable explanation of the data. However, the value of 1 used in the literature gives a good first-order fit to the 8CB monolayer data, and is used for calibration and elsewhere in this work. The 8CB monolayer makes a good system for testing models of local fields and Fresnel factors, in addition to providing a stable calibration of the SHG system.

3.5 ISOTROPIC 8CB FREE SURFACE STUDIED BY SHG NULLING TECHNIQUE

The free surface of 8CB illustrates the use of the SHG nulling technique when the phases of the nonlinear susceptibility components are substantially different from each other, and the advantages of obtaining phase information in addition to signal magnitudes. The magnitude of the SHG signal from this surface has been studied previously, and a model of the free surface was proposed using these measurements, with the assumption that all components of $\chi^{(2)}$ for the surface had the same phase (13). Measurements presented here give a more complete picture of the interface.

For these experiments, pure 8CB in a reservoir 1 mm deep was heated several degrees above its isotropic phase transition at 40.5 °C. The experiment was carried out as in Section 3.4, with the 8CB reservoir replacing the Langmuir trough. Also, as described in Chapter 2, a large excimer fluorescence signal was generated by the 8CB bulk, and was blocked with a mirror for the wavelength of 367 nm. Additional shielding of the monochromator entrance slit was needed for the free surface, to block scattered excimer light.

The SHG signal was nulled as described in Section 3.4, for input polarizations γ_1 of 15°, 30°, 45°, 60°, and 75°. A background signal, approximately 2% of the maximum signal, was found for each null, and is attributed to the bulk fluorescence. The estimated uncertainties in the data were 1° for ψ and 2° for χ. The fit to the electric field, shown in Figure 3.3, gives a chi-squared per degree of freedom of 1.7 for the real fit and 0.6 for the imaginary fit. The fit parameters, calibrated using the 8CB monolayer data, are shown in Table 3.1. The nonlinear susceptibility, also shown in this table, was calculated using previously measured dielectric constants for the bulk 8CB (50), and values of 1 for $\varepsilon_m(\omega, 2\omega)$. This is an effective surface susceptibility, containing both surface and bulk terms.

The 8CB free surface susceptibliity is not similar to a dipole monolayer susceptibility, since the phases differ substantially and the $\chi^{(2)}_{zii}$ and $\chi^{(2)}_{izi}$ terms differ. A previous model predicted that the 8CB free surface signal may contain both a surface dipole contribution and a bulk quadrupole contibution generated by antiparallel pairs of 8CB molecules; signal magnitudes suggested that only the bulk term actually contributed (13). However, if only the bulk term contributed then all susceptibilty components would be in phase, so the data in Table 3.1 show that this is incorrect. Fits to these data were attempted using the previous model with both surface dipole and bulk quadrupole terms, but the relative magnitudes and phases did not match. It may be possible to improve the fits by finding the correct monolayer dielectric constants, rechecking the dielectric constants of the bulk 8CB, or including other multipole expansion terms.

3.6 NONLINEAR OPTICAL PROPERTIES OF TRYPTOPHAN

The nonlinear optical properties of the aromatic amino acids are of interest as possible probes of protein orientation or other properties at interfaces. Tryptophan (Trp), tyrosine (Tyr) and phenylalanine (Phe) adsorbed to the air-water interface have previously been studied by SHG (67). The Trp signal was found to be an order of magnitude larger than the signal from the plain air-water interface, while the Tyr and Phe signals were twice as large as the water signal. The signal from Trp also appeared to be linearly polarized for an input polarization of 45°, compatible with a single-component molecular nonlinear polarizability $\alpha^{(2)}$, as found for 8CB.

These experiments on the aromatic amino acids were carried out on the same SHG setup used in this work. Later, in the course of this work, a problem with this setup was found. This problem does not affect the signal magnitudes found for the aromatic amino acids, but it does affect the finding of a linear signal polarization for Trp. The problem was that an aluminum mirror, used to steer the SH beam, had been placed between the sample and the output polarizer. The SH beam was reflected from this mirror with a large angle of incidence, introducing a phase shift between the *s* and *p* components. The phase shift could not be calculated exactly, due to coatings of unknown thickness on the mirror, but measurements with 8CB monolayers on water indicated that it was slightly larger than 90°. This did not affect measurements with the output polarizer set to *p* or *s*, but it affected data taken at other polarizations. The beam path was altered to remove the mirror between the sample and output polarizer, and all data presented in this work for output polarizations other than *p* or *s* were taken with this altered beam path.

The polarization of the SHG from Trp, for 45° input polarization, was checked here for comparison to previous data. The experimental setup is shown in Figure 3.1(a). Trp with a tert-butyloxycarbonyl-substituted amino terminus, or Boc-Trp (Calbiochem-Novabiochem, San Diego, CA) was dissolved at a concentration of 0.40 mM in 20 mM citric acid, pH 3.2, plus 0.5% EtOH. The trough was filled with this solution and equilibrated for 1 hour to allow the Boc-Trp to come to the surface. The surface pressure was 1 mN/m. Figure 3.4 shows the SHG data for Boc-Trp, and also for the plain air-water interface. The water signal is linearly polarized, but the polarization of the Boc-Trp signal is far from linear.

The SHG measurements in Figure 3.4 for Boc-Trp indicate that its surface nonlinear susceptibility contains components with very different phases, and thus that the single-component model of $\alpha^{(2)}$ does not apply to Trp. This also implies that the orientation of Trp molecules at the interface cannot be found in the simple manner used for 8CB (Section 3.4). The absolute signal magnitudes measured previously for Trp, for *p* and *s* output polarizations, are not affected by the changes presented here and should still be correct. Additional characterization of the SHG signal of Trp could be made by the method of Section 3.3, but is beyond the scope of this work. Tyr and Phe are also interesting candidates for further study by this method, since their structures have symmetries which make them likely to fit the single-component $\alpha^{(2)}$ model, although their SH signals are smaller than the signal of Trp.

Table 3.1: SHG fit results for 8CB monolayers and free surfaces.
Electric fields and second-order nonlinear susceptibilities, found by the fitting procedure of Section 3.3. All data are given in units of 10^{-17} esu, calibrated using the 8CB monolayer. The calibration introduces an additional uncertainty of roughly 10% in the absolute magnitudes, which is not shown in the table; the relative uncertainties from the fit are shown. The phase of $E_{45s}(2\omega)$ is set to zero.

	8CB monolayer	8CB free surface
$E_{pp}(2\omega)$	$(11.4 \pm 0.2) + i\,(8.8 \pm 0.5)$	$(-7.4 \pm 0.3) - i\,(4.2 \pm 0.3)$
$E_{sp}(2\omega)$	$(37.3 \pm 0.6) + i\,(6.2 \pm 1)$	$(3.6 \pm 0.1) - i\,(1.4 \pm 0.2)$
$E_{45s}(2\omega)$	41.3	7.13
$\chi^{(2)}_{zzz}$	$(36.4 \pm 1) \exp[i\,(14^\circ \pm 3^\circ)]$	$(3.0 \pm 0.6) \exp[i\,(-61^\circ \pm 10^\circ)]$
$\chi^{(2)}_{zii}$	$(107 \pm 2) \exp[i\,(9^\circ \pm 2^\circ)]$	$(15.7 \pm 0.6) \exp[i\,(-24^\circ \pm 3^\circ)]$
$\chi^{(2)}_{izi}$	119	$24.9 \exp[i\,(8.9^\circ)]$

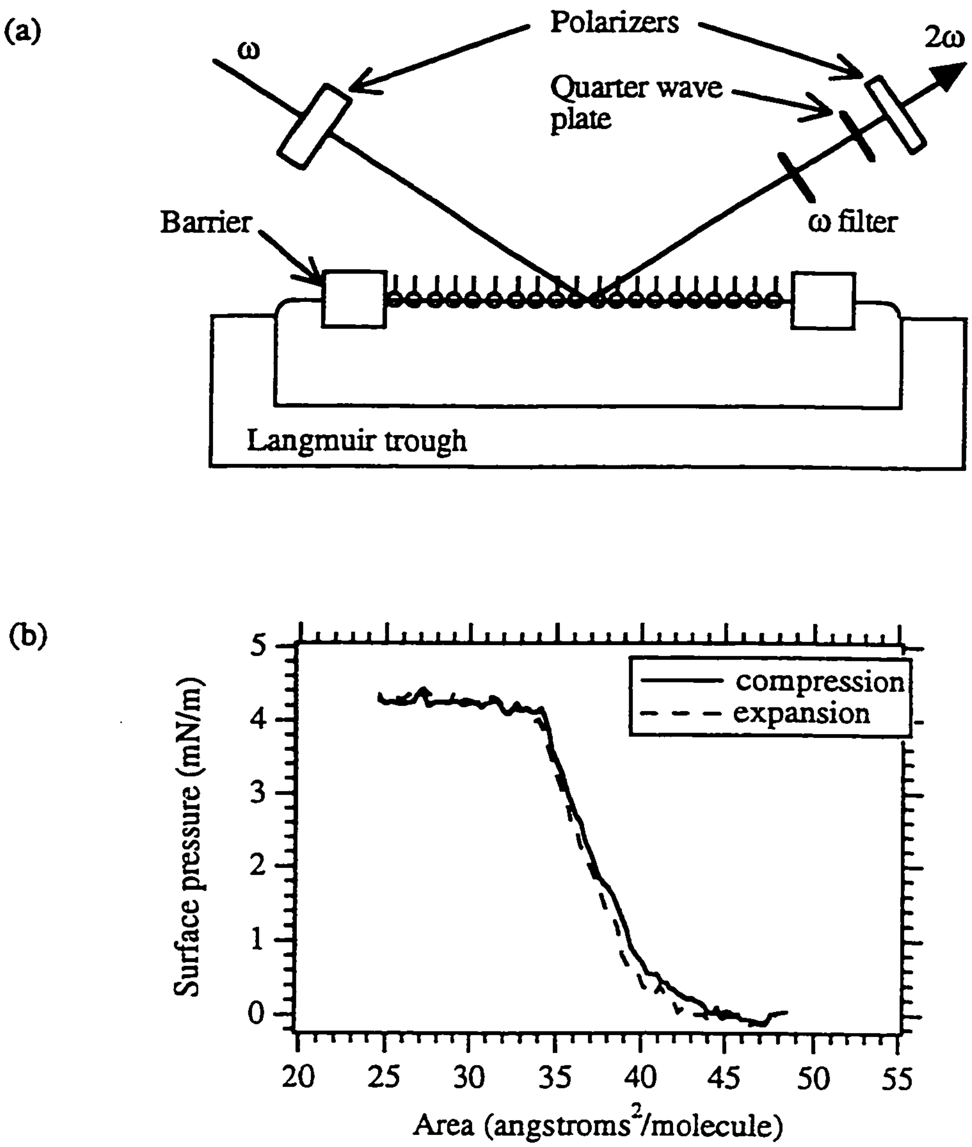

Figure 3.1: Experimental configuration for an 8CB monolayer on water.
(a) A monolayer of 8CB is spread at the air-water interface and compressed between the barriers. The laser is incident at a 60° angle. A quarter wave plate and polarizer are used to null the second harmonic signal. (b) Pressure-area isotherm of 8CB on water. The compression and expansion isotherms are solid and dashed lines, respectively.

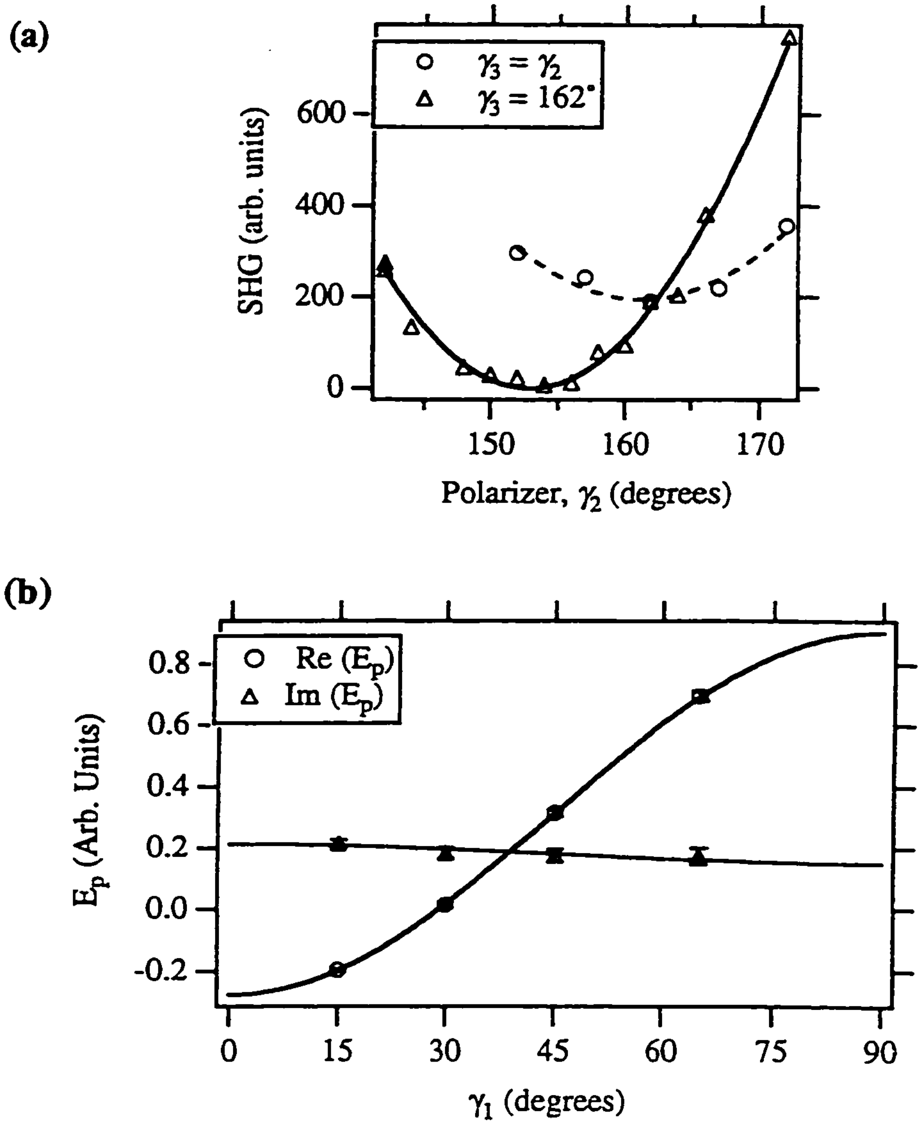

Figure 3.2: SH null data and fit for an 8CB monolayer on water.

(a) SHG vs. output polarization γ_2. The circles are data taken with the quarter wave plate angle γ_3 equal to γ_2, and the fit gives the minimum value ψ. Triangles are data taken with $\gamma_3 = \psi$, and fit to find ζ. The input polarization is 45°. (b) Real part (circles) and imaginary part (triangles) of $E_p(2\omega)$ vs input polarization γ_1, with fits to Eq. (3.17).

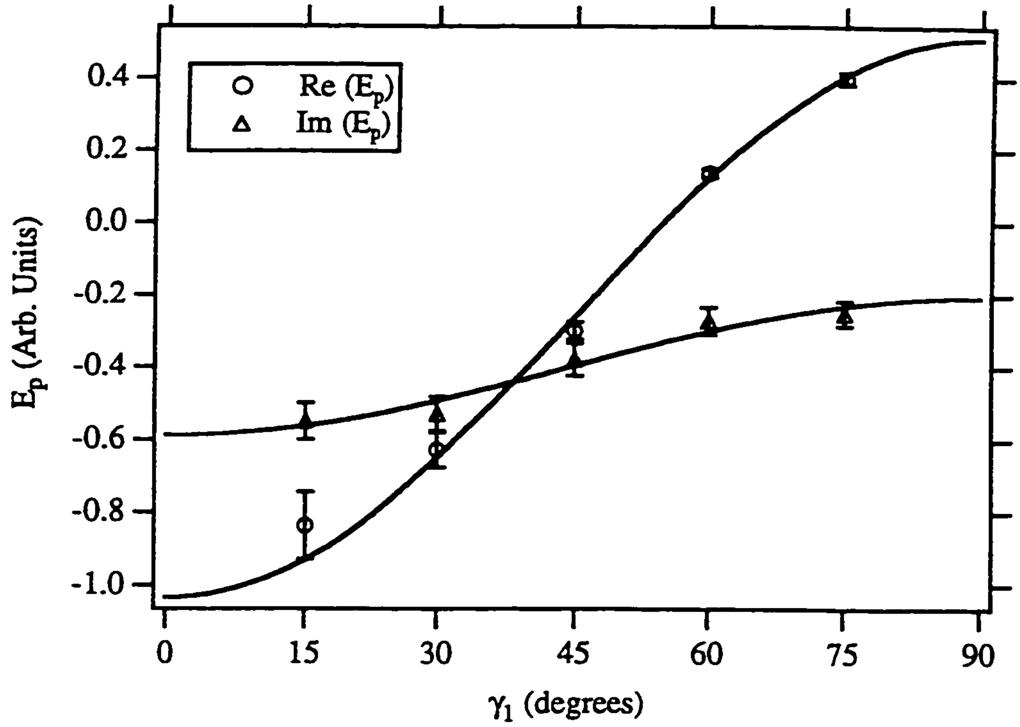

Figure 3.3: SH null data and fit for a free surface of isotropic 8CB.
The real and imaginary parts of $E_p(2\omega)$ (circles and triangles, respectively) are plotted vs input polarization γ_1, with fits to Eq. (3.17).

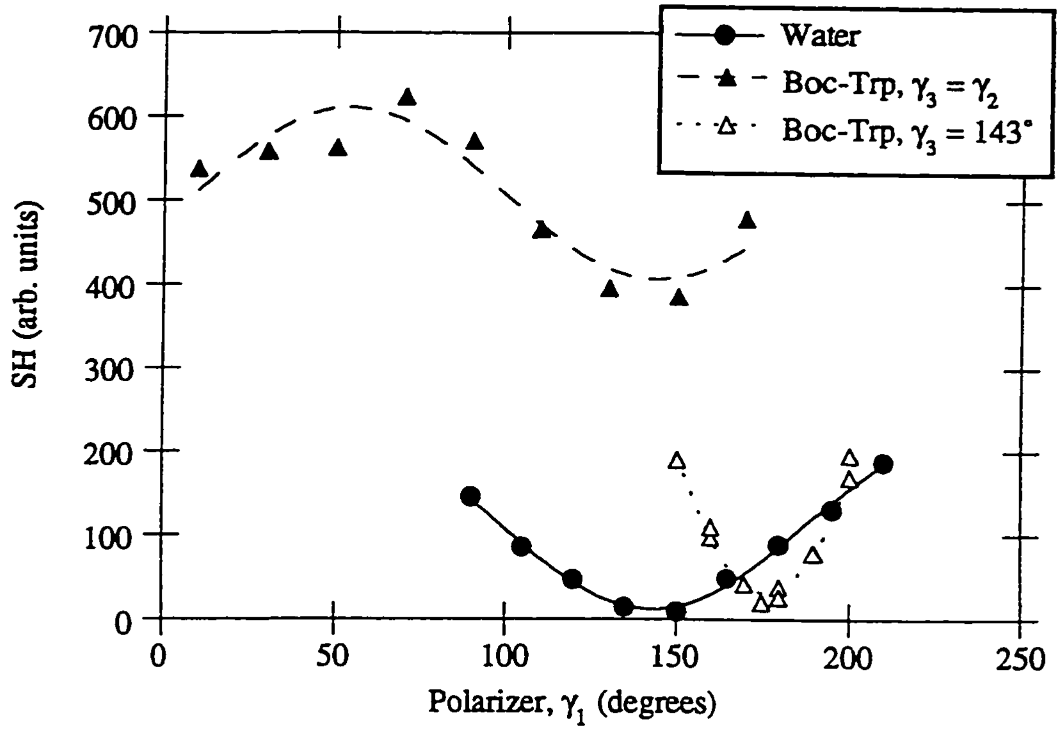

Figure 3.4: SHG signal from Boc-Trp at the air-solution interface.
Signals are plotted vs output polarization, γ_2, for an input polarization, γ_1, of 45°. Filled triangles are data for Boc-Trp with the quarter wave plate γ_3 equal to γ_2, and open triangles are with γ_3 set to 143°. The circles are data for the air-water interface with γ_3 equal to γ_2. Lines are fits to a $\sin^2$ function.

4. TESTS OF LIQUID CRYSTALLINE BIOPOLYMER ALIGNMENT ON SHEAR-DEPOSITED POLYTETRAFLUOROETHYLENE FILMS

4.1 INTRODUCTION

Surface alignment of liquid crystals is important technologically for the production of liquid crystal displays, and many types of surface preparations have been shown to align liquid crystals (LCs), including shear-deposited PTFE films (33, 34). However, the LCs aligned in this manner and used in displays are generally low molecular weight LCs. Polymer liquid crystals (PLCs), or liquid-crystalline polymers, are another important class of LCs with properties somewhat different from the low molecular weight LCs. The latter type are generally single-component systems which are thermotropic: they enter a liquid-crystalline state as they are cooled from the isotropic liquid phase, before becoming solid. PLCs are commonly dissolved in a solvent, and are lyotropic: they undergo a phase transition from disordered to ordered as their concentration in solution is increased.

Surface alignment of PLCs is of interest for the study of their elastic and viscous properties and response to external influences, and potentially for materials applications, where the liquid-crystalline state in processing can enhance material properties such as strength (e. g. Kevlar). The effects of anisotropic surfaces on polymer liquid crystals have not been widely reported, and alignment has often not been found in the systems studied (11). In one particularly well-studied PLC, poly-γ-benzyl-glutamate (PBG), tests with a number of common surface treatments failed to produce uniform homogeneous surface alignment (parallel to the preferred surface axis), and instead gave only homeotropic alignment (normal to the surface) (71). Uniform homogeneous alignment was achieved only by the use of magnetic fields in conjunction with plasma-deposited polyethylene films (24, 25). However, tobacco mosaic virus (TMV), a large rigid-rod system, showed uniform homogeneous alignment on obliquely-evaporated silicon monoxide films (72). For sickle-cell hemoglobin fibers, paper-rubbed quartz surfaces can induce alignment (73).

The category of PLCs also includes many biopolymers and biological systems (23): DNA (74, 75); viruses such as TMV; polysaccharides (76); and a number of proteins, including collagen (77), actin (78, 79), microtubules (80), and sickle-cell hemoglobin. Surface alignment in such systems, besides providing tests for general PLC alignment, is of interest for measuring material parameters by electric or magnetic field deformation of surface alignment, or for producing ordered samples to be studied by other techniques. In addition, ordered samples may be useful as models of situations in which liquid-crystalline order may influence in vivo properties, such as cytoplasmic viscosity (78) or order in structural fibers (81).

We have investigated the ordering of two PLCs on shear-deposited PTFE films. The first is PBG, which is a racemic mixture of L and D synthetic amino acid polymers, PBLG and PBDG. PBG consists of long semi-rigid alpha helices (Figure 4.1(a)), forming a nematic liquid crystal above a threshold concentration. PBG (and PBLG, which forms a cholesteric liquid crystal) have been extensively studied, and their phase behavior, elastic and viscous characteristics, and responses to external fields are fairly well-known (82-84). Since it is also relatively easy to work with, PBG made a simple representative system to test PLC alignment on PTFE films. The second system studied here is solutions of microtubules, which are cytoskeletal filaments polymerized from the protein tubulin. Microtubules are known to form liquid crystals (80, 85), but these phases have not been extensively studied. Microtubules were chosen because they are interesting, fairly complex biological elements which may still be reasonably modeled as rigid rods in a dilute solution. In addition, they may be polymerized and depolymerized by raising and lowering the temperature, respectively; thus, the phase transition may be easily induced in a sample which is in contact with anisotropic surfaces, without varying other parameters.

The following section summarizes some theoretical predictions for the onset of the nematic phase in lyotropic polymers, and for the elastic constants which play a large role in their response to anisotropic surfaces. Next, the experimental results for PBG and microtubules are presented. For PBG, the PTFE films produce uniform alignment parallel to the shear direction. The microtubules' threshold concentration for the liquid crystal phase agrees roughly with expectations, but no alignment is observed on the PTFE films. The final section discusses causes of these results.

4.2 THEORY

The simplest model of a PLC is a system of rigid rods in a solvent, interacting only by steric repulsion. Such models have generally been treated in one of two ways: a lattice treatment presented by Flory (86), or a virial expansion due to Onsager (87). The lattice model gives simpler results in some cases, and can more easily be applied to high polymer concentrations, but the Onsager approach is more accurate at low densities and has been used to estimate characteristics of PLC response to external forces; this approach is briefly summarized here. The free energy of the rods, in the second virial approximation, contains two terms which depend on the orientational distribution of the rods: an entropy-of-mixing term between rods of different orientations, favoring an isotropic distribution; and the second virial coefficient term representing the steric interactions of the rods, which is minimized for parallel order of the rods. This free energy was minimized by Onsager using a trial form for the rod distribution function, and has also been minimized numerically without an assumed trial distribution (88). The numerical result shows isotropic ordering of rods at low rod volume fractions v_2, and nematic ordering above a volume fraction $v_2^a = 4.191\ d/L$, where d and L are the rod diameter and length, respectively. Coexistence is found in the narrow range between $v_2^i = 3.290\ d/L$ and v_2^a. This result is exact for rigid rods in the limit of small v_2 and d/L. For long rods, the nematic transition occurs at low volume fraction; for example, if $L = 100\ d$ then $v_2^a = 0.004$.

This treatment of rigid rods can fail to describe real polymers for several reasons. One reason suggested already is that real polymer solutions may not have small values of v_2 and/or d/L, which then requires the use of higher virial coefficients. Another is that polymers typically have polydisperse lengths; including this effect within the Onsager treatment gives a wider region of phase coexistence between the isotropic and nematic phases (23). Flexibility of polymer chains also alters the phase diagram (88). Finally, the presence of external orienting influences such as flow or electromagnetic fields generally reduces the volume fraction at which orientation occurs (89).

Deformations or defects in LC alignment, and the response of LCs to external influences, are generally described in terms of an elastic theory first presented by Frank (90). Any deformation of the LC director from a single uniform direction is associated with an increase in the free energy, and it is found that this free energy may be written in terms of three elastic constants K_i:

$$F_d = \frac{1}{2}\left[K_1(\nabla \bullet \mathbf{n})^2 + K_2(n \bullet (\nabla \times \mathbf{n}))^2 + K_3(\mathbf{n} \times (\nabla \times \mathbf{n}))^2\right] \tag{4.1}$$

where **n** is the director. These three types of deformations, and the elastic constants associated with them, are called splay, twist, and bend, respectively. The effect of surface topography upon this free energy has been studied by Berreman (48). For the case of a surface with shallow ridges running in one direction, a LC with homogeneous anchoring (parallel to the substrate) and oriented across the ridges will have an extra deformation energy of:

$$\rho_\perp = \frac{1}{4}K_1(Aq)^2 q \tag{4.2}$$

relative to orientation along the ridges. Here A is the ridge amplitude and q the ridge wavenumber (2π/wavelength). This calculation was made assuming that K_1 and K_3 are equal. Using representative values of A = 10 nm and $q = 2\pi/(100$ nm) for a rubbed surface, and $K_1 = 10^{-11}$ N for the elastic constant of a low molecular weight LC, this energy evaluates to 6×10^{-5} J/m^2, larger than typical magnetic alignment energies for LCs and comparable to the effect of a large electric field (48). However, for PLCs the assumption of roughly equal elastic constants is not valid, so Eq. (4.2) would not give reliable estimates of alignment energies, and the theory only indicates that this energy should increase with increasing elastic constants.

The elastic constants for a system of rigid rods may be found by extension of the Onsager treatment, and have been tabulated numerically as a function of $Q = v_2(L/d)$ (91). It is found that K_1 is roughly three times as large as K_2, increasing with Q, while K_3 increases much more rapidly and becomes much larger than K_1 for large Q. For a given Q, the elastic constants are proportional to kT/d, so they become smaller as the rods are scaled up. For semiflexible polymers, the allowed bending of chains means that K_3 stops growing at large Q: for example, as the chain length L increases beyond the persistence length, K_3 stops rising and becomes smaller than K_1, as has been observed for PBG (82).

Table 4.1 shows values of elastic constants calculated from the rigid rod theory for microtubules and TMV, as well as experimental values for PBG and a typical low-molecular-weight LC.

The alignment energy of low molecular weight LCs, estimated by Eq. (4.2), is proportional to these elastic constants, but this equation assumes roughly equal elastic constants. Although this assumption is not satisfied by the PLCs in Table 4.1.; their alignment energies would be expected to increase with increasing elastic constants.

4.3 METHODS

PBG sample preparation. PBLG and PBDG (molecular weight 150,000 - 350,000, average molecular weight 230,000, degree of polymerization ~1050) were purchased from Sigma Chemical Company (St. Louis, MO). Equal amounts of PBLG and PBDG were dissolved in CH_2Cl_2, with 5% trifluoroacetic acid (CCl_3COOH, TFA) added to reduce the system viscosity and response time (71). All experiments were carried out at approximately 20% (by weight), giving a PBG volume fraction of about 0.20, above the nematic threshold. Cells were prepared between glass microscope slides with or without PTFE films (see Section 1.2), and with no spacers. The solvent tended to evaporate from these cells very quickly, so the cells were clamped to a stage as shown in Figure 4.1(b) and sealed by an O-ring made of the fluorocarbon Viton (Parker Seal Group, Lexington, KY), which has low solvent permeability. Pre-soaking the O-ring in solvent and adding some extra solvent to the reservoir further slowed the rate of drying, allowing samples to last for one to two days.

Alignment of PBG in magnetic fields was tested with a 1 T magnetic resonance imaging magnet in the laboratory of Prof. James Nelson at the University of Washington. The samples were left overnight in the magnet (the sample holder was made of aluminum and was sealed with brass screws for these experiments).

Microtubule sample preparation. Tubulin was isolated from bovine brain by cycling polymerization two and one-half times followed by phosphocellulose chromatography (92), and was stored in aliquots frozen at -80°C. Flow cells were prepared as shown in Figure 4.1(c): two parallel strips of vacuum grease (Dow Corning, Midland MI) were deposited about 1 cm apart on a microscope slide, shards of No. 1 cover glass were added to the grease as spacers (thickness ≈ 0.15 mm) and a coverslip was pressed on top. (The inert vacuum grease is not expected to interact with the flow cell contents; no difference has been noted between such flow cells and others constructed with stainless steel edges (93), although the others were also sealed with vacuum grease.) The flow cell dimensions were 18 mm by roughly 6 mm, giving a volume of about 10 µl. In some flow cells, one or both surfaces were coated with PTFE. Flow cells were filled from one end using a micropipette, with the flow direction parallel to the long axis, and the ends were sealed with immersion oil to prevent evaporation. Some PTFE flow cells were pre-treated with bovine serum albumin (BSA): before cell assembly, the slides and coverslips were immersed in a solution of 0.2 mg/ml BSA in water, then dried in air.

Tubulin was polymerized in a solution of 2 mM GTP, 100 mM $MgCl_2$ in BRB80 buffer (80 mM PIPES, 1 mM EGTA, 2 mM $MgCl_2$, pH 6.85 with KOH). To prevent GTP depletion, some solutions contained a GTP regeneration system consisting of 1 µg/ml acetate kinase and 20 mM acetyl phosphate (Boehringer Mannheim, Indianapolis, IN). Some solutions also contained 10 µM taxol, to stabilize microtubules against depolymerization. Polymerization was initiated by raising solution temperature from 0°C to 37°C. Polymerization was carried out either in a microcentrifuge tube (with the microtubules subsequently added to a flow cell), or in a flow cell, or in a squash, consisting of a microscope slide and coverslip with no spacers. For magnetic field experiments, microtubules were polymerized in an electromagnet at 0.35 T, within a temperature-controlled housing.

Microscopy. PBG samples were examined in reflection under an epi illumination microscope (Nikon Inc., Melville, NY), between crossed polarizers. For microtubules, a Diastar upright microscope (Reichert-Jung, Buffalo, NY) was used for polarized-light and DIC microscopy. The temperature of unstabilized microtubules was controlled during observation with a temperature-controlled blow dryer which heated a foam housing surrounding the sample, or with water circulated through metal coils cemented to the microscope objective lens. Birefringence was measured on a Leitz Laborlux 12 Pol microscope equipped with a Berek compensator.

4.4 RESULTS

PBG solutions were studied at a volume fraction of approximately 0.20, above the nematic threshold, and sample anisotropy was confirmed by polarized light microscopy. The typical nematic texture of an unaligned sample between bare glass slides is shown in Figure 4.2(a). The effect of magnetic fields upon the alignment of similar samples was tested. A sample left in a 1 T magnetic field overnight is shown in Figure 4.2(b) roughly one half hour after removal from the field. The domain size is larger in this sample, but defects are still present and the alignment direction varies from point to point, not following the magnetic field. The absence of alignment may be due to the time delay between removing the sample from the magnet and observing the sample. Samples removed from the magnet did not have static textures; rather, the defects and director orientation at a given spot shifted over a period of several hours, as shown in Figure 4.2(c), (d). The experimental configuration did not allow observation of the orientation of these samples while they were within the magnet.

However, nematic samples of PBG prepared between PTFE-coated slides showed uniform alignment parallel to the PTFE orientation direction, even without the use of magnetic fields. An example of this alignment for two different sample orientations is shown in Figure 4.3(a), (b). The sample texture is very smooth, with few defects or apparent features. Outside the PTFE film edges, the alignment direction gradually changed to random on the bare glass, without sharp defects. Thus, the film edges could not be imaged as clearly as with low molecular weight LCs (Figure 2.4), although they could be located approximately. Samples aligned on PTFE sometimes showed a less uniform texture, as seen in Figure 4.3(c), (d); the reason for differences in texture is not clear (see Section 4.5).

The LC threshold concentration of microtubules has previously been studied little, and was found to depend strongly on the conditions of polymerization. The approximate threshold tubulin concentrations at which birefringence was observed are summarized in Table 4.2. For solutions of unstabilized microtubules, birefringence was not observed at the highest concentrations used. The microtubules in these solutions continually polymerize and depolymerize, converting GTP to GDP in the process, and at high concentrations they quickly depleted the GTP available in solution. A GTP regeneration system allowed sufficient polymerization for the LC phase to appear. Alternatively, the addition of taxol stabilized the polymerized microtubules, preventing this problem. With the GTP regeneration system, microtubule samples could be repeatedly cycled between the birefringent and isotropic states by raising and lowering the temperature. For each type of solution, the threshold concentration was lowest when polymerized in a microcentrifuge tube and then injected into a flow cell, since the flow is an additional orienting factor, and the director was oriented parallel to the flow direction. Tubulin polymerized within flow cells had a lower threshold than tubulin polymerized in squashes without spacers, because a smaller proportion of the tubulin suffered loss of function at the surfaces. Although not included in the table, squashes with one PTFE surface did give an LC phase, at 7.5 mg/ml with taxol.

The magnitude of birefringence measured for liquid-crystalline samples of microtubules varied with the solution conditions, and also showed some variation between samples under apparently identical conditions. For samples of tubulin at 12.1 mg/ml, with the GTP regeneration system and without taxol, and polymerized in flow cells with glass surfaces, the magnitude of BR was $(1.8 \pm 0.9) \times 10^{-4}$ (mean ± standard deviation), for 13 samples. As in the case of PBG, samples differed in their apparent texture, with some appearing less smooth than others (Figure 4.4(a), (b)). In addition, samples at high tubulin concentrations which had the GTP regeneration system but were not taxol-stabilized often showed striped patterns of oscillating director orientation, as in Figure 4.4(c), or less regular director variations as seen in Figure 4.4(d) The average director orientation in striped samples is normal to the stripes.

To test the surface alignment of microtubules, tubulin was polymerized in flow cells with one PTFE-coated and one glass surface, as flow cells with both surfaces PTFE-coated were generally too hydrophobic to be filled with tubulin. These microtubules generally were not aligned parallel to the PTFE orientation axis. An example of the results for tubulin at 7.5 mg/ml, in the presence of taxol (and also with a GTP regeneration system), is shown in Figure 4.5. The PTFE axis was perpendicular to the long axis of the cell, which was also the flow axis when the flow cell was filled, and the microtubules are oriented along the flow cell's long axis. DIC microscopy of a flow cell surface shows the PTFE ridges, and also shows variations in microtubule orientation direction, by variations in the directions of fine striations as well as changes in brightness (Figure 4.5(b)). The microtubule orientation does not follow the PTFE ridges, but instead appears random. Over a number of similar experiments, the microtubules were most often found to be either oriented in random, varying directions or oriented parallel to the flow cell's long axis, whether the PTFE was oriented parallel or perpendicular to this axis. To remove cell asymmetry and flow effects, microtubules were polymerized in a squash with one PTFE surface, but their orientation as seen in Figure 4.5(c) was again random.

Microtubule orientation on PTFE films was also tested with the GTP regeneration system and no taxol, at a tubulin concentration of 12.1 mg/ml. This would remove any possible flow alignment arising from taxol-induced pre-polymerization of the cold tubulin. The microtubule alignment again did not follow the PTFE, but either appeared random or showed a slight preference for orientation parallel to the flow cell's long axis. Many of the flow cells filled with this tubulin solution had the stripes shown in Figure 4.4(c). The stripes had a wavelength of 200 ± 40 μm (mean ± standard deviation).

Alignment of microtubules was tested on PTFE films pre-treated with BSA, which made the films less hydrophobic and allowed the use of flow cells with PTFE on both surfaces. These cells were filled with 12.1 mg/ml tubulin, with the GTP regeneration system and no taxol. The microtubules in these samples were predominantly oriented perpendicular to the PTFE, and parallel to the long axis of the flow cells.

The orientation of microtubules polymerized in glass flow cells within a 0.35 T magnetic field was also tested, again using 12.1 mg/ml tubulin with GTP regeneration and no taxol. The flow cell long axis was varied between parallel and perpendicular to the field during polymerization. The microtubules in these flow cells were not aligned parallel to the magnetic field more than 50% of the time, while their orientation was predominantly parallel to the long axis of the flow cell in approximately 70% of the 18 flow cells tested.

4.5 DISCUSSION

This section begins with a discussion of the LC threshold concentrations of microtubules and the magnitude of their birefringence (for PBG, threshold concentrations have previously been reported (23, 94)). It then focuses on possible explanations of the alignment results obtained for PBG and microtubules on PTFE films, along with implications for future experiments.

For microtubules, approximate anisotropic-phase thresholds under various preparation conditions are reported in Table 4.2. For theoretical comparisons, microtubules fit the requirements of the Onsager rigid rod model well. They have a diameter of 25 nm and are typically several microns long, giving a large value of *L/d*, and they have been used at quite small volume fractions. Their persistence length is 5.2 mm (95), much greater than *L*, so they may be considered rigid. Microtubules are negatively charged (96), but in the polymerization buffer have a Debye radius of only 0.6 nm, making electrostatic interactions small (88). The main complicating factor is that they are polydisperse, with a length distribution which depends on the particular conditions of polymerization.

Rigid-rod theory predicts that monodisperse microtubules 10 μm long would be found in the anisotropic phase above v_2^a = 0.010, or 6.4 mg/ml microtubules. Modeling the polydispersity with a population of two different lengths $L_1 = 2 L_2$, at equal concentrations, and average length 10 μm, shifts this concentration to 10.6 mg/ml (23). These values are roughly comparable to the observed threshold values in Table 4.2, with the differences probably due to variations in the length and polydispersity of microtubules and the amount of tubulin left unpolymerized (for unstabilized microtubules, approximately 2.5 mg/ml tubulin is unpolymerized, so the microtubule concentration in mg/ml is lower than the tubulin concentration by this amount). The measured birefringence for tubulin at 12.1 mg/ml agrees approximately with a previous result for tubulin oriented by flow (with slightly different solution conditions), which gave a birefringence of 2.0 x 10^{-4} at this concentration (97).

The theory of LC alignment by surface topographical features proposed by Berreman is quite general, depending only on the LC elastic constants, but few experimental tests of PLC alignment have been carried out. In this work, PBG on PTFE films showed uniform alignment parallel to the films' orientation axis. Previous tests had not found alignment of PBG on surfaces, but had generally observed homeotropic alignment (71). One study found that polyethylene films yielded PBG alignment parallel to the surface, perhaps due to reduced PBG endgroup interactions with the low-energy polyethylene surface (24). In the absence of end interactions, polymers are expected to align parallel to a surface because of entropic considerations (98). The low surface energy of the PTFE film may be important to parallel alignment of PBG, while the surface ridges may then constrain the alignment to a single direction. Since the PTFE surface interacts only weakly with many types of chemical groups, PTFE films make promising candidates for aligning a variety of other PLCs, if their elastic constants are similar and if alignment is not dominated by other influences (as discussed below for microtubules). PBG surface alignment may also be useful for aligning other, perhaps non-mesogenic, molecules, by including them as dopants in aligned PBG samples.

Alignment of microtubules by PTFE films was not observed, for any of the various sample configurations and solution conditions tested. The microtubules lay approximately parallel to the surface plane, but were not aligned along the PTFE orientation axis. The estimated elastic constants of microtubules are smaller than those of PBG or typical low molecular weight LCs (Table 4.1), indicating a lower energy for alignment. However, they are larger than the estimated elastic constants for TMV, which has previously been aligned by surfaces with a ridge topology (72). Microtubules and TMV are both rigid-rod systems with relatively large diameters (25 nm and 18 nm, respectively), which result in smaller elastic constants. One difference is that the microtubules studied have large axial ratios (L/d) and a low volume fraction, while TMV has a much smaller axial ratio and was studied at a larger volume fraction. These differences offset each other in the prediction of elastic constants, leading to similar results, but perhaps they affect the process of surface alignment. This could occur, for example, through differences in rotational viscosities, since the freedom of an individual polymer to rotate decreases strongly with increasing L (99). The polydispersity of microtubules is not taken into account in the calculation of elastic constants, but polydispersity does not appear to affect agreement between predicted and measured constants in PBG (82).

Variations seen in the apparent texture of microtubule and PBG birefringence are similar to some previous observations of texture variations (73, 80), although causes of variations between similarly-prepared samples are not clear. The striped patterns seen in unstabilized microtubule samples with a GTP regeneration system have been studied previously (100-102), and have been explained as energy-dissipative structures, of a type found in other reactions far from equilibrium (103). These patterns show that other factors besides the minimization of elastic constants are influencing microtubule orientation. This may explain the absence of surface alignment in striped samples, though not in taxol-stabilized microtubules or other cases where stripes were not present.

The orientation of these stripes has been studied for microtubule solutions in containers larger than flow cells, and was found to depend sensitively on weak external forces, including gravity (101, 102). The container walls were found to induce stripe orientation perpendicular to the walls (or average director orientation parallel to the walls), up to several millimeters away from the walls. The observation in this work of microtubule alignment parallel to the long axis of flow cells may be due to a similar wall effect, perhaps caused by the vacuum grease edges of the flow cell. The influence of such weak forces upon a flow cell several millimeters across suggests the absence of an aligning effect due to the PTFE films, which would be expected to be much stronger.

Polymerization of microtubules in magnetic field of 0.35 T was also unsuccessful at producing alignment. Previous to this study, one report had indicated that microtubules polymerized in a 1 T magnetic field were aligned (104). It was later found that a substantially higher field was needed, and a value of 17 T was used to produce alignment (105). One study of stripe formation in microtubules found that a large-scale stripe pattern was made clearer by a field of 9.2 T parallel to the stripes, but did not report any other field effects (102). Due to the apparently large fields needed to align microtubules, further magnetic field experiments were not pursued in this work.

Microtubules were chosen for this study as an apparent simple rigid rod system, in which even the effects of flow could be eliminated by polymerization in situ, so that the aligning effects of surfaces could be studied in isolation. However, their behavior is more complex than anticipated, as the spontaneous formation of stripe patterns indicates. The lack of surface alignment may be linked to the formation of these stripe patterns. The relatively low volume fraction and large length of microtubules may also affect the alignment, perhaps by increasing the rotational viscosity; further tests at much higher tubulin concentrations would be worthwhile, since higher nucleation rates would be expected to give larger numbers of shorter microtubules. Based on the results obtained for PBG, shear-deposited PTFE surfaces appear promising for aligning other simple PLC systems, although they do not appear to provide a general method for producing surface-aligned

PLCs, such as cloth-rubbed polymer surfaces provide for low molecular weight liquid crystals.

Table 4.1: Elastic constants of several liquid crystals.
The elastic constants K_1, K_2, and K_3 predict energies of splay, twist, and bend deformations, respectively. Values are estimated from hard-rod theory for microtubules (of 10 µm length and 10 mg/ml concentration) and for TMV ($v_2 = 0.2$). Experimental values are given for PBG ($v_2 = 0.2$, molecular weight 230,000) (82) and for 8CB, a low-molecular-weight LC (106, 107).

	K_1 (10^{-13} N)	K_2 (10^{-13} N)	K_3 (10^{-13} N)
Microtubules	2.7	0.9	50
TMV	1	0.4	4
PBG	200	6	180
8CB	20	15	20

Table 4.2: Approximate threshold tubulin concentrations for microtubule birefringence.
Concentrations are shown for microtubules polymerized either in a microcentrifuge tube (and subsequently injected into a flow cell), in glass flow cells, or in glass squashes with no spacers. The microtubules were either polymerized without any stabilizing factors, or with taxol, or with a GTP regeneration system.

	Unstabilized	Taxol	GTP regeneration
Tube	>9	2.5 to 5	5 to 7.5
Cell	>10	~7.5	7.5 to 10
Squash	-	>12.3	>12.1

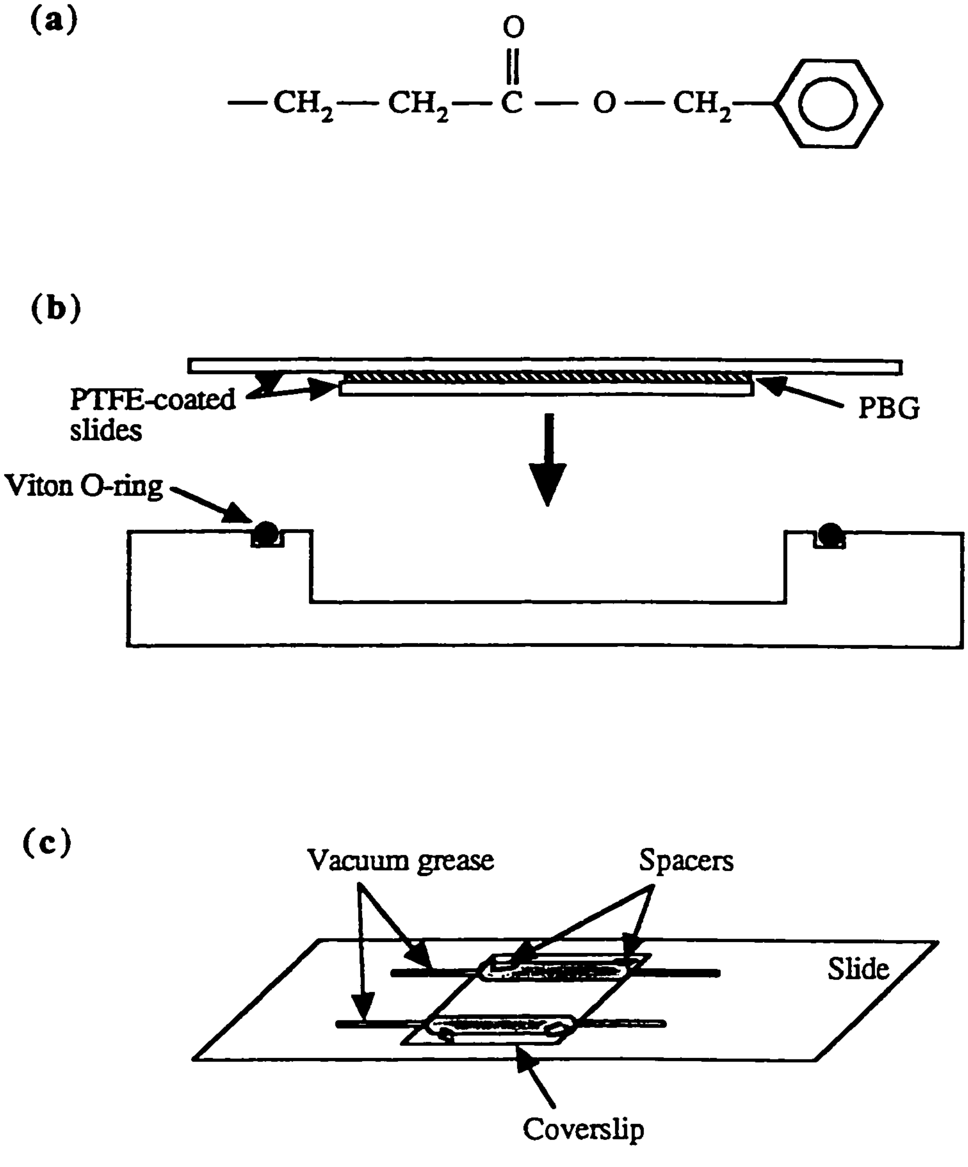

Figure 4.1: PBG and microtubule sample preparation.
(a) The side group of the synthetic amino acid PBG. (b) In the PBG sample holder, the larger (top) glass slide, is sealed to the base with a Viton O-ring, which is impermeable to the solvent used. (c) The flow cell consists of a microscope slide, two parallel strips of vacuum grease with No. 1 cover glass spacers, and a coverslip.

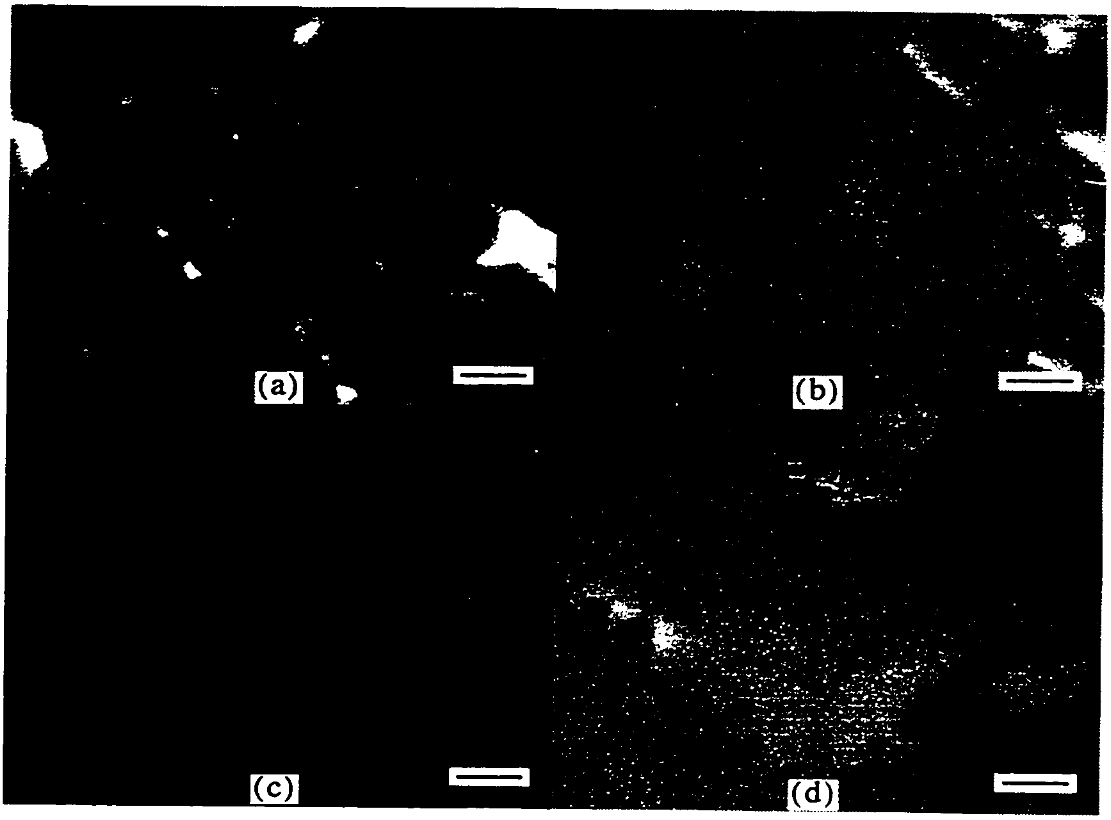

Figure 4.2: Unaligned PBG in glass cells.
Nematic-phase PBG samples at a volume fraction of 0.2 are sandwiched between glass slides and imaged by polarized light microscopy in reflection. (a) A typical unaligned sample. (b) A sample removed from a 1 T magnetic field roughly one half hour earlier, showing defects. (c) and (d) The same sample several hours later, with shifted domain boundaries, at two different sample rotation angles which differ by 30°. The scale bars are 30 μm.

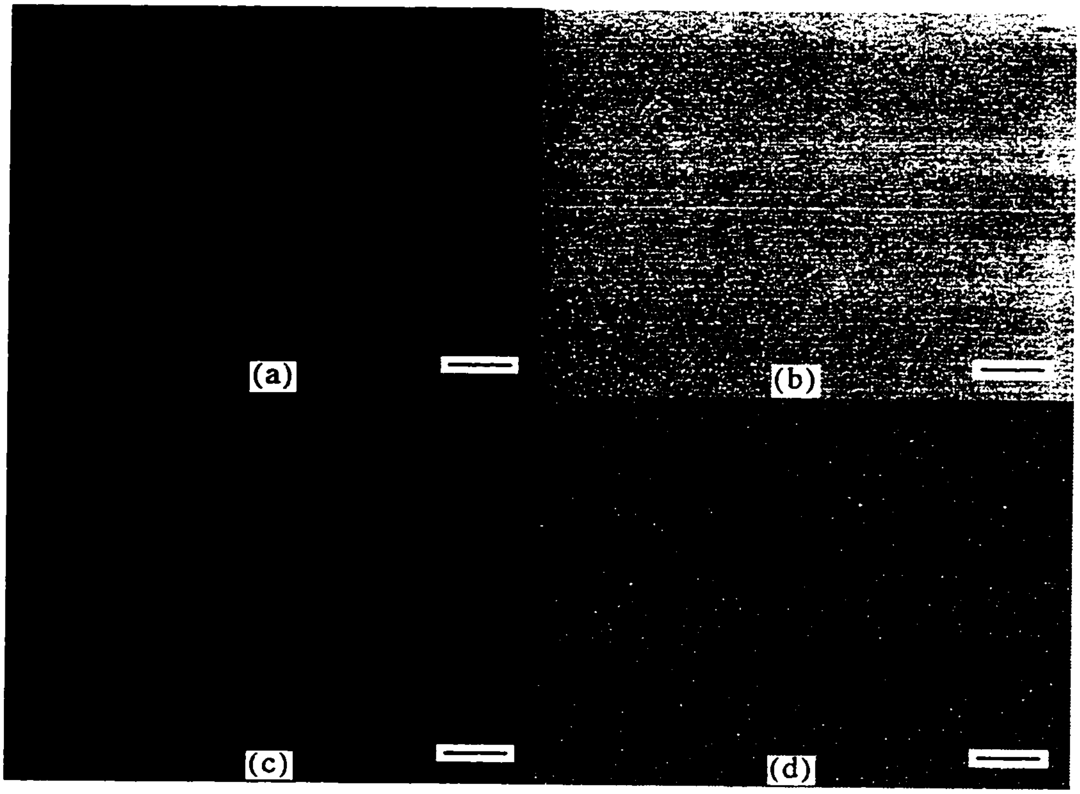

Figure 4.3: PBG aligned on shear-deposited PTFE films.
Nematic samples are imaged by polarized light microscopy. (a) and (b) PBG aligned parallel to the PTFE shear direction, at extinction and maximum brightness respectively. (c) and (d) Similar pictures for a sample with a less uniform texture. The scale bars are 30 μm.

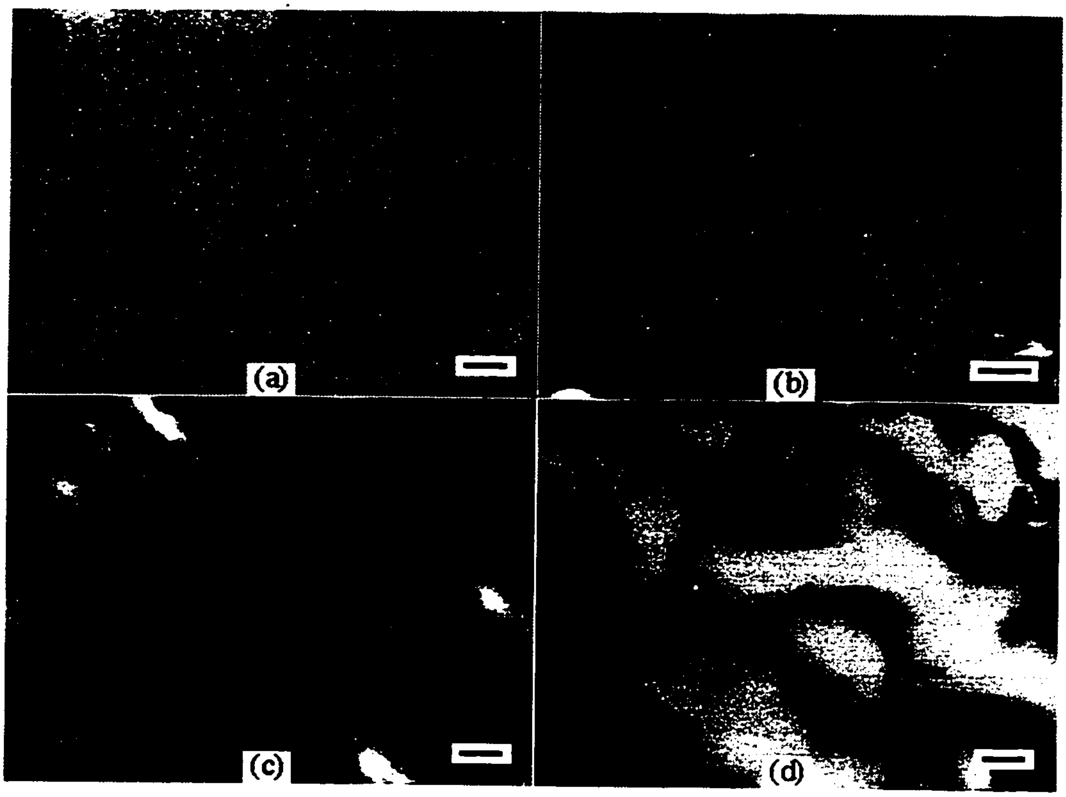

Figure 4.4: Images of microtubule birefringence.
Tubulin at 12.1 mg/ml, polymerized with a GTP regeneration system, and imaged by polarized light microscopy. (a), (b) Microtubules with uniform overall director orientations and slight differences in apparent texture. (c) Sample with a periodically varying director, producing light and dark stripes perpendicular to the average director orientation. (d) Sample with irregular changes in orientation. Scale bars are: (b) 200 μm; (a, c, d) 100 μm.

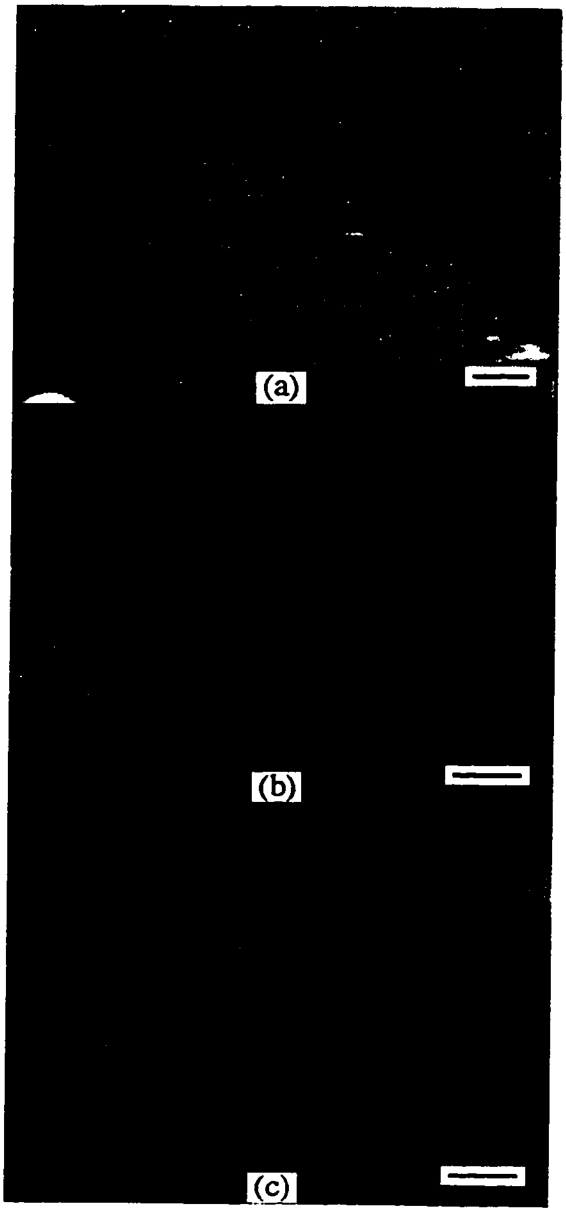

Figure 4.5: Microtubule alignment on PTFE films.
Tubulin was polymerized with taxol, at 7.5 mg/ml. (a) Polarized light image of microtubules on a PTFE-coated surface, oriented predominantly parallel to the flow cell axis (horizontal in the image) and perpendicular to the PTFE shear direction. (b) DIC image of a PTFE-coated flow cell surface, showing the oriented PTFE (vertical lines) and the varying alignment direction of adjacent microtubules. (c) Similar image for microtubules polymerized in a squash. The scale bars are: (a) 200 μm; (b,c) 10 μm.

5. MOLECULAR SHUTTLES: DIRECTED MOTION OF MICROTUBULES ALONG KINESIN TRACKS

5.1 INTRODUCTION

Nature has evolved intricate ways of controlling the active transport of molecules and large molecular complexes over long distances by the use of motor proteins. Many of these molecular motors have been isolated and characterized (108, 109), and much is being learned about how forces are generated on a molecular scale under the hydrolysis of adenosine triphosphate (ATP) (110-112). The intriguing properties of motor proteins have not previously been employed for transporting cargo over mesoscopic length scales in nonbiological environments. Potential applications of directed motion of molecular shuttles range from basic science to engineering, and include measurement of intramolecular forces in condensed matter, stretching and/or ordering of macromolecules in the direction of the shuttle's destination, and studies of kinetic processes where the rate limiting step is not determined by convection or diffusion, but by the transport capacity of individual molecular shuttles. Utilization of motor proteins for such applications is hampered by the fact that the molecules generate motion in random directions in standard motility assays. Little is known about how to properly design nanoscale surface textures that allow control over the direction of motion of individual motor proteins under in vitro conditions. Using the motor protein kinesin, we have investigated guidance of motion by a simple nanoscale architecture, and the mechanism of this guidance.

Kinesin is a motor protein which transports vesicles or other cargo along microtubules through the cytoplasm of cells (113, 114). Microtubules are cytoskeletal filaments polymerized from the protein tubulin, with ends designated plus (at which polymerization of tubulin occurs most rapidly) and minus. Kinesin is a double-headed protein. Each head is a motor domain that can bind to the surface of a microtubule and can bind to and hydrolyze ATP (115, 116). The tail is thought to bind to the cargo (117). Kinesin moves in one direction, from the minus to the plus end of a microtubules. Much about the molecular mechanisms of force generation has been deduced from in vitro motility assays in which kinesin molecules are immobilized randomly on glass surfaces. With a light microscope, fluorescently labeled microtubules are readily observed to move across these surfaces; they follow randomly-oriented paths in conventional assays, generally anchored to the surface by multiple kinesin molecules, although only a single one is needed to sustain motion (118). Similar motility assays are used with other motor proteins (119).

Here we report that a shear-deposited polymer film on a surface can induce microtubules to move preferentially along one axis. The films were prepared by a simple method of sliding a solid block of poly(tetrafluoroethylene) (PTFE) across a substrate, laying down a thin layer of PTFE on the substrate (7). The deposited PTFE molecules are stretched and oriented with their long axes along the shear direction, and the surface topology on a nanoscale shows uniaxially aligned surface ridges and grooves running in the same direction. The ridges have a random height distribution, typically on the order of 5 - 40 nm, and are spaced randomly, 10 nm - 1 µm apart (9, 37). Similar polymer films may also be used to orient the motion of motor proteins other than kinesin, as has been shown for actin filaments transported by the motor protein myosin (36, 120). Alignment and oriented crystal growth of a variety of substances on PTFE films have been demonstrated and studied (7-9, 121).

5.2 MATERIALS AND METHODS

PTFE and flow cell preparation. Microscope slides and coverslips were cleaned with Nochromix glass cleaner (Godax Laboratories, Takoma Park, MD), rinsed three times with 18 MΩ-cm water, soaked in 0.05 M NaOH, rinsed three times again, and dried in an oven. PTFE films were deposited onto coverslips on a hot plate at approximately 200 °C, by sliding a solid PTFE block across the surface with controlled pressure and speed, roughly 10^6 Pa and 0.5 mm/sec respectively. Each flow cell was prepared by laying down two parallel strips of vacuum grease (Dow Corning, Midland MI) about 1 cm apart on a microscope slide, then adding shards of #0 cover glass as spacers (thickness ≈ 0.1 mm) and pressing a coverslip on top. The final flow cell volume was roughly 10 µl. The ends of the flow cell were open, and the solution inside was exchanged by adding a new solution at one end with a pipette while wicking out the old solution at the other end with filter paper. The inner surface of the coverslip was coated with the PTFE film in our experiments, while the microscope slide remained uncoated.

Tubulin and Kinesin. Preparations of kinesin and rhodamine-labeled, taxol-stabilized microtubules have been described previously (122). Bovine brain tubulin was labeled with carboxytetramethylrhodamine, and a 1:3 mixture of labeled and unlabeled tubulin was polymerized into microtubules at 37 °C for 30 min. in a standard buffer, BRB80 (80 mM PIPES, 1 mM EGTA, 2 mM $MgCl_2$, pH 6.85 with KOH) plus 4 mM $MgCl_2$, 1 mM GTP and 5% DMSO. The microtubules were stabilized with 10 μM taxol, and diluted 1000-fold into a final BRB80 solution containing 0.2 mg/ml casein, 1 mM ATP, 10 μM taxol, and an oxygen-scavenging system (20 μg/ml glucose oxidase, 8 μg/ml catalase, 20 mM d-glucose, and 0.5% 2-mercaptoethanol) to minimize photobleaching. This solution was sheared twice through a 30g syringe needle to shorten the microtubules. Bovine brain kinesin was diluted to specified concentrations in BRB80 with 0.2 mg/ml casein and 1 mM ATP.

Motility Assay. Flow cells were first filled with a solution of the protein casein (Sigma Chemical Co., St. Louis, MO), which coats most of the accessible surfaces; this step is necessary to prevent the kinesin from losing function upon adsorption to bare glass, presumably by denaturation (118). Kinesin solutions were then added to the flow cells, and kinesin was allowed to adsorb for five minutes. This time is sufficient for essentially all of the kinesin to diffuse and adsorb to the flow cell surface, so that the average surface density is approximately proportional to the bulk kinesin concentration (122). After kinesin adsorption, the flow cells were filled with the solution of labeled microtubules. The motion of the microtubules was recorded using fluorescence microscopy, while the PTFE surfaces were imaged using differential interference contrast (DIC) microscopy. A Diastar upright microscope (Reichert-Jung, Buffalo, NY) was used for both fluorescence and DIC microscopy. Images were recorded onto videotape using a Sony AVC-D7 CCD camera, an Argus-10 image processor (Hamamatsu) and a S-VHS VCR (Mitsubishi).

Microtubule Motion Analysis. From videotapes of microtubule motility, microtubule directions and speeds were recorded on a personal computer using the Measure computer board (M. Walsh Electronics, San Dimas, CA). Each microtubule's path was recorded in five-second segments, to weight the directions of the independent microtubules by the time traveled. The number of segments per five seconds of video gave the average number of time-weighted microtubules for histograms. Microtubules which were stuck at one point were not included in the analysis, and those which attached, detached, or left the field of view were counted over as many segments as were accessible.

The number of independent microtubules moving in either direction along the striations was approximated by preparing histograms for the full range of angles from 0° to 360°, and fitting with the sum of a constant term and two Gaussians. The Gaussian peaks were fixed at 0° and 180°, parallel to the PTFE striations, and good fits were found in each case. The areas under the peaks were integrated and normalized using the total number of microtubules in each experiment. A histogram of microtubule landing orientations was fit with the sum of a Gaussian (with peak fixed at 0°) and a constant term, using the Leavenberg-Marquardt algorithm in the software package Igor Pro (WaveMetrix Inc., Lake Oswego, OR).

5.3 RESULTS

Figure 5.1 shows that shear-deposited PTFE films are able to direct the motion of microtubules. The grayscale background shows the grooves and ridges of the PTFE surface running along the film's shear direction, as seen by DIC microscopy. The microtubules in the same field of view were visualized by fluorescence microscopy. A time series of fluorescence images is superimposed on the DIC image to capture the motion of microtubules. The fluorescence images were taken at five-second intervals, and were assigned different colors to show the movement of the microtubules across the surface. In Figure 5.1(a), a clear preference for motion along the striations of the PTFE surface is seen. For this image, a moderate kinesin bulk concentration was used (3 μg/ml). This concentration would give approximately 250 motors/μm^2, if all motors adsorbed uniformly to the flow cell surfaces and were active, but the average number of bound microtubules suggests that fewer active motors are found on PTFE than on glass. Although the microtubules in this image were all moving in the same direction, further observations showed many microtubules moving parallel to the ridges in either direction.

Similar images for lower and higher kinesin surface densities are shown in Figure 5.1(b) and Figure 5.1(c), respectively. At the lower kinesin density (bulk concentration = 0.5

μg/ml), fewer microtubules were seen moving on the surface, and these microtubules appeared to have fewer attachment points: ends or sections of the microtubules often vibrated back and forth, showing that these portions of the microtubule were not attached to the surface (118). Greater numbers of microtubules moved on the surface at the higher kinesin density (bulk concentration = 18 μg/ml), and while a preference for motion along the surface striations is still observed, more microtubules are found moving in other directions.

Histograms of the microtubules' directions of motion are shown in Figure 5.2 for glass and PTFE surfaces at low, medium and high kinesin surface densities. At each density, the PTFE surface shows a strong preference for orientation along the direction of the striations (set to 0°), in contrast to the isotropic motion seen on glass. This preference for oriented motion is greatest at the medium kinesin density, and decreases somewhat at the high and low densities. Microtubules moving in either direction along a given axis (for instance, parallel or antiparallel to the 0° direction) are shown at the same angle on the histograms. The histograms show an increase in the total number of microtubules per unit time as the kinesin density increases, for each type of surface. At each kinesin density, the number of microtubules moving on PTFE is less than half of the number moving on glass.

The numbers of microtubules moving in either direction along the striations were estimated by making normalized fits to each direction separately. The result was that, for the three kinesin densities combined, the numbers of microtubules found moving in each direction were 82 ± 9 and 62 ± 8, compatible with equal probabilities for motion in either direction. The orientations of microtubules landing on the PTFE films were also tested, for medium kinesin density, with the results shown in Figure 5.3. With the small number of landing events recorded (due in part to a time lapse between sample preparation and observation), the peak at 0° is not highly significant, although some preference for orientation upon landing seems to be present. Fitting the data with a constant plus a Gaussian gave a peak height of 6 ± 2 and a standard deviation of 15° ± 7°, with a constant term of 1.6 ± 0.8. The very strong orientation shown in Figure 5.2(b) does not appear in Figure 5.3, indicating that much of the orientation observed on the surface develops through changes in the microtubules' directions of motion after they have landed.

In repeated experiments, the solution concentrations of kinesin which corresponded to each apparent surface density showed some variation, although the trends observed with changing kinesin concentration remained consistent. In one trial, for instance, no motility was seen at a solution concentration of 0.5 μg/ml, but increasing the concentration to 1.5 μg/ml gave motility similar to the low-density case described above. The low-density histograms of Figure 5.2(a) combine data taken at 0.5 and 1.5 μg/ml, while the other histograms in Figure 5.2 each use a single kinesin concentration. The speeds of the microtubules showed no consistent differences between PTFE and glass. The microtubule speeds measured on PTFE were 1.01 ± 0.11, 0.77 ± 0.13, and 0.86 ± 0.11 μm/sec, for low, medium and high densities respectively (mean ± standard deviation, counting 63, 81 and 69 microtubules). For glass, the speeds were 0.92 ± 0.11, 0.92 ± 0.14, and 0.78 ± 0.10 μm/sec, respectively (counting 20, 27 and 58 microtubules). Previous studies have shown that the speed of motion changes little with the number of motors which propel a microtubule, although it varies with other factors such as ATP concentration or a resisting force (for example, if the solution viscosity is increased) (123-125). Average speeds observed parallel to the PTFE ridges (± 10°) did not differ from speeds for other directions by more than the standard errors of the averages.

5.4 DISCUSSION

A number of explanations for the oriented microtubule motion on PTFE films may be suggested. The aligned PTFE film could cause a bias in the direction in which each individual kinesin motor propels a microtubule. However, this idea is unlikely given kinesin's apparent flexibility and ability to move a microtubule in any direction when bound to a surface (126). Also, with this idea it is difficult to explain why microtubules move in both directions along the PTFE striations, and why the degree of orientation decreases at high kinesin densities. Alternatively, some high surface ridges could prevent interactions between motors lying in the valleys and microtubules which were not parallel to the ridges, as illustrated in Figure 5.4(a). Or, functional kinesin could initially adsorb preferentially in linear "tracks" corresponding to ridges, grooves or other surface features, and separated by spaces with few active motors (Figure 5.4(b), (c)). For either of these mechanisms, microtubules moving across the ridges would have fewer attachment points and would be more likely to detach from the surface or change direction. Both mechanisms would predict that at high surface densities, more attachment points would be available to stabilize motion across the striations, and the preference for oriented motion would decrease, as observed.

The ridge mechanism requires some surface ridges to be high enough to limit microtubule interactions with bound kinesin. The surface ridges seen on the PTFE films by AFM were typically less than 30 nm high, although occasionally as high as 60-70 nm (36, 39), while the microtubule diameter is about 25 nm. Kinesin has a total length of about 75 nm, but it is not known how much of the rodlike kinesin molecule is bound to the PTFE surface, or how far above the surface the heads can reach. However, in motility assays on PTFE or glass, microtubules commonly cross over one another with no change in speed, indicating that a ridge at least 25 nm high does not significantly impede their motion. It then appears unlikely that the PTFE ridges would strongly inhibit interactions of kinesin with misaligned microtubules.

The track mechanism requires preferential adsorption of proteins to sites that are aligned with the films' shear direction. AFM images indicate that such alignment is found in at least two very different systems: myosin adsorbed on similar films (36), and crystals of the fluorophore 1,4-bis-2-(5-phenyloxazolyl)benzene grown on these films (9). The range of heights and spacings of the PTFE ridges and valleys suggests that their ability to generate long-range alignment is not limited to materials with a tightly-constrained dimension, but rather that various different materials may find suitable adsorption sites. Since the surface features vary little along the direction of shear, effective microscopic tracks of similar sites are produced. The existence of such tracks is the probable cause of oriented microtubule motion on PTFE films functionalized by kinesin. Preferential binding may occur either for kinesin, or for casein during pretreatment, or both.

The idea that preferential adsorption of kinesin into spatially confined tracks is the underlying mechanism that directs the motility of microtubules is quite promising for future applications. It implies that, in principle, any method that can produce narrowly defined tracks of kinesin should be appropriate to induce directed motility of microtubules. Such tracks could thus be generated in two or three dimensions by a multitude of techniques, for example, through nanomachining, nanopatterning or imprinting approaches, or by formation of mesoscale supramolecular assemblies that are functionalized with kinesin. These same approaches may also be applied to direct the motion of myosin, and possibly other motor proteins. Different motor proteins may have different requirements with respect to the minimum density of motors that is required on such tracks. A single kinesin molecule, for example, can move a microtubule several micrometers before detaching (118, 127), whereas myosin requires several motors for continuous movement (128, 129). The width of the track has to be optimized with respect to the average length and the bending stiffness of the filament; the stiffness of f-actin is 300 times less than that of microtubules (95).

Controlling active transport processes is of fundamental interest in the basic and applied sciences. Besides the well-developed methods of applying forces by external techniques, such as atomic force microscopy and optical tweezers, a complementary approach is possible using molecular motors, which requires that the spatial patterning and orientation of motion be controlled. This approach offers the possibility of transporting many small objects across a surface in parallel, rather than one at a time.

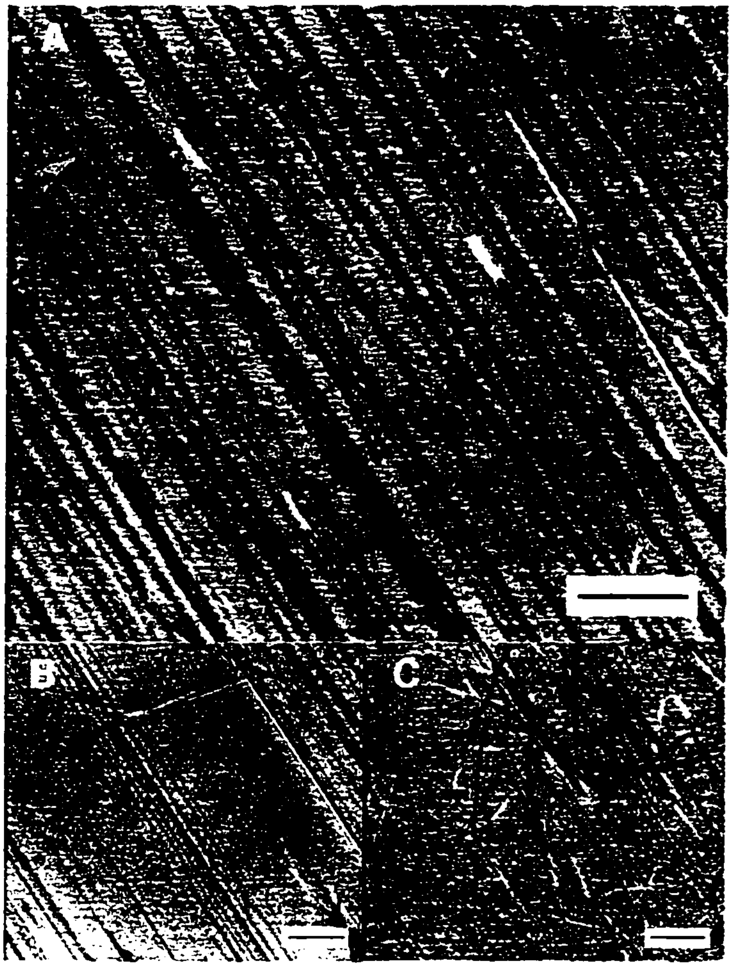

Figure 5.1: Motility of microtubules on uniaxially aligned PTFE substrates. Fluorescence images of microtubules taken at five-second intervals have been colored (advancing from red to violet) and superimposed on a DIC image of the underlying PTFE. The kinesin surface density was varied by changing the concentration of the solution from which kinesin was adsorbed; concentrations used were: (a) 3 μg/ml; (b) 0.5 μg/ml; (c) 18 μg/ml. Scale bars are 10 μm.

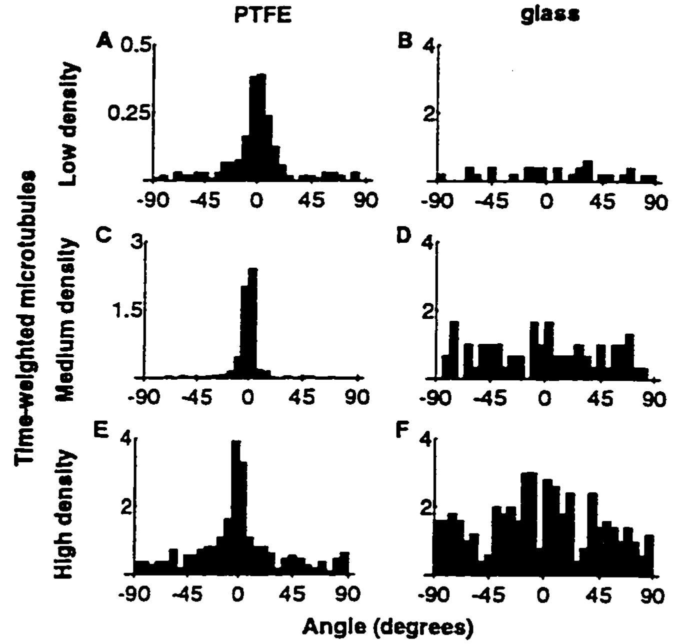

Figure 5.2: Histograms of the axis of microtubule motion.
The average number of time-weighted microtubules observed is plotted vs. the direction angle of the axis along which the microtubules moved. For experiments on PTFE surfaces (a through c), 0° corresponds to the PTFE orientation axis, while on glass (d through f), the absolute orientation is arbitrary. The kinesin solution concentrations were (a and d) 0.5 μg/ml or 1.5 μg/ml; (b and e) 3 μg/ml; (c and f) 18 μg/ml.

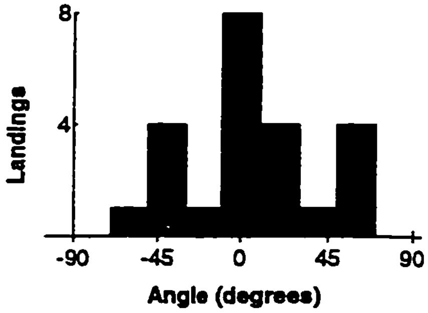

Figure 5.3: Histograms of microtubule orientation upon landing.
For medium kinesin density (bulk concentration = 3 μg/ml), the number of microtubule landings is plotted vs. the direction angle of microtubule orientation upon landing.

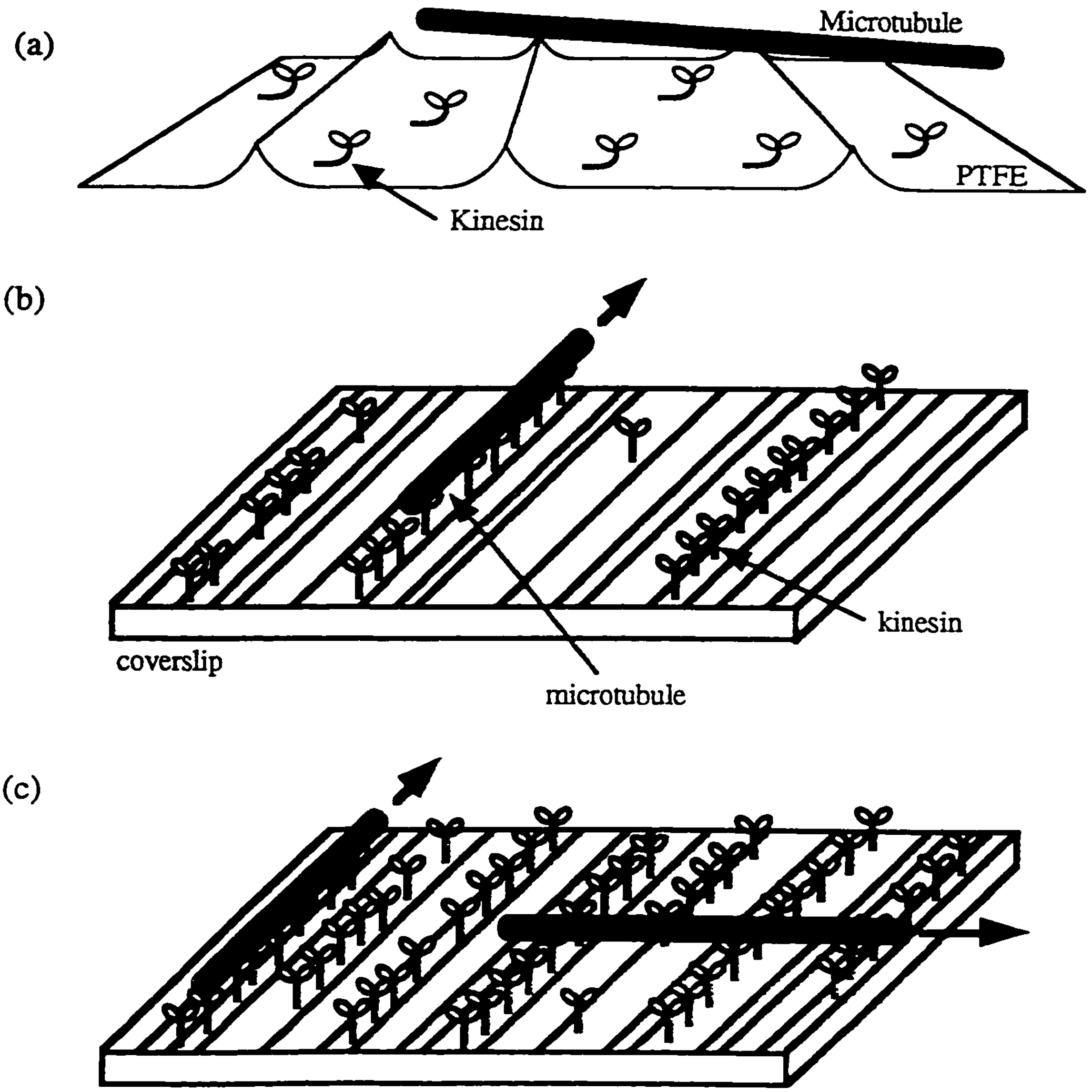

Figure 5.4: Ridge and track mechanisms for oriented microtubule motility. (a) Ridge mechanism: high ridges prevent unaligned microtubules from binding to many motors. (b) Track mechanism: tracks of active kinesin are separated by spaces, so that unaligned microtubules find few attachment points and are more likely to detach or swivel to follow a track. At high kinesin density (c), active motors fill in the spaces, and unaligned motion becomes more stable. Casein is left out of all pictures.

6. SUMMARY AND EXTENSIONS

Shear-deposited PTFE and HDPE films are highly structured surfaces which are known to produce alignment in a wide variety of different materials. In this work, optical second harmonic generation has been used to give a detailed molecular picture of liquid crystal alignment on these films, and the alignment of two polymer liquid crystals and a motor protein system on these films have been examined. The results of these studies are summarized below, after which some possible future extensions of this work are presented.

Liquid crystal alignment on PTFE and HDPE films was probed at the molecular level using SHG, with the well-characterized liquid crystal 8CB. The 8CB was found to show partial polar ordering at the polymer surfaces, but the azimuthal anchoring in the surface layer was weak, as shown by the reorientation of the surface molecules in the nematic-to-isotropic phase transition. There was no significant alignment of the surface layer of 8CB molecules in the absence of an ordered nematic bulk (that is, either for cells in the isotropic phase or for evaporated monolayers). This indicates that any epitaxy-like alignment induced by the surface was weak, and that alignment was caused primarily by surface ridges on the films, through an elastic interaction with the bulk liquid crystal.

Additional SHG results collected in Chapter 3 serve several purposes: facilitating the study of relatively complex buried interfaces, improving methods of data analysis for isotropic interfaces, and verifying the correct operation and absolute calibration of the experimental setup. The correct local field factors for liquid crystal cells were derived, and extended to account for the uniaxial nature of the liquid crystal; these factors are also applicable to various other buried interfaces. A simplified method was presented for using the phase information available in the second-harmonic signal to find the full nonlinear susceptibility of an isotropic interface, up to an overall phase factor. This method used with 8CB monolayers on water gave an absolute calibration of signal magnitudes, verified the simple dipole model of 8CB monolayers to a first approximation, and revealed a small correction to this model. The free surface of isotropic-phase 8CB, on the other hand, did not show a simple dipole SHG signal when analyzed by this method. Finally, it was shown that the molecular nonlinear polarizability of the amino acid tryptophan does not have a single dominant component, as a previous report had suggested (67).

The alignment of polymer and biopolymer liquid crystals on shear-deposited polymer films was studied in Chapter 4, and discussed in terms of the elastic deformation energy produced in the liquid crystals by surface ridges on the films. The films produced parallel homogeneous alignment in samples of the synthetic amino acid PBG, which had not previously been observed using other types of anisotropic surfaces. Comparisons with previous work suggest that the lack of strong specific interactions between the PBG molecules and the PTFE film is important in producing alignment, in addition to the effect of surface ridges. Liquid-crystalline samples of microtubules were also tested for alignment on these films, after being polymerized in contact with the films. However, the microtubules were not aligned. In the case of microtubules, the elastic deformation energy may be too weak to force alignment, particularly because microtubules have a higher rotational viscosity as a consequence of their greater length (compared to PBG). Alignment may also be hampered by director oscillations which form as energy-dissipative structures, in microtubule samples with a GTP regeneration system.

Chapter 5 describes the application of PTFE films to orient the motion of microtubules transported by the motor protein kinesin. Kinesin adsorbed to PTFE films was found to move microtubules primarily along the films' orientation axis, in contrast to the random directions of motion found on glass surfaces. As the surface density of kinesin was increased, the degree of microtubule orientation reached a maximum and then declined. This effect is attributed to preferential surface adsorption of kinesin into groups of sites which run parallel to the PTFE orientation direction, separated by spaces, forming "tracks" for microtubule motion along this direction.

The shear-deposited polymer films used in this work have the advantages of quite versatile aligning properties and simple preparation, but the shapes and sizes of the surface ridges and grooves cannot be controlled precisely or varied. For future work, the effect of particular sizes and shapes of topographical features may be studied, by taking advantage of recent developments in nanoscale surface patterning. Newer techniques such as microcontact printing (6) allow control of the height, width, spacing and other characteristics of ridges and grooves, and the fabrication of more intricate nanoscale surface features. The surface ridges and grooves of the polymer films were the primary aligning factor for 8CB, and also apparently for PBG, while the lack of strong interactions between the films and specific functional groups on the adjacent molecules may have allowed the ridge effects to dominate. It could also be that specific topographical features, such as steps or valleys of a certain dimension, produced the patterned protein adsorption which led to oriented microtubule motion.

Optical SHG has been a valuable tool in probing molecular order at interfaces, and additional areas of study are suggested by this work. The method of isotropic surface analysis presented in Chapter 3 is applicable to many studies of interfaces by SHG, and also by sum frequency generation (SFG), to gain additional phase information and consistency checking with a minimum of extra measurement time. This method may be used to more easily test different models of local field factors (59) and monolayer dielectric constants (see Appendix A), using simple adsorbates at interfaces. One useful application of this method would be in further characterization of tryptophan at the air-water interface, as suggested in Chapter 3. Two other aromatic amino acids, tyrosine and phenylalanine, have structures which suggest that they are likely to act as simple dipoles in SHG, similar to 8CB, although the magnitudes of their responses are much smaller than that of Trp (67).

The finding of uniform PBG alignment on PTFE films suggests further application of these films in the alignment of other PLCs. The results for PBG do not appear to depend on any specific interaction of PBG molecules with the polymer films, but rather on general interactions which may also work to align other PLCs. However, the results obtained with microtubules illustrate the fact that PLCs are not as easily aligned on surfaces as low molecular weight LCs, and that other factors besides surface effects may control alignment. PTFE films may be useful for testing the importance of elastic energy considerations in controlling the alignment of particular PLCs, as well as for measuring the elastic constants of aligned PLCs by the Fredericks transition (84, 130). An aligned PLC such as PBG may also serve as a matrix for alignment of other small molecules, which might not otherwise form anisotropic phases.

The patterning of kinesin on PTFE films, and the orientation of microtubule motility which results from it, show promise for applications in the field of nanotechnology. The naturally-occuring nanoscale motor kinesin may be formed into tracks for producing controlled motion of cargo attached to microtubules. Further development of these systems will require tracks which can be controlled much more precisely than the ones on shear-deposited PTFE. Again, microcontact printing is a good candidate for such surface patterning. Next steps could include curved tracks, branching tracks or intersections. Such elements could be combined to produce microtubule motion in one direction only: for example (Figure 6.1), a circular track with tangent rays radiating outward should retain microtubules which circle in one direction while sending those which move in the other direction out along the tangents.

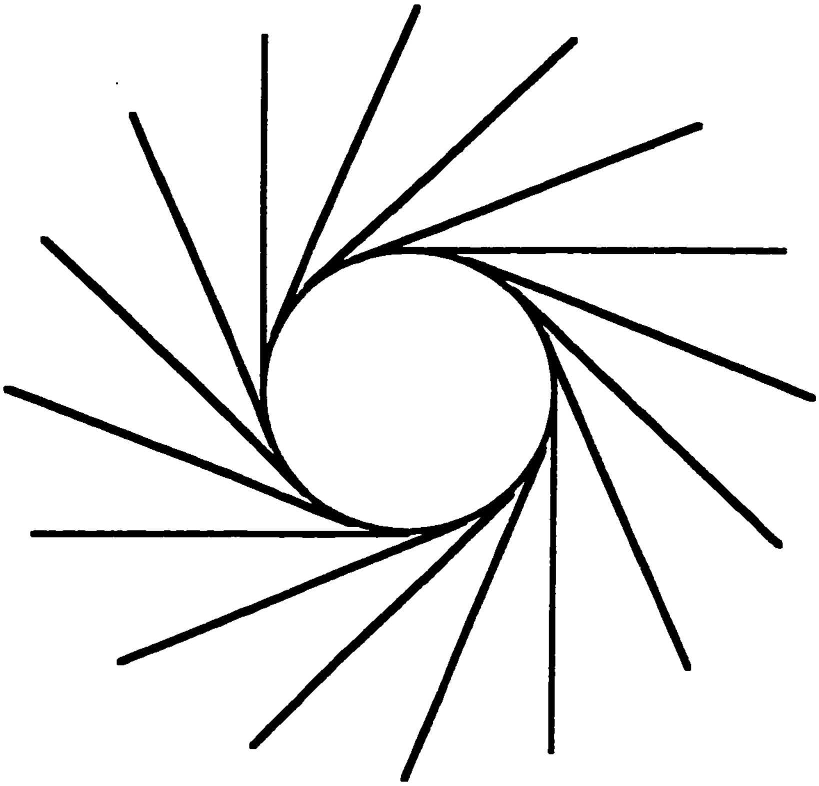

Figure 6.1: Kinesin track pattern for unidirectional microtubule motion. Microtubules traveling clockwise around the circle could branch outward along any of the tangent lines, making it likely that they would soon leave the circle. Those traveling counterclockwise would remain on the circle, and new ones arriving at the circle from the tangent lines would travel the same direction. Counterclockwise motion would be dominant on the circle.

BIBLIOGRAPHY

1. A. M. Belcher, X. H. Wu, R. J. Christensen, P. K. Hansma, G. D. Stucky, and D. E. Morse. Control of crystal phase switching and orientation by soluble mollusc-shell proteins. *Nature* **381**, 56 (1996).

2. I. Weissbuch, L. Addadi, M. Lahav, and L. Leiserowitz. Molecular recognition at crystal interfaces. *Science* **253**, 637 (1991).

3. G. Altankov, F. Grinnell, and T. Groth. Studies on the biocompatibility of materials: fibroblast reorganization of substratum-bound fibronectin on surfaces varying in wettability. *J. Biomed. Mater. Res.* **30**, 385 (1996).

4. E. T. den Braber, J. E. de Ruijter, L. A. Ginsel, A. F. von Recum, and J. A. Jansen. Quantitative analysis of fibroblast morphology on microgrooved surfaces with various groove and ridge dimensions. *Biomaterials* **17**, 2037 (1996).

5. B. Chehroudi, T. R. L. Gould, and D. M. Brunette. Titanium-coated micromachined grooves of different dimensions affect epithelial and connective-tissue cells differently *in vivo*. *J. Biomed. Mater. Res.* **24**, 1203 (1990).

6. Y. Xia, E. Kim, X. Zhao, J. A. Rogers, M. Prentiss, and G. M. Whitesides. Complex optical surfaces formed by replica molding against elastomeric masters. *Science* **273**, 347 (1996).

7. J. C. Wittman and P. Smith. Highly oriented thin films of poly(tetrafluoroethylene) as a substrate for oriented growth of materials. *Nature* **352**, 414 (1991).

8. C.-C. Chen, S. Riou, S. L. Hsu, and H. D. Stidham. Characterization of silk crystallization behavior on highly oriented substrates. *Langmuir* **12**, 1035 (1996).

9. D. Fenwick, P. Smith, and J. C. Wittmann. Epitaxial and graphoepitaxial growth of materials on highly orientated PTFE substrates. *J. Mater. Sci.* **31**, 128 (1996).

10. F. Motamedi, K. J. Ihn, D. Fenwick, J. C. Wittmann, and P. Smith. Polymer friction-transfer layers as orienting substrates. *J. Polym. Sci., Part B: Polym. Phys.* **32**, 453 (1994).

11. A. M. Donald and A. H. Windle. *Liquid Crystalline Polymers* (Cambridge University Press, Cambridge, 1992), pp 310.

12. Y. R. Shen. Optical second harmonic generation at interfaces. *Annu. Rev. Phys. Chem.* **40**, 327 (1989).

13. P. Guyot-Sionnest, H. Hsiung, and Y. R. Shen. Surface polar ordering in a liquid crystal observed by optical second harmonic generation. *Phys. Rev. Lett.* **57**, 2963 (1986).

14. T. F. Heinz, C. K. Chen, D. Richard, and Y. R. Shen. Spectroscopy of molecular monolayers by resonant second-harmonic generation. *Phys. Rev. Lett.* **48**, 478 (1982).

15. C. S. Mullin, P. Guyot-Sionnest, and Y. R. Shen. Properties of liquid-crystal monolayers on silane surfaces. *Phys. Rev. A* **39**, 3745 (1989).

16. T. F. Heinz, H. W. K. Tom, and Y. R. Shen. Determination of molecular orientation of monolayer adsorbates by optical second-harmonic generation. *Phys. Rev. A* **28**, 1883 (1983).

17. M. Buck, O. Dannenberger, and J. J. Wolf. Formation of organic thin films at the liquid/solid interface studied by second harmonic spectroscopy. *Thin Solid Films* **284**, 396 (1996).

18. X. Zhao, S. Ong, and K. B. Eisenthal. Polarization of water molecules at a charged interface. Second harmonic studies of charged monolayers at the air/water interface. *Chem. Phys. Lett.* **202**, 513 (1993).

19. V. Vogel. What do nonlinear optical techniques have to offer the biosciences? *Curr. Opin. Colloid & Interface Sci.* **1**, 257 (1996).

20. B. L. Smiley and V. Vogel. Near UV optical second harmonic generation studies of surface-adsorbed tryptophan residues. *J. Chem Phys.* **103**, 3140 (1995).

21. M. J. Crawford, S. Haslam, J. M. Probert, Y. A. Gruzdkov, and J. G. Frey. Second harmonic generation from the air/water interface of an aqueous solution of the dipeptide Trp-Trp. *Chem. Phys. Lett.* **230**, 260 (1994).

22. Z. Chen, M. Sheves, A. Lewis, and O. Bouevitch. A comparison of the second harmonic generation from light adapted, blue, and acid purple membrane. *Biophys. J.* **67**, 1155 (1994).

23. G. J. Vroege and H. N. W. Lekkerkerker. Phase transitions in lyotropic colloidal and polymer liquid crystals. *Rep. Prog. Phys.* **55**, 1241 (1992).

24. V. G. Taratuta, G. M. Srajer, and R. B. Meyer. Parallel alignment of poly-γ-benzyl-glutamate nematic liquid crystal at a solid surface. *Mol. Cryst. Liq. Cryst.* **116**, 245 (1985).

25. J. A. Mueller, R. S. Stein, and H. H. Winter. Rotation of liquid crystalline macromolecules in shear flow and shear-induced periodic orientation patterns. *Rheologica Acta* **35**, 160 (1996).

26. K. R. Makinson and D. Tabor. The friction and transfer of polytetrafluoroethylene. *Proc. R. Soc. London, Ser. A* **281**, 49 (1964).

27. C. M. Pooley and D. Tabor. Friction and molecular structure: the behaviour of some thermoplastics. *Proc. R. Soc. London, Ser. A* **329**, 251 (1972).

28. C. Fischer, J. K. Kruger, and W. Heitz. Surface-induced organization of N-alkanes on nanostructured PTFE. 2. Brillouin spectroscopic investigations on N-tritriacontane. *J. Phys.: Condens. Matter* **9**, 8407 (1997).

29. P. Damman, M. Dosiere, M. Brunel, and J. C. Wittmann. Nucleation and oriented growth of aromatic crystals on friction-transferred poly(tetrafluoroethylene) layers. *J. Am. Chem. Soc.* **119**, 4633 (1997).

30. D. Fenwick, K. Pakbaz, and P. Smith. Alignment of fluorescent molecules vapour-deposited on to highly oriented PTFE substrates. *J. Mater. Sci.* **31**, 915 (1996).

31. C. Y. Yang, Y. Yang, and S. Hotta. Crystal-structure and polymorphism of dimethyl-oligothiophenes crystallized epitaxially on highly oriented PTFE thin-films. *Synth. Met.* **69**, 303 (1995).

32. S. Sheiko, B. Blommers, H. Frey, and M. Moller. Substrate-induced orientation of poly(di-n-alkylsilylenes). *Langmuir* **12**, 584 (1996).

33. G. Lester, J. Hanmer, and H. Coles. PTFE drawn films as alignment agents for liquid crystals. *Mol. Cryst. Liq. Cryst.* **262**, 149 (1995).

34. P. Hubert, H. Dreyfus, D. Guillon, and Y. Galerne. Anchoring orientation of nematic and smectic A liquid crystals on PTFE treated plates. *J. Phys. II (France)* **5**, 1371 (1995).

35. J. R. Rasmusson, R. Erlandsson, W. R. Salaneck, M. Schott, D. T. Clark, and I. Lundstrom. Adsorption of fibrinogen on thin oriented poly(tetrafluoroethylene) (PTFE) fibres studied by scanning force microscopy. *Scanning Microscopy* **8**, 481 (1994).

36. H. Suzuki, K. Oiwa, A. Yamada, H. Sakakibara, H. Nakayama, and S. Mashiko. Linear Arrangement of Motor Protein on a Mechanically Deposited Fluoropolymer Thin Film. *Jpn. J. Appl. Phys., Part 1* **34**, 3937 (1995).

37. P. Dietz, P. K. Hansma, K. J. Ihn, F. Motamedi, and P. Smith. Molecular structure and thickness of highly oriented poly(tetrafluoroethylene) films measured by atomic force microscopy. *J. Mater. Sci.* **28**, 1372 (1993).

38. P. Bodo and M. Schott. Highly oriented polytetrafluoroethylene films: a force microscopy study. *Thin Solid Films* **286**, 98 (1996).

39. H. Hansma, F. Motamedi, P. Smith, P. Hansma, and J. C. Wittman. Molecular resolution of thin, highly oriented poly(tetrafluoroethylene) films with an atomic force microscope. *Polymer* **33**, 647 (1992).

40. G. Beamson, D. T. Clark, D. E. Deegan, N. W. Hayes, D. S.-L. Law, J. R. Rasmusson, and W. R. Salaneck. Characterization of PTFE on silicon wafer tribological transfer films by XPS, imaging XPS and AFM. *Surf. Interface Anal.* **24**, 204 (1996).

41. M. Schott. Preparation and properties of highly oriented polytetrafluoroethylene films. *Synth. Met.* **67**, 55 (1994).

42. M. Kobayashi, M. Sakashita, T. Adachi, and M. Kobayashi. Morphology-dependent anomalous frequency-shifts of infrared-absorption bands - poly(tetrafluoroethylene) and its linear oligomers perfluoroeicosane and perfluorotetracosane. *Macromol.* **28**, 316 (1995).

43. P. Dannetun, M. Schott, and M. R. Vilar. High-resolution electron-energy-loss spectroscopy of thin crystalline highly oriented films of poly(tetrafluoroethylene). *Thin Solid Films* **286**, 321 (1996).

44. M. K. Kar and S. Bahadur. Micromechanism of wear at polymer-metal sliding interface, in *Wear of Materials 1977,* eds. W. A. Glaeser, K. C. Ludema, and S. K. Rhee (American Society of Mechanical Engineers, New York, 1977) p. 501.

45. T. Boland and J. Dennis, unpublished results (1993).

46. B. J. Briscoe, A. K. Pogosian, and D. Tabor. The friction and wear of high-density polyethylene: the action of lead oxide and copper oxide fillers. *Wear* **27**, 19 (1974).

47. J. Cognard. Alignment of nematic liquid crystals and their mixtures. *Mol. Cryst. Liq. Cryst.* **51**, 1 (1982).

48. D. W. Berreman. Solid Surface Shape and the Alignment of an Adjacent Nematic Liquid Crystal. *Phys. Rev. Lett.* **28**, 1683 (1972).

49. J. M. Geary, J. W. Goodby, A. R. Kmetz, and J. S. Patel. The mechanism of polymer alignment of liquid-crystal materials. *J. Appl. Phys.* **62**, 4100 (1987).

50. M. B. Feller, W. Chen, and Y. R. Shen. Investigation of surface-induced alignment of liquid-crystal molecules by optical second-harmonic generation. *Phys. Rev. A* **43**, 6778 (1991).

51. M. Barmentlo, N. A. J. M. van Aerle, R. W. J. Hollering, and J. P. M. Damen. Surface induced liquid-crystal alignment studied by optical second-harmonic generation. *J. Appl. Phys.* **71**, 4799 (1992).

52. G. Berkovic, T. Rasing, and Y. R. Shen. Second-order polarizability of various biphenyl derivatives. *J. Opt. Soc Am. B* **4**, 945 (1987).

53. Y. R. Shen. Studies of liquid crystal monolayers and films by optical second harmonic generation. *Liq. Cryst.* **5**, 635 (1989).

54. C. David and D. Baeyens-Volant. Absorption and fluorescence spectra of 4-cyanobiphenyl and 4'-alkyl- or 4'-alkoxy-substituted liquid crystalline derivatives. *Mol. Cryst. Liq. Cryst.* **59**, 181 (1980).

55. G. Berkovic, Y. R. Shen, G. Marowsky, and R. Steinhoff. Interference between second-harmonic generation from a substrate and from an adsorbate layer. *J. Opt. Soc Am. B* **6**, 205 (1989).

56. R. C. Weast. *CRC Handbook of Chemistry and Physics*, 66 ed. (CRC Press, Inc., Boca Raton, 1986).

57. J. Xue, C. S. Jung, and M. W. Kim. Phase Transitions of Liquid-Crystal Films on an Air-Water Interface. *Phys. Rev. Lett.* **69**, 474 (1992).

58. W. Chen, M. Feller, P. Guyot-Sionnest, C. S. Mullin, H. Hsiung, and Y. R. Shen. Second harmonic generation studies of liquid crystal monolayers and films. *Proc. SPIE* **1056**, 104 (1989).

59. P. Ye and Y. R. Shen. Local-field effect on linear and nonlinear optical properties of adsorbed monolayers. *Phys. Rev. B* **28**, 4288 (1983).

60. T. F. Heinz. Nonlinear optics of surfaces and adsorbates. Doctoral Thesis, University of California, Berkeley, 1982.

61. V. Mizrahi and J. E. Sipe. Phenomenological treatment of surface second-harmonic generation. *J. Opt. Soc Am. B* **5**, 660 (1988).

62. T. G. Zhang, C. H. Zhang, and G. K. Wong. Determination of molecular orientation in molecular monolayers by second-harmonic generation. *J. Opt. Soc Am. B* **7**, 902 (1990).

63. M. Kauranen, T. Verbiest, J. J. Maki, and A. Persoons. Second-harmonic generation from chiral surfaces. *J. Chem Phys.* **101**, 8193 (1994).

64. F. Geiger, R. Stolle, G. Marowsky, M. Palenberg, and B. U. Felderhof. Single-valued determination of second-order nonlinear susceptibilities by quarter-wave-plate rotation. *Appl. Phys. B* **61**, 135 (1995).

65. J. J. Maki, M. Kauranen, T. Verbiest, and A. Persoons. Uniqueness of wave-plate measurements in determining tensor components of second-order surface nonlinearities. *Phys. Rev. B* **55**, 5021 (1997).

66. M. Barmentlo and Q. H. F. Vrehen. Reorientation of liquid-crystal (LC) molecules in mixed surfactant/LC Langmuir films. *Chem. Phys. Lett.* **209**, 347 (1993).

67. B. L. Smiley. Application of Optical Second Harmonic Generation to Studies of Surface-Adsorbed Aromatic Amino Acids and Short Peptides. Doctoral Thesis, University of Washington, 1996.

68. J. Lekner. Optical properties of an isotropic layer on a uniaxial crystal substrate. *J. Phys.: Condens. Matter* **4**, 6569 (1992).

69. M. Buck, F. Eisert, M. Grunze, and F. Trager. Second-order nonlinear susceptibilities of surfaces. A systematic study of the wavelength dependence of thiol adsorption on polycrystalline gold. *Appl. Phys. A* **60**, 1 (1995).

70. M. Born and E. Wolf. *Principles of Optics,* 6th ed. (Pergamon Press, New York, 1980).

71. D. B. DuPre. Techniques for the evaluation of material constants in lyotropic systems and the study of pretransitional phenomena in polymeric liquid crystals, in *Polymer Liquid Crystals,* eds. A. Ciferri, W. R. Krigbaum, and R. B. Meyer (Academic Press, New York, 1982) p. 166.

72. A. J. Hurd, S. Fraden, F. Lonberg, and R. B. Meyer. Field-induced transient periodic structures in nematic liquid crystals: the splay Frederiks transition. *J. Phys. (France)* **46**, 905 (1985).

73. E. Iizuka. The liquid crystals of deoxygenated sickle-cell hemoglobin. *Mol. Cryst. Liq. Cryst.* **42**, 67 (1977).

74. C. Robinson. Liquid-crystalline structures in polypeptide solutions. *Tetrahedron* **13**, 219 (1961).

75. T. E. Strzelecka, M. W. Davidson, and R. L. Rill. Multiple liquid crystal phases of DNA at high concentrations. *Nature* **331**, 457 (1988).

76. T. Itou and A. Teramoto. Multi-phase equilibrium in aqueous solutions of the triple-helical polysaccharide, schizophyllan. *Polym. J.* **16**, 779 (1984).

77. M. M. Giraud-Guille. Liquid crystalline phases of sonicated type I collagen. *Biol. Cell* **67**, 97 (1989).

78. R. E. Buxbaum, T. Dennerll, S. Weiss, and S. R. Heidemann. F-actin and microtubule suspensions as indeterminate fluids. *Science* **235**, 1511 (1987).

79. A. Kerst, C. Chmielewski, C. Livesay, R. E. Buxbaum, and S. R. Heidemann. Liquid crystal domains and thixotropy of filamentous actin suspensions. *Proc. Natl. Acad. Sci. USA* **87**, 4241 (1990).

80. A. L. Hitt, A. R. Cross, and R. C. Williams. Microtubule solutions display nematic liquid crystalline structure. *J. Biol. Chem.* **265**, 1639 (1990).

81. R. J. Hawkins and E. W. April. Liquid crystals in living tissues. *Adv. Liq. Cryst.* **6**, 243 (1983).

82. S. D. Lee and R. B. Meyer. Elastic and viscous properties of lyotropic polymer nematics, in *Liquid Crystallinity in Polymers: Principles and Fundamental Properties*, ed. A. Ciferri (VCH Publishers, New York, 1991) p. 343.

83. E. Iizuka. Properties of the liquid crystals of some biopolymers. *Adv. Biophys.* **24**, 1 (1988).

84. S. Itou, K. Tozaki, and N. Komatsu. Lyotropic liquid crystalline structures of synthetic polypeptide 2. Measurements of elastic constants and coupling constants of poly(γ-benzyl L-glutamate) solutions by the Freedericksz transition. *Jpn. J. Appl. Phys., Part 1* **30**, 1230 (1991).

85. M. Somers and Y. Engelborghs. Kinetics of the spontaneous organization of microtubules in solution. *Eur. Biophys. J.* **18**, 239 (1990).

86. P. J. Flory. Phase equilibria in solutions of rod-like particles. *Proc. R. Soc. London, Ser. A* **234**, 73 (1956).

87. L. Onsager. The effects of shapes on the interaction of colloidal particles. *Ann. NY Acad. Sci.* **51**, 627 (1949).

88. A. R. Khokhlov. Theories based on the Onsager approach, in *Liquid Crystallinity in Polymers: Principles and Fundamental Properties*, ed. A. Ciferri (VCH Publishers, New York, 1991) p. 97.

89. A. R. Khokhlov and A. N. Semenov. Influence of external field on the liquid-crystalline ordering in solutions of stiff-chain macromolecules. *Macromol.* **15**, 1272 (1982).

90. F. C. Frank. On the theory of liquid crystals. *Discuss. Faraday Soc.* **25**, 19 (1958).

91. S. D. Lee. A numerical investigation of nematic ordering based on a simple hard-rod model. *J. Chem Phys.* **87**, 4972 (1987).

92. M. D. Weingarten, M. M. Suter, D. R. Littman, and M. W. Kirschner. Properties of the depolymerization products of microtubules from mammalian brain. *Biochemistry* **13**, 5529 (1974).

93. H. C. Berg and S. M. Block. A miniature flow cell designed for rapid exchange of media under high-power microscope objectives. *J. Gen. Microbiol.* **130**, 2915 (1984).

94. A. Ciferri. Phase Behavior of Rigid and Semirigid Mesogens, in *Liquid Crystallinity in Polymers: Principles and Fundamental Properties,* ed. A. Ciferri (VCH Publishers, New York, 1991) p. 209.

95. F. Gittes, B. Mickey, J. Nettleton, and J. Howard. Flexural rigidity of microtubules and actin filaments measured from thermal fluctuations in shape. *J. Cell Biol.* **120**, 923 (1993).

96. A net charge of -20 per tubulin monomer at pH 6.85 was calculated using the Wisconsin Package Version 9.1, Genetics Computer Group (GCG), Madison WI.

97. R. Hard and R. D. Allen. Flow birefringence of microtubules and its relation to birefringence measurements in cells. *Cell Motil.* **5**, 31 (1985).

98. R. B. Meyer. Macroscopic phenomena in nematic polymers, in *Polymer Liquid Crystals,* eds. A. Ciferri, W. R. Krigbaum, and R. B. Meyer (Academic Press, New York, 1982) p. 133.

99. G. Marrucci. Rheology of nematic polymers, in *Liquid Crystallinity in Polymers: Principles and Fundamental Properties,* ed. A. Ciferri (VCH Publishers, Inc., New York, 1991) p. 395.

100. J. Tabony and D. Job. Spatial structures in microtubular solutions requiring a sustained energy source. *Nature* **346**, 448 (1990).

101. J. Tabony and D. Job. Gravitational symmetry breaking in microtubular dissipative structures. *Proc. Natl. Acad. Sci. USA* **89**, 6948 (1992).

102. J. Tabony. Morphological bifurcations involving reaction-diffusion processes during microtubule formation. *Science* **264**, 245 (1994).

103. A. M. Turing. The chemical basis of morphogenesis. *Philos. Trans. R. Soc. London* **237**, 37 (1952).

104. A. Yamagishi, T. Takeushi, T. Higashi, and M. Date. Diamagnetic orientation of blood cells in high magnetic field. *Physica B* **177**, 523 (1992).

105. F. Diaz, W. Brass, G. Diakun, C. Dumortier, and H. Kramer. Alignment of microtubules in high magnetic fields, in *Biophysics of the Cytoskeleton*, San Felin de Guixols, Spain, October 3-8, 1995.

106. S. W. Morris, P. Palffy-Muhoray, and D. A. Balzarini. Measurements of the bend and splay elastic constants of octylcyanobiphenyl. *Mol. Cryst. Liq. Cryst.* **139**, 263 (1986).

107. H. J. Coles and M. S. Sefton. Pretransitional behaviour of the splay and twist elastic and viscotic constants for the nematic to smectic A phase transition in octyl cyanobiphenyl (8CB). *Mol. Cryst. Liq. Cryst. Lett.* **4**, 123 (1987).

108. G. S. Bloom and S. A. Endow. Motor proteins 1: kinesins. *Protein Profile* **2**, 1105 (1995).

109. J. R. Sellers and H. V. Goodson. Motor proteins 2: myosin. *Protein Profile* **2**, 1323 (1995).

110. S. M. Block. Fifty ways to love your lever: myosin motors. *Cell* **87**, 151 (1996).

111. J. Howard. The movement of kinesin along microtubules. *Annu. Rev. Physiol.* **58**, 703 (1996).

112. K. C. Holmes. The swinging lever-arm hypothesis of muscle contraction. *Curr. Biol.* **7**, R112 (1997).

113. S. T. Brady. A novel brain ATPase with properties expected for the fast axonal transport motor. *Nature* **317**, 73 (1985).

114. R. D. Vale, T. S. Reese, and M. P. Sheetz. Identification of a novel force-generating protein, kinesin, involved in microtubule-based motility. *Cell* **42**, 39 (1985).

115. J. T. Yang, W. M. Saxton, R. J. Stewart, E. C. Raff, and L. S. B. Goldstein. Evidence that the head of kinesin is sufficient for force generation and motility in vitro. *Science* **249**, 42 (1990).

116. R. J. Stewart, J. P. Thaler, and L. S. B. Goldstein. Direction of microtubule movement is an intrinsic property of the motor domains of kinesin heavy chain and *Drosophila* ncd protein. *Proc. Natl. Acad. Sci. USA* **90**, 5209 (1993).

117. D. L. Coy and J. Howard. Organelle transport and sorting in axons. *Curr. Opin. Neurobiol.* **4**, 662 (1994).

118. J. Howard, A. J. Hudspeth, and R. D. Vale. Movement of microtubules by single kinesin molecules. *Nature* **342**, 154 (1989).

119. J. M. Scholey. *Motility Assays for Motor Proteins* (Academic Press Inc., New York, 1993), pp 304.

120. H. Suzuki, A. Yamada, K. Oiwa, H. Nakayama, and S. Mashiko. Control of actin moving trajectory by patterned poly(methylmethacrylate) tracks. *Biophys. J.* **72**, 1997 (1997).

121. J. R. Dennis and V. Vogel. Liquid-crystal alignment on polytetrafluoroethylene and high-density polyethylene thin films studied by optical second-harmonic generation. *J. Appl. Phys.* **83**, 5195 (1998).

122. J. Howard, A. J. Hunt, and S. Baek. Assay of Microtubule Movement Driven by Single Kinesin Molecules. *Methods Cell Biol.* **39**, 137 (1993).

123. A. J. Hunt, F. Gittes, and J. Howard. The force exerted by a single kinesin molecule against a viscous load. *Biophys. J.* **67**, 766 (1994).

124. K. Svoboda and S. Block. Force and velocity measured for single kinesin molecules. *Cell* **77**, 773 (1994).

125. E. Meyhöfer and J. Howard. The force generated by a single molecule of kinesin against an elastic load. *Proc. Natl. Acad. Sci. USA* **92**, 574 (1995).

126. A. J. Hunt and J. Howard. Kinesin swivels to permit microtubule movement in any direction. *Proc. Natl. Acad. Sci. USA* **90**, 11653 (1993).

127. S. M. Block, L. S. B. Goldstein, and B. J. Schnapp. Bead movement by single kinesin molecules studied with optical tweezers. *Nature* **348**, 348 (1990).

128. Y. Y. Toyoshima, S. J. Kron, and J. A. Spudich. The myosin step size: measurement of the unit displacement per ATP hydrolyzed in an in vitro assay. *Proc. Natl. Acad. Sci. USA* **87**, 7130 (1990).

129. Y. Harada, K. Sakurada, T. Aoki, D. D. Thomas, and T. Yanagida. Mechanochemical coupling in actomyosin energy transduction studied by in vitro movement assay. *J. Mol. Biol.* **216**, 49 (1990).

130. G. Srajer, S. Fraden, and R. B. Meyer. Field-induced nonequilibrium periodic structures in nematic liquid crystals: nonlinear study of the twist Frederiks transition. *Phys. Rev. A* **39**, 4828 (1989).

131. F. Eisert, O. Dannenberger, and M. Buck. Molecular orientation determined by second harmonic generation (SHG): a study of self-assembled monolayers. (Manuscript in review)

APPENDIX A: COMPARISON OF FRESNEL FACTORS WITH THOSE PRESENTED BY MIZRAHI AND SIPE

A number of different methods of calculating the Fresnel factors used in SHG are given in the literature. The method used in this work was first presented by Heinz (60) for the case of a simple interface, and then extended by Feller et al. (50) to more complex layered structures, and modified further in this work. A somewhat different and commonly-used derivation is given by Mizrahi and Sipe (61); this is one of the few other systems which have been extended to treat layered systems more complicated than a simple interface. Here, their derivation will be related to the Heinz method. It will be shown that the two ultimately agree, but there are important differences between them which are not obvious and which must be taken into account in extending them to cover new systems. Mizrahi and Sipe's notation will be used here, to facilitate comparison with their paper; it is straightforward to relate this to the notation used elsewhere in this work.

Mizrahi and Sipe showed that for a simple interface, their Fresnel factors were equivalent to those of Heinz (see Eq. (3.2)), except for a difference in the treatment of the SH source layer. They did not assign this layer its own dielectric constants, but treated it as part of one of the media adjacent to the interface. When the monolayer dielectric constants of the Heinz results were replaced by those of the adjacent media, the two sets of results agreed. Mizrahi and Sipe also presented Fresnel factors for a SH signal emitted from the back surface of a thick slab, as shown in Figure A.2(a). The input factor derivations for this case are quite similar to those in Chapter 3, except that the fields which generate the SH signal are taken to be those just inside the slab, at $Z = 0^-$. The method of deriving the output factors is quite different than in Chapter 3: for an SH source at $Z = 0^+$, they first write the emitted SH field, and then add terms for the effects of crossing the boundary at $Z = 0$ into the slab and the boundary at $Z = -T$ exiting the slab.

The resulting SH signal from the back surface of the thick slab is presented as follows by Mizrahi and Sipe. The total power, similar to Eq. (2.1) for SH energy, is:

$$P(2\omega) = \frac{32\pi^3\omega^2}{Ac^3}\sec^2\theta_{\text{in}}\left|\mathbf{e}^{2\omega} \bullet \chi^s : \mathbf{e}^{\omega}\mathbf{e}^{\omega}\right|^2 P^2(\omega) \tag{A.1}$$

where $P(\omega)$ and $P(2\omega)$ are the power of the fundamental and SH, and θ_{in} and A are the beam's incident angle and cross-sectional area outside the slab. The Fresnel factors, $\mathbf{e}^{\omega}$ and $\mathbf{e}^{2\omega}$, are:

$$\mathbf{e}^{\omega} = \left[\hat{s}t^s_{0m}\left(1 + r^s_{m0}\right)\hat{s} + \left(\hat{p}_+ + r^p_{m0}\hat{p}_-\right)t^p_{0m}\hat{p}_{0+}\right] \bullet \hat{\mathbf{e}}^{\text{in}} \tag{A.2}$$

$$\mathbf{e}^{2\omega} = \hat{\mathbf{e}}^{\text{out}} \bullet \left(\hat{S}T^s_{0m}T^s_{m0}\hat{S} + \hat{P}_{0-}T^p_{0m}T^p_{m0}\hat{P}_{0-}\right) \tag{A.3}$$

Here, the polarization vectors are as shown in Figure A.2(a): lower-case letters denote the fundamental frequency and upper-case the SH; subscripts of 0 are used for outside the slab and omitted within it; subscripts of + denote waves propagating downward while - is for waves propagating upward. The Fresnel reflection and transmission coefficients from medium a to b with k polarization are $r_{ab}{}^k$ and $t_{ab}{}^k$ (lower case for fundamental frequency, capitalized for SH), and subscript m is used in this case for the slab. The input and output polarization vectors are $\hat{\mathbf{e}}^{\text{in}}$ and $\hat{\mathbf{e}}^{\text{out}}$.

In the above Eq. (A.1) for the second-harmonic power, it is assumed that the slab sits in a vacuum. If another medium with dispersion surrounds the slab, several factors need to be reintroduced (which were omitted in Mizrahi and Sipe's Eq. (3.12) to (3.14)). The SH power becomes:

$$P(2\omega) = \left[\frac{32\pi^3\omega^2\sec^2\theta_{\text{out}}}{c^3\varepsilon_0(2\omega)}\right]\left[\frac{\sqrt{\varepsilon_0(2\omega)}A(2\omega)}{\varepsilon_0(\omega)A^2(\omega)}\right]\left|\mathbf{e}^{2\omega} \bullet \chi^s : \mathbf{e}^{\omega}\mathbf{e}^{\omega}\right|^2 P^2(\omega) \tag{A.4}$$

where $\varepsilon_0(\omega)$ and $\varepsilon_0(2\omega)$ are the dielectric constants of the external medium, $A(\omega)$ and $A(2\omega)$ are the beam areas, and θ_{out} is the exit angle from the slab.

Consider now an extension of this treatment to the case where the slab sits between two different media, as shown in Figure A.2(b). There is in this case an ambiguity of the terms in square brackets in Eq. (A.4). These terms contain constants of the medium surrounding the slab, but should this now become the medium above the slab or the medium below? Tracing these constants to where they appear in the derivation suggests the following assignment: the terms in the first set of brackets should go with the medium of the SH source, below the slab (medium 1), while the second set should go with the detection medium, above the slab. (This is of course why the terms were grouped this way.)

This suggested assignment of terms may be verified as follows. Returning to the case of Figure A.2(a), one may calculate the SH power within the slab and compare it to the power which exits the slab. To find the power within the slab, Eq. (A.4) is used with the slab as the detection medium, so the second set of square brackets in this equation takes on the slab's values, while the first set is unchanged. Also, the T_{m0} terms are removed from the output Fresnel factor in Eq. (A.3). The power exiting the slab is still given by Eq. (A.4) unmodified. The ratio of power which exits the slab to power within then has the correct form for the interface's power transmission (see for example Born and Wolf (70), Section 1.5, Eq. (27)):

$$\frac{P(2\omega)}{P_m(2\omega)} = \frac{\sqrt{\varepsilon_0(2\omega)}\cos\theta_{out}}{\sqrt{\varepsilon(2\omega)}\cos\theta_m(2\omega)} T_{m0}^2 \tag{A 5}$$

Since any other assignment of terms would give a different result, this verifies that our proposal is the correct one.

This assignment of terms may be used to extend Mizrahi and Sipe's treatment to arbitrary multilayer systems. The SH power for the case of Figure A.2(b) becomes:

$$P(2\omega) = \left[\frac{32\pi^3\omega^2 \sec^2\theta_1(2\omega)}{c^3\varepsilon_1(2\omega)}\right]\left[\frac{\sqrt{\varepsilon_0(2\omega)}A(2\omega)}{\varepsilon_0(\omega)A^2(\omega)}\right]\left|\mathbf{e}^{2\omega}\bullet\chi^s:\mathbf{e}^{\omega}\mathbf{e}^{\omega}\right|^2 P^2(\omega) \tag{A.6}$$

$$\mathbf{e}^{\omega} = \left[\hat{s}t_{0m}^s\left(1+r_{m1}^s\right)\hat{s} + \left(\hat{p}_+ + r_{m1}^p\hat{p}_-\right)t_{0m}^p\hat{p}_{0+}\right]\bullet\hat{\mathbf{e}}^{\text{in}} \tag{A.7}$$

$$\mathbf{e}^{2\omega} = \hat{\mathbf{e}}^{\text{out}}\bullet\left(\hat{S}T_{1m}^sT_{m0}^s\hat{S} + \hat{P}_{0-}T_{1m}^pT_{m0}^p\hat{P}_{1-}\right) \tag{A.8}$$

where subscripts of 1 refer to the bottom layer.

The above equations may now be compared with the Heinz method used elsewhere in this work. Eq. (2.1) for SHG energy appears essentially identical to Eq. (A.4), when written in the same notation. However, there is a very important difference: in the Heinz method all of the prefactors go with the detection medium, instead of the split assignment of factors just discussed. Thus for the system of Figure A.2(b), the SH power is stil given by Eq. (A.4) in the Heinz model, not by the modified form of Eq. (A.6). This difference is compensated by the different methods of defining and calculating the output Fresnel factors, so that the overall results are equivalent. This will be shown below, again for the system of Figure A.2(b).

For comparison, the output Fresnel factors of Eqs. (A.8) will be rewritten in component form:

$$\begin{aligned} e_x^{2\omega} &= T_{1m}^p T_{m0}^p \frac{\left(\hat{P}_{1-}\right)_x}{\left(\hat{P}_{0-}\right)_x} = T_{1m}^p T_{m0}^p \frac{\cos\theta_1(2\omega)}{\cos\theta_{\text{out}}} \\ e_y^{2\omega} &= T_{1m}^s T_{m0}^s \\ e_z^{2\omega} &= T_{1m}^p T_{m0}^p \frac{\sin\theta_1(2\omega)}{\sin\theta_{\text{out}}} \end{aligned} \tag{A.9}$$

The corresponding factors for the Heinz method are found from Eq.(3.7) with h taken to zero, and are labeled $e_H{}^{2\omega}$:

$$\begin{aligned} e_{H,x}^{2\omega} &= T_{m1}^p T_{0m}^p \frac{\cos\theta_1(2\omega)}{\cos\theta_{\text{out}}} \\ e_{H,y}^{2\omega} &= T_{m1}^s T_{0m}^s \\ e_{H,z}^{2\omega} &= T_{m1}^p T_{0m}^p \frac{n_1^2(2\omega)}{n_{\text{SH}}^2(2\omega)} \frac{\sin\theta_1(2\omega)}{\sin\theta_{\text{out}}} \end{aligned} \tag{A.10}$$

where n_{SH} is used for the refractive index of the SH source layer. This index is set equal to n_1 for comparison with the Mizrahi and Sipe method, as done previously. Then, using the definition of the reflection coefficients $T_{ab}{}^{k}$, it is easy to show component by component that:

$$\mathbf{e}_{H}^{2\omega} = \mathbf{e}^{2\omega} \frac{\sqrt{\varepsilon_0(2\omega)}\cos\theta_0(2\omega)}{\sqrt{\varepsilon_1(2\omega)}\cos\theta_1(2\omega)} \tag{A.11}$$

The input Fresnel factors for the Heinz method are equivalent to those of the Mizrahi and Sipe method, once n_{SH} is set equal to n_1. With the Heinz method, the SH power for any multilayer system is still given by Eq. (A.4). Plugging the Heinz input and output Fresnel factors into this equation, and substituting for the output factors using Eq. (A.11), then gives again Eq. (A.6), the SH power by the Mizrahi and Sipe method. This shows that the results of the two methods are equivalent.

The only remaining difference is in the model of the SH source layer: Heinz assigns it a separate dielectric constant while Mizrahi and Sipe do not. Either model has its difficulties. In Mizrahi and Sipe's model, the placement of the SH source at $Z = 0^+$ rather than at $Z = 0^-$ appears arbitrary, particularly since the fundamental field is evaluated at $Z < 0$. Also, the physical picture of a field emitted at one side of the interface and then transmitted or reflected by it seems not to fit situations where the monolayer lies precisely at the interface, such as a monolayer between two fluids. On the other hand, the dielectric constant of the monolayer in the Heinz model is difficult or perhaps impossible to measure, as Mizrahi and Sipe pointed out, and no justification in the literature for the convention of setting it to 1 has been found by this author. The values of dielectric constants and the differences between the two monolayer models may perhaps be resolved by comparison with data from other experimental techniques (131). Ultimately, any macroscopic model of the interface is only an approximation to the true microscopic behavior. The Heinz model intuitively appears to be a more natural approximation, since it does not take the fundamental and SH fields to be on opposite sides of the interface.

Here it has been shown how to generalize Mizrahi and Sipe's method of calculating Fresnel factors to more complex multilayer systems. The results of this method look very similar to those of the Heinz method, but it is essential to distinguish the differences in the output Fresnel factors and in the interpretation of terms in the SH power equations. When these differences are treated correctly, the results of the two methods are essentially equivalent, except for the different models of the SH source. The Heinz method has been used elsewhere in this work in order to make use of the Fresnel factors derived by Feller et al, and to compare our experimental results with similar published results which use this method. The Heinz model of the interface seems more reasonable physically, although decisive reasons for preferring it cannot be given.

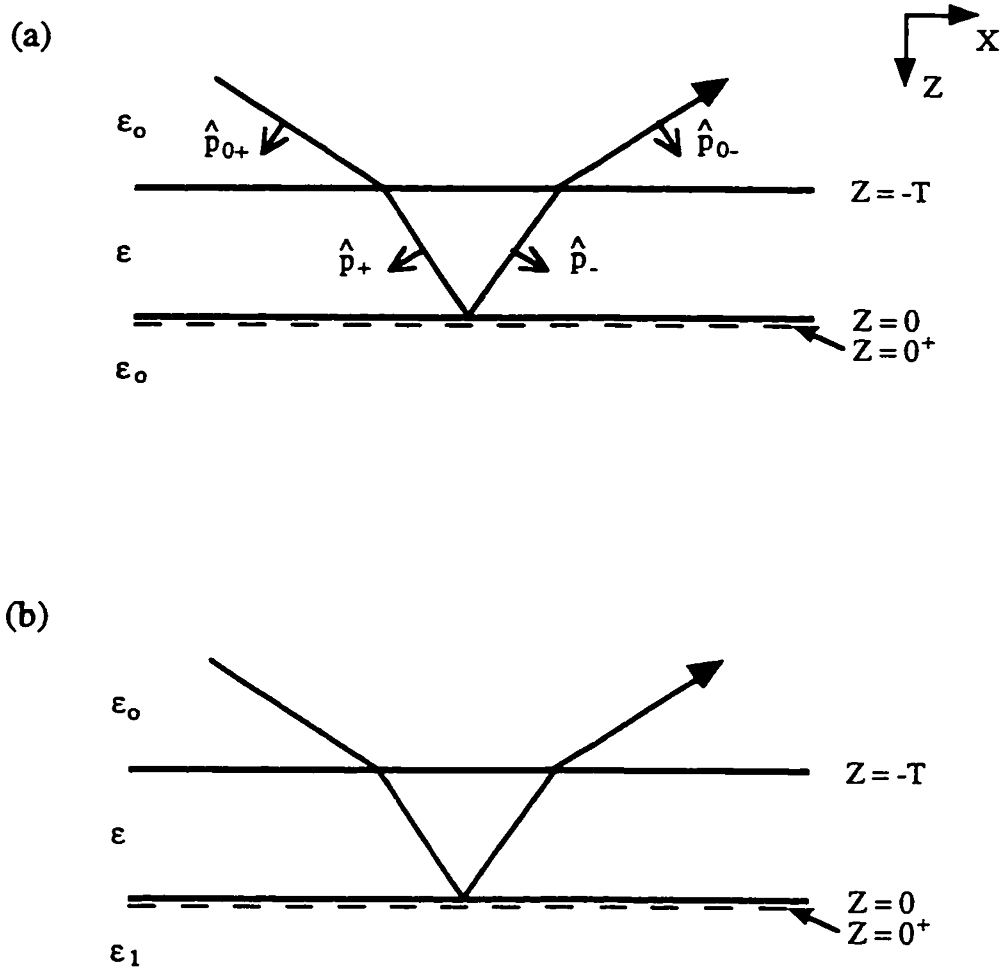

Figure A.2: Multilayer systems used for Fresnel factor comparisons.
The dashed lines at $Z = 0^+$ represent the SH sources, and dielectric constants of each layer are shown at left. The layer separation is taken to be large enough that multiple reflections need not be considered. (a) SHG from the back face of a thick slab surrounded by a single medium. The different polarization vectors for the p polarization are shown. (b) SHG from a slab with different media above and below the slab.

VITA

John R. Dennis

University of Washington

1998

EDUCATION

Ph.D., Physics, June 1998.
University of Washington, Seattle WA:
Dissertation: Mechanisms of liquid crystal and biopolymer alignment on highly-oriented polymer thin films

M. S., Physics, March 1992.
University of Washington, Seattle WA:

B.S., Physics, 1990.
Harvey Mudd College, Claremont CA
Coursework concentration: Computers in Physics.

PRESENTATIONS AND PUBLICATIONS

J. R. Dennis, J. Howard, and V. Vogel. Oriented transport of microtubules by kinesin adsorbed to patterned surfaces. Presented at *The Eighth International Conference on Organized Molecular Films*, Asilomar, California, USA, August 24-29, 1997.

J. R. Dennis and V. Vogel. Liquid-crystal alignment on polytetrafluoroethylene and high-density polyethylene thin films studied by optical second-harmonic generation. *J. Appl. Phys.* **83**, 5195 (1998).

AWARDS

NIH Molecular Biophysics Training Grant, 1992-1995
Graduation with High Distinction, Harvey Mudd College, 1990
ARCS Foundation Scholarship
National Merit Scholarship

IMAGE EVALUATION
TEST TARGET (QA-3)

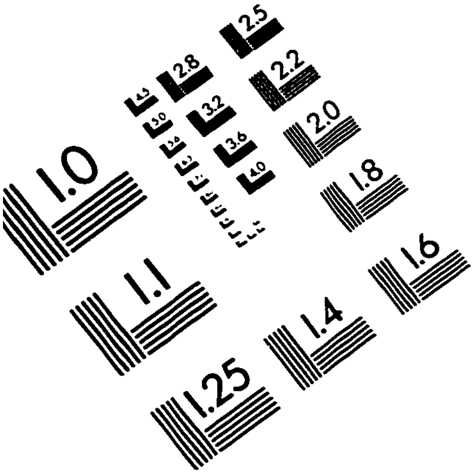

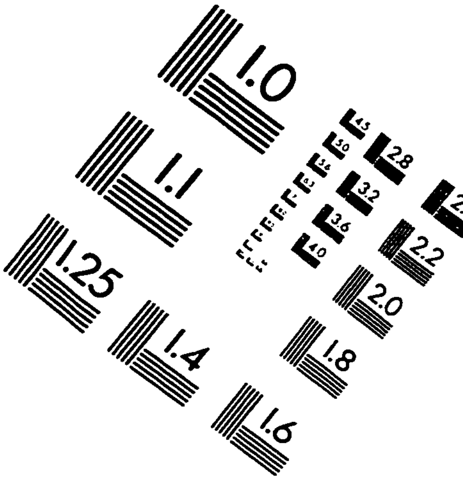

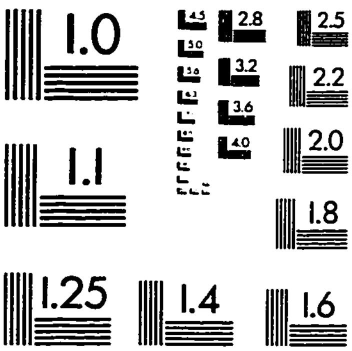

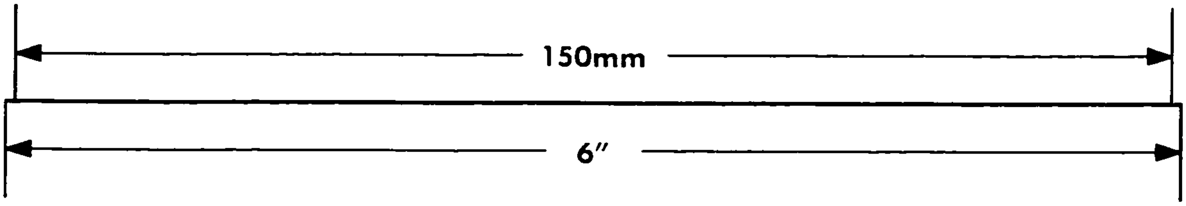

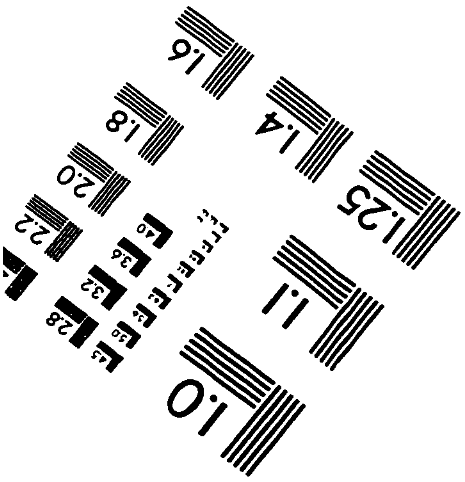

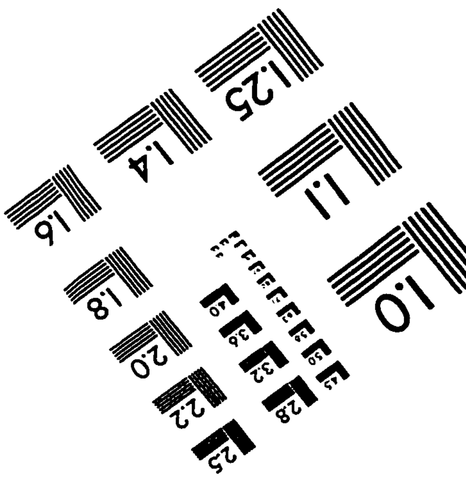

APPLIED IMAGE, Inc
1653 East Main Street
Rochester, NY 14609 USA
Phone: 716/482-0300
Fax: 716/288-5989